Properties of Terrestrial Gamma ray Flashes

Modelling and Analysis of BATSE and RHESSI data

Thomas Gjesteland

Dissertation for the degree of Philosophiae Doctor (PhD)

Department of Physics and Technology
University of Bergen

April 2012

Preface

This synthesis and collection of papers are submitted for the degree of philosophiae doctor (PhD) in physics at the Department of Physics and Technology, University of Bergen.

The thesis is divided into an introductory part and a part consisting of five papers published in international peer reviewed journals.

1. Østgaard, N., T. Gjesteland, J. Stadsnes, P. H. Connell, and B. Carlson, *Production altitude and time delays of the terrestrial gamma flashes: Revisiting the Burst and Transient Source Experiment spectra*, J. Geophys. Res., 113, A02307, doi:10.1029/2007JA012618, 2008

2. Gjesteland, T., N. Østgaard, P. H. Connell, J. Stadsnes, and G. J. Fishman, *Effects of dead time losses on terrestrial gamma ray flash measurements with the Burst and Transient Source Experiment*, J. Geophys. Res., 115, A00E21, doi:10.1029/2009JA014578, 2010

3. Gjesteland, T., N. Østgaard, A. B. Collier, B. E. Carlson, M. B. Cohen, N. G. Lehtinen *Confining the Angular Distribution of Terrestrial Gamma-ray Flash Emission.*, J. Geophys. Res., 116, A11313, doi:10.1029/2011JA016716, 2011

4. Gjesteland, T.,N. Østgaard, A. B. Collier, B. E. Carlson, C. Eyles, D. M. Smith *A new method reveals more TGFs in the RHESSI data* Geophys. Res. Lett., 39, L05102, doi:10.1029/2012GL050899, 2012

5. Østgaard, N., T. Gjesteland, B. E. Carlson, R. S. Hansen, and A. B. Collier, *The true fluence distribution of terrestrial gamma flashes at satellite altitude*, J. Geophys. Res., 117,A03327, doi:10.1029/2011JA017365,

Additional papers

I have, during my Ph.D. studies, also contributed to the following papers. They are not a part of the thesis.

- Cohen, M. B., U. S. Inan, R. K. Said, and T. Gjesteland, *Geolocation of terrestrial gamma ray flash source lightning*, Geophys. Res. Lett., 37, L02,801, doi:10.1029/2009GL041753, 2010.

- Collier A. B., T. Gjesteland, N. Østgaard. *Assessing the Power Law Distribution of TGFs.*, J. Geophys. Res,116 ,A10320, doi:10.1029/2011JA016612, 2011.

- Carlson B. E., T. Gjesteland, N. Østgaard. *Terrestrial gamma ray flash electron beam geometry, fluence, and detection frequency*,J. Geophys. Res, 116, A11217, doi:10.1029/2011JA016812,2011

- Carlson B. E., T. Gjesteland, N. Østgaard. *Connecting the terrestrial gamma-ray flash source strength and observed fluence distributions*,J. Geophys. Res, Res., 116, A11217, doi:10.1029/2011JA016812,2011

Contents

List of Figures

Acknowledgements

This PhD thesis is the result of four year work at the University of Bergen. All together I have now been at the University ten years and there are many people who have helped me and supported me during those years and I am very thankful.

First I will thank my advisor Nikolai Østgaard for all the help during my master and PhD Studies. He has been an excellent advisor. His enthusiasm has been a great source for inspiration and ideas. I will also thank Emeritus Johan Stadsnes who always has an open door and have given impressive answers to my questions. I am very grateful for the help and inspiring discussion with Brant Carlson whom I shared the office with the last two years in Bergen and at the time at Stanford. Thanks to Andrew Collier whom I had the pleasure to share office with the two months he visited our group.

I spent one semester at the VLF group at Stanford University which gave me a lot of experience. I will thank Umran Inan forn for inviting me to his group, and thanks to Brant Carlson, Nikolai Lehtinen and Morris Cohen for the collaboration at Stanford.

I would like to thank David Smith for the help and the use of the RHESSI data. Thanks to Jerry Fishman for the help and use of the BATSE data and Hugh Christian for the use of LIS/OTD data. Thanks to Paul Connell for the help in analysing the BATSE data and Chris Eyles for the help in developing the RHESSI search algorithm.

The years at the Department of physics and technology have been great. Thanks to the whole Space physics group and the associated for the social events, lavvo trips, cakes and other fun. It has been an inspiring, and fruitful environment. Many thanks to the TGFs people at UB, Brant, Ragnhild, Siri, Alexander and Øystein, for many good meetings and discussions. Thanks to Kåre Njøten and Arne Solberg for sharing old stories from the department and all the other advises. Thanks to Villy for the every day morning greetings.

I want to thank my parents and family for all help and support and also for taken care of my children whenever needed.

Finally, I am very grateful to my wife Marie for all she is and to my lovely children Mathilde and Johan.

Bergen, April 2012
Thomas Gjesteland

Chapter 1

Introduction

This thesis objective is to study Terrestrial Gamma ray Flashes (TGFs), which are short burst ($\sim$ 1 ms) of gamma-radiation from thunderstorms first discovered by *Fishman et al.* [1994]. The measured photons energies in TGFs are found to be up to several tens of MeV [*Smith et al.*, 2005; *Marisaldi et al.*, 2010a], which make them the most energetic natural photon phenomenon on Earth. The physics behind the production of TGFs are not well established. TGFs are assumed to be bremsstrahlung from relativistic electrons which are accelerated in strong electric fields related to thunderstorms. However, it is not known how frequent TGFs are, what are the altitude range in which they can be produced, the spatial extent of their source region, the angular distribution of the photons at the production altitude or to what kind of thunderstorms and lightning they are related to. There is a few suggested theories of how TGFs can be produced, but there are so far no consensus.

The aim of this thesis is to study TGFs in order to understand what this recently discovered natural phenomenon is. In the papers presented in this thesis several questions regarding the nature of TGFs are addressed. The main contributions can be summarized in three points.

1) Determine the production altitude of TGFs. The production altitude will give constraints on the electric fields that produces TGF and which type of lightning and/or thunderstorms that produces TGFs. The production altitude is investigated by comparing Monte Carlo simulations with measurements from the Burst And Transient Source Experiment (BATSE). The conclusions of Paper I [*Østgaard et al.*, 2008] and Paper II [*Gjesteland et al.*, 2010] of this thesis is that the TGFs measured by BATSE are produced in $\sim 10-20$ km altitude.

2) Determine the angular distribution of the photons produced in a TGF. The distribution of emitted photons will reflect the direction of the electric fields that produces the TGFs. Paper III [*Gjesteland et al.*, 2011] argue that TGFs are emitted within a cone of $30^\circ - 40^\circ$ indicating that TGFs are produced in nearly vertical electric fields.

3) Examine how common TGFs are. When TGFs were discovered they were thought to be a rare phenomenon since they were only observed $\sim$ once a month [*Fishman et al.*, 1994]. More recent results based on more sensitive instruments have observed $\sim$ 10 TGFs a month [*Grefenstette et al.*, 2009], which is more frequent but still rare. Paper IV [*Gjesteland et al.*, 2012] describes a method to lower the sensitivity threshold for the RHESSI satellite. Applying this method has more than double the number of identified TGFs. The increase of identified TGFs indicates that so far only

the top of an 'iceberg' of TGFs are observed. Paper V [*Østgaard et al.*, 2012] use an analytical approach, by comparing the relative TGF count rates of the RHESSI and Fermi satellites, to show that one cannot reject the hypothesis that all lightning produce TGFs. If this is the case, then TGFs are a very common phenomenon which may have important impacts of the coupling between the lower atmosphere and space.

This thesis starts with a historical walk trough the TGF research starting almost hundred years ago. Chapter 3 describes the two satellites instruments, BATSE and RHESSI, which are used in the studies of this thesis. Also, a brief overview of other experiments which have measured TGFs are presented. The same chapter also describes radio measurements of lightning which are found to be associated TGFs. Chapter 4 describes the basic theory behind TGFs. In chapter 5 present a brief summary of each of five papers, which is the scientific contribution in this thesis. The five papers are presented in chapter 6.

Chapter 2

History of terrestrial gamma ray flashes

2.1 Early years

Lightning have always fascinated mankind. In ancient times lightning and thunder were described by mythological creatures such as Thunderbirds or Thor and his hammer Mjølne. The modern understanding of lightning started with the famous kite experiment by Benjamin Franklin. Two hundred and fifty years ago he flew his kite into a thunderstorm and showed that lightning is electricity.

In the early 1920 C. T. R. Wilson, the Noble prize winner for the discovery of the cloud chamber, studied the electrical field of thunder clouds [*Wilson*, 1924]. He made a very simple model where he assumed that the thundercloud is an electric dipole. Above the thunderstorm the electric force on electrons, due to the electric moment of the dipole, decreases approximately with $1/z^3$ where z is the hight above the cloud. The threshold for dielectric breakdown in air scales approximately as the densities, which, in our atmosphere, decreases exponentially with a scale hight of ~ 7 km. Therefore there will be a point above the thundercloud, estimated by Wilson to be 60 km [*Wilson*, 1924], where breakdown occurs. This was a prediction for red sprites as they are known today [*Williams*, 2010]. Red sprites are transient luminous events (TLE), caused by electrical discharges that occur above thunderclouds.

In the cloud chamber Wilson found that the ionization tracks of electrons straightened with increasing energy [*Williams*, 2010]. In other words he found that the friction force on electrons decrease at increasing energies. With an applied electric field, such as those in thunderclouds, the electric acceleration force can exceed the friction force due to collision and the electron would run away and gain energy. Wilson stated:

Thus, β-particles which have traversed a few metres in the direction of the field have already acquired energies exceeding those of the fastest known β-particles from radioactive substances. [*Wilson*, 1924, p. 37D].

Such electrons, which experience a decreasing drag force at increasing energies, are now called runaway electrons. When high energy electrons, such as those Wilson discovered in the cloud chamber, collide with air molecules they will produce bremsstrahlung. Wilson predicted:

It would be of interest to test by direct experiment whether a thundercloud does emit any measurable amount of extremely penetrating radiation of X- or γ-ray type. [*Wilson*, 1925, p. 538].

2.2 Discovery of Terrestrial Gamma Ray Flashes

66 years after Wilson's prediction the Burst and Transient Source Experiment (BATSE) on board the Compton Gamma Ray Observatory (CGRO) observed the first TGF south of India April 22, 1991 [*Fishman et al.*, 1994]. CGRO was a big NASA observatory designed to study cosmic gamma ray burst (GRB). The BATSE instrument could estimate the direction from which the GRB comes. Since some of the bursts came from the Earth at times when the CGRO was close to thunderstorms, *Fishman et al.* [1994] concluded that this was the radiation from thunderclouds predicted by *Wilson* [1925].

Figure 2.1 shows the light curve of the first TGF. It is shorter than a typical GRB and contains a harder energy spectrum. The TGFs detected by BATSE have a duration of ~ 1 ms and energies above 1 MeV [*Fishman et al.*, 1994]. BATSE measured a total of 78 TGFs during its eight years mission.

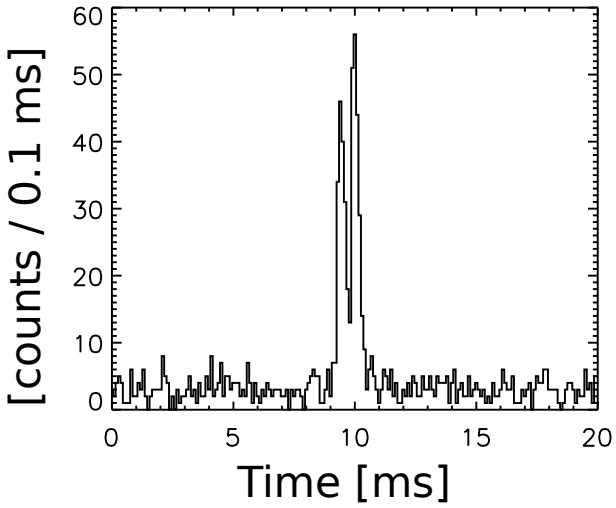

Figure 2.1: The light curve of BATSE trigger 106.

2.3 X and gamma-rays from thunderstorms

Fishman et al. [1994] was not the first to detect X-rays from thunderclouds. Wilson's ideas that thundercloud produce high energy radiation motivated several efforts to find such radiation and in the 1980-ties came the first evidence of X-rays from thunderclouds. *Parks et al.* [1981] and *Mccarthy and Parks* [1985] flew X-ray detectors in thunderclouds and found continuous X-rays with energy > 110 keV. The high X-ray fluxes lasted seconds prior to the observed lightning and returned to background within 0.1 second within the lightning discharge. They were surprised by the heigh photon fluxes and the high energies they measured. In the atmosphere there are naturally high energy particles and X-ray radiation caused by energetic cosmic rays and the extensive air showers of secondary particles they produce. E.g. [*Carlson et al.*, 2008] estimated that cosmic radiation produce $\sim 10^3 - 10^4$ energetic electrons per m^3 per second. However, *Mccarthy and Parks* [1985] concluded that their measurements of high energies and fluxes could not be described by cosmic rays alone: *An urgent problem is the iden-*

tification of the origin of the energetic electrons, whose presence is indicated by the observations presented here. Two processes meriting further study include the original Wilson mechanism and the production of energetic electrons near the concentrated field regions of leader tips. Any acceptable model must account for both the number flux and the high energies which are detected. [*Mccarthy and Parks*, 1985]

Continuous X-ray emission from thunder clouds have also been measured by *Eack et al.* [1996] who flew a balloon into a thundercloud. They measured minute long emission of X-rays which increased two orders of magnitude as the balloon passes through regions with enhanced electric field strength.

Even if the continues X-ray emissions from thunderstorms are different from TGFs in duration, fluxes and photon energies, both phenomena are assumed to origin from runaway processes.

Motivated by the observations of the high X-rays fluxes in thunderstorms *Gurevich et al.* [1992] picked up the idea of Wilson and further developed the theory of runaway electrons to runaway breakdown avalanches. The models were improved by *Roussel-Dupré et al.* [1994] with a kinetic treatment and the influence of magnetic field by *Gurevich et al.* [1996]. With the discovery of TGFs *Roussel-Dupré and Gurevich* [1996] argued that the TGF measurements by BATSE were a manifestation of relativistic runaway electron avalanches (RREA) in air. RREA is a theory that explains how discharges may occur in fields that are only one tenth of the conventional breakdown threshold. More detailed description of RREA and the production mechanisms of TGFs are presented in chapter 4.

Recent observations by satellite instruments such as Reuven Ramaty High Energy Solar Spectroscopic Imager (RHESSI) [*Grefenstette et al.*, 2009], Fermi Gamma ray Space Telescope [*Fishman et al.*, 2011] , and Astrorivelatore Gamma a Immagini Leggero (AGILE) [*Marisaldi et al.*, 2010a] have increased the knowledge about TGFs as this thesis has progressed. It is now widely accepted that TGFs occurs in RREA processes related to lightning activity. Most recent studies, included the results in this thesis, suggest that TGFs are produced below ~ 20 km, which indicates that it is electrical fields inside or right above thunderclouds that are the source of TGFs. But it is still not known how often TGFs occur and what is the driving electric field that produces them.

All instruments that have detected TGFs so far were designed for other purpose than TGFs. Therefore the measurements have certain problems. Especially deadtime losses in the measurements of the very high fluxes in TGFs have been a problem. Currently new mission, such as the Atmosphere-Space Interactions Monitor (ASIM) and Tool for the Analysis of Radiations from lightNIng and Sprites (TARANIS), are planned for space observation with electronic designed to handle the high fluxes in TGFs. These missions are needed to address the unknown questions about this very energetic natural photon phenomenon.

Chapter 3

TGF observations

This chapter will give an introduction to the measurements of TGF so far. This thesis have used data from the Burst and Transient Source experiment (BATSE) (paper I and II) and Reuven Ramaty High Energy Solar Spectroscopic Imager (RHESSI) (Paper III, IV and V). The TGF detection rate of Fermi Gamma Ray Space Telescope is used in paper V. Section 3.5 will discuss the detection of atmospherics (sferics) radio measurements which are related to TGFs. Such measurements are used in paper III and IV of this thesis.

3.1 Burst and Transient Source experiment (BATSE)

BATSE was one of four experiments on board the Compton Gamma Ray Observatory (CGRO). CGRO was a low Earth orbiting observatory ($\sim$ 450 km altitude) with inclination of 28.5°. It was launched April 5, 1991 and deliberately de-orbited on June 4, 2000. The primary objective was to study cosmic gamma ray burst (GRB), which due to the attenuation of gamma rays in the atmosphere, is not detectable on ground.

BATSE consisted of eight Sodium Iodide (NaI) Large Area Detector (LAD), each 2000 cm^2 [*Fishman et al.*, 1994] sensitive to photons with energies from 20 keV to 2 MeV [*Grefenstette et al.*, 2008]. The detectors were placed in each of the spacecraft's eight corners with the faces pointing in the same direction as in an octahedron. With this geometry one can use the ratio of counts in each detector to determine the location of the gamma source. Figure 3.1 shows the CGRO when it was launched from the Atlantis space shuttle. Four of the eight BATSE modules are marked with red circles.

To limit the amount of data BATSE used a trigger scheme to only collect the the most intense events. The search window were fixed to 64 ms, 256 ms and 1024 ms. The signal-to-noise threshold were changing during the mission but the typical trigger regime for TGFs was 5.5σ above background for a selection of the energy discriminators in the 64 ms window. 64 ms is long compared to the typical duration of TGFs ($\sim$ 1 ms). BATSE will therefore be biased to detected the longest and most intense TGFs. More description about the BATSE trigger criteria can be found at `http://gammaray.msfc.nasa.gov/batse/grb/catalog/current/trigger_criteria.html`.

The data was stored as time tagged events with time resolution of 2 μs and the energy in one of four fast discriminator channels covering the energy range $20-50$, $50-100$, $100-300$ and >300 keV [*Fishman et al.*, 1994]. The TGF energy spectra measured by BATSE were proportional to $\sim \varepsilon^{\lambda}$, where ε is the count energy and λ

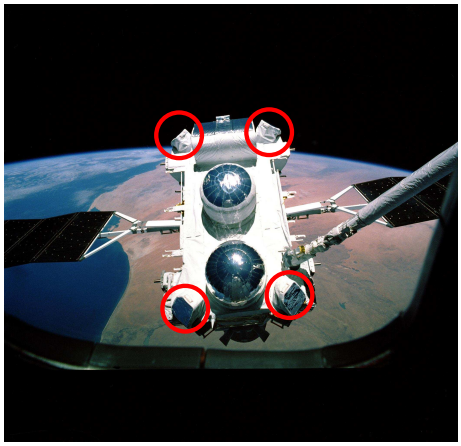

Figure 3.1: CGRO at launch from the space shuttle. Four of the BATSE LAD modules are marked with red circles. Image credit: NASA

varied from -0.6 to -1.5 [*Nemiroff et al.*, 1997]. Such energy spectra are harder than the energy spectra from GRB.

The TGFs measured by BATSE typically contain about 100 counts and have a duration $0.67 - 10.71$ ms [*Nemiroff et al.*, 1997]. The shortest TGFs consist of a single pulse, while the longer contain multiple pulses each lasting ~ 1 ms. The longest TGF, trigger 1457 (see figure 3.2), contain five pulses each separated about 2 ms [*Nemiroff et al.*, 1997]. Figure 3.2 show six examples of BATSE TGFs. Many of the TGFs measured by BATSE contains two or more pulses.

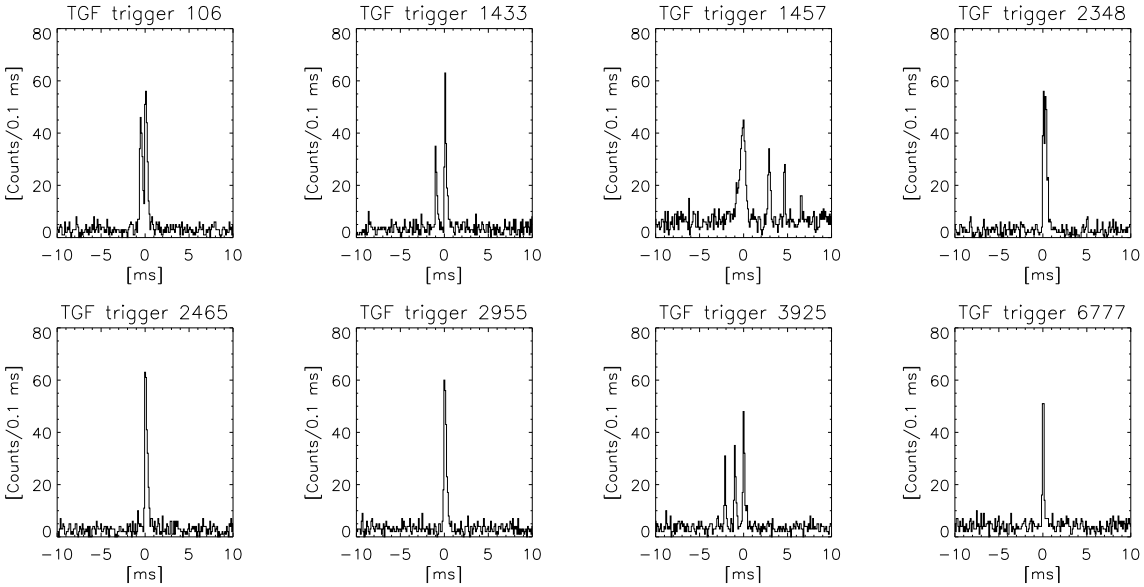

Figure 3.2: Lightcurve of BATSE TGFs. Many of the BATSE TGFs contained multiple pulses e.g. trigger 106, 1433, 1457 and 3925.

During its lifetime BATSE detected 78 TGFs [`http://gammaray.msfc.nasa.gov/batse/misc/triggers.html`]. Among the 78 TGFs from BATSE *Dwyer* [2008] suggested that many of them are in fact not burst of gamma, but bursts of electrons and

positrons. A further discussion on electrons beams produced by TGFs can be found in section 4.6.

The first analysis of the BATSE TGF data found a minimum variability time scale of typical 50 μs and interpreted this as TGFs were produced over a 15 km (50 μs $\times$ the speed of light) long region [*Nemiroff et al.*, 1997]. This finding together with the assumption that the atmosphere is only transparent for gamma-rays at altitudes above 40 km led to the conclusion that BATSE TGFs were related to red sprites.

Carlson et al. [2007] used a superposed spectrum from all the BATSE TGFs and compared it to simulated spectra. They found that a production altitude of 15-20 km could best represent the data. In paper I of this thesis [*Østgaard et al.*, 2008] a Monte Carlo code to simulate TGFs through the atmosphere is presented. The simulations is, for the first time, compared with individual TGF measurements from BATSE. *Østgaard et al.* [2008] determined that most TGFs are produced at low altitude (< 20 km), consistent with the earlier results [*Dwyer*, 2005; *Carlson et al.*, 2007], but they also found that a significant portion came from higher altitudes ($30 - 40$ km). However, it has been shown that the BATSE instrument suffered from a significant dead-time problem [*Grefenstette et al.*, 2008], i.e., that the read-out electronics of the BATSE instruments are not fast enough to count all the scintillation pulses from the detector material (See section 3.1.1 and paper II [*Gjesteland et al.*, 2010] for more information). When the effects of dead-time were treated properly *Gjesteland et al.* [2010] showed that the TGFs *Østgaard et al.* [2008] suggested were produced at 30-40 km in fact were produced at lower altitudes.

Another interesting finding in the BATSE data is the dispersion signature in the TGFs. *Feng et al.* [2002] found that the count profile for low energy photons (20-50 keV) where shifted with respect to the higher energy photons (>300 keV) with 240 μs on average. In the simulations by *Østgaard et al.* [2008] the dispersion signature was explained as a pure Compton effect. Photons that travel through the atmosphere are Compton scattered. Compton scattering changes the photons direction and reduces its energy. As a consequence the photons that escapes the atmosphere at low energy are more scattered and therefore have gone a longer path on their way through the atmosphere. Since all photons travel with the speed of light, low energy photons will arrive satellite altitudes later than high energy photons. The dispersion found in *Østgaard et al.* [2008] was ~ 100 μs which is shorter than found in *Feng et al.* [2002]. However, as shown in *Gjesteland et al.* [2010], this difference is explained by the losses due to dead-time in the BATSE instrument.

3.1.1 Losses due to dead-time

In an analysis of count rates in both RHESSI and BATSE *Grefenstette et al.* [2008] showed that BATSE TGFs had a lower peak count rate than RHESSI TGFs when the effective detection areas were accounted for. This suggest that BATSE suffered from losses due to dead-time in the read out electronics. By analysing the BATSE preflight data *Grefenstette et al.* [2008] found that the BATSE detectors worked as paralyzable detectors. A paralyzable detector with dead-time, τ, which do not vary on the photons energy, suffers from dead-time losses on the form

$$m = ne^{-n\tau} , \tag{3.1}$$

where m is the measured count rate, n is the incoming pulse rate and τ is the instrument dead-time [*Knoll*, 1989]. When $n \rightarrow \infty$ the measured count rate , $m \rightarrow 0$ and the detector is totally paralyzed.

The BATSE dead-time was dependent on photon energy. As found by *Grefenstette et al.* [2008], the dead-time in BATSE can be described by

$$\tau = \alpha \ln \frac{E_p}{E_0} , \tag{3.2}$$

where α is the signal decay time, E_p is the energy of the incoming photon and E_0 is the instrument reset level. Based on preflight data the estimated values are $\alpha = 0.75\mu$s and $E_0 = 5.5$ keV [*Grefenstette et al.*, 2008]. The result of equation 3.2 is that high energy photons results in longer dead-time than lower energy photons such that the dead-time losses are more significant for harder spectra.

With the claim that BATSE peak count rate is ~ 4 times larger than measured and that the energy spectrum were changed by the losses due to dead-time [*Grefenstette et al.*, 2008], all result based on BATSE spectra were questionable. *Østgaard et al.* [2008] did spectral analysis of individual BATSE TGFs and concluded that most of the TGFs were produced at altitudes below ~ 20 km. However, a significant portion were suggested to be produced at a higher altitude ($30-40$ km). All of these where single pulse TGFs with high count rates indicating that these TGFs suffered the most from losses due to dead-time. Therefore *Gjesteland et al.* [2010] implemented the dead-time effects on the BATSE instrument and applied them on the single pulse TGFs. The main effects of dead-time losses for BATSE are that the energy spectrum become significantly softer for increasing losses. Such softening influence the spectral analysis of the event and, as showed in *Gjesteland et al.* [2010], the production altitude becomes lower when dead-time are treated properly. *Gjesteland et al.* [2010] conclude that also the single pulse TGFs are consistent with a production altitude below ~ 20 km altitude.

Since BATSE was a paralyzable detector a single pulse TGF can be measured as a double pulse TGF. BATSE trigger 2348 is such example. *Gjesteland et al.* [2010] suggest that this TGF contains two pulses due to paralyzation of the read-out electronics. In that case the event is ~ 6 times brighter than measured [*Gjesteland et al.*, 2010]. A full description of the dead-time effects in BATSE can be found in paper II of this thesis.

3.2 Reuven Ramaty High Energy Solar Spectroscopic Imager (RHESSI)

RHESSI (figure 3.3) is a small observatory designed to study solar flares. It was launched on February 5, 2002 into a low orbit (~ 600 km altitude) with inclination 38° and is still operating. Its instrument consists of nine Germanium detectors inside an Aluminium cryostat. The Germanium detectors are divided into front and rear segments. The front segments are used to image solar flares from the sun with an energy range of 3 kev - 2.7 MeV and is not used in search for TGFs [*Grefenstette et al.*, 2009]. The rear detectors views the whole sky and are only shielded by the thin cryostat. The rear segments energy range is ~ 30 keV to 17 MeV. If a photon deposit more than 17 MeV in one detector the photon will be measured in an overflow channel. One photon can also deposit energy in more than one detector by Compton scattering. In that

case the two (or more) counts will have the same time tag. By combining coincident counts *Smith et al.* [2005] showed that RHESSI is measuring TGFs with energy up to 20 MeV. This is a very important results since the measurements from BATSE could only tell that TGFs contains photons with energy above > 1 MeV. RHESSI has also a much higher detection rate than BATSE. The first 183 days they measured 83 TGFs [*Smith et al.*, 2005], which lead to an estimate of ~ 50 TGF per day globally. These new measurements shows that TGFs are a much more common and powerful phenomenon than previously assumed.

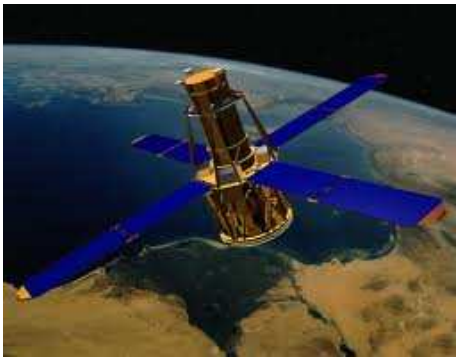

Figure 3.3: Illustration of RHESSI. Image credit: NASA.

The RHESSI relative time resolution is 1 binary micro second (2^{-20}s), but is not clear how well RHESSI are synchronised with Universal Time (UT). A giant flare from SGR 1806-20 on December 27 2004 which was measured by both the Swift and RHESSI satellites indicates that the RHESSI clock is 1.8 ms slower than UT [*Grefenstette et al.*, 2009]. It is not known if this offset is constant or varying during the mission.

Unlike BATSE RHESSI do not work in a trigger scheme but telemeters all data to ground. However, the data stream is decimated or switched off as RHESSI passes in regions with high fluxes of energetic particles such as the South Atlantic Magnetic Anomaly (SAMA), and at high latitudes where RHESSI passes close to the radiation belt.

The RHESSI catalog of TGFs is presented in *Grefenstette et al.* [2009]. It contains 820 TGFs from the period March of 2002 through February of 2008 and is the largest database of TGF events so far. The search algorithm applied on the raw data require at least 12σ above background in a 1 ms window, where the average background rate, N, is 2 counts per ms and $\sigma = \sqrt{N+1}$. This criteria is chosen such that the catalog is as clean as possible rather than complete. A typical RHESSI TGFs contains ~ 25 counts per TGF, which is significantly fewer than a typical BATSE TGF. This is due to a smaller effective detection area in RHESSI, but also due to the trigger algorithm on BATSE, which were biased to more intense events.

Grefenstette et al. [2009] also presented the results from an alternative TGF search algorithm. The number of events and quality of this search were not discussed, but it clearly showed that there are more TGFs than presented in the catalog. Motivated by these findings *Gjesteland et al.* [2012] developed a new search algorithm which was applied to the raw RHESSI data for 2004-2006. This algorithm more than doubled

the number of identified TGFs for this period. A full description and the result of this search algorithm can be found in paper IV of this thesis.

Figure 3.4 shows examples of RHESSI TGF lightcurves. Figure 3.4 a) and d) are RHESSI TGFs presented in the RHESSI catalog [*Grefenstette et al.*, 2009] and figure 3.4 b), c) ,e) and f) are new TGFs identified by the new search algorithm [*Gjesteland et al.*, 2012]. Multiple pulse TGFs such as shown in figure 3.4 d) and e) are rare in the RHESSI catalog compared to BATSE. This is most likely the result of BATSE trigger algorithms which were biased to detecting longer long events.

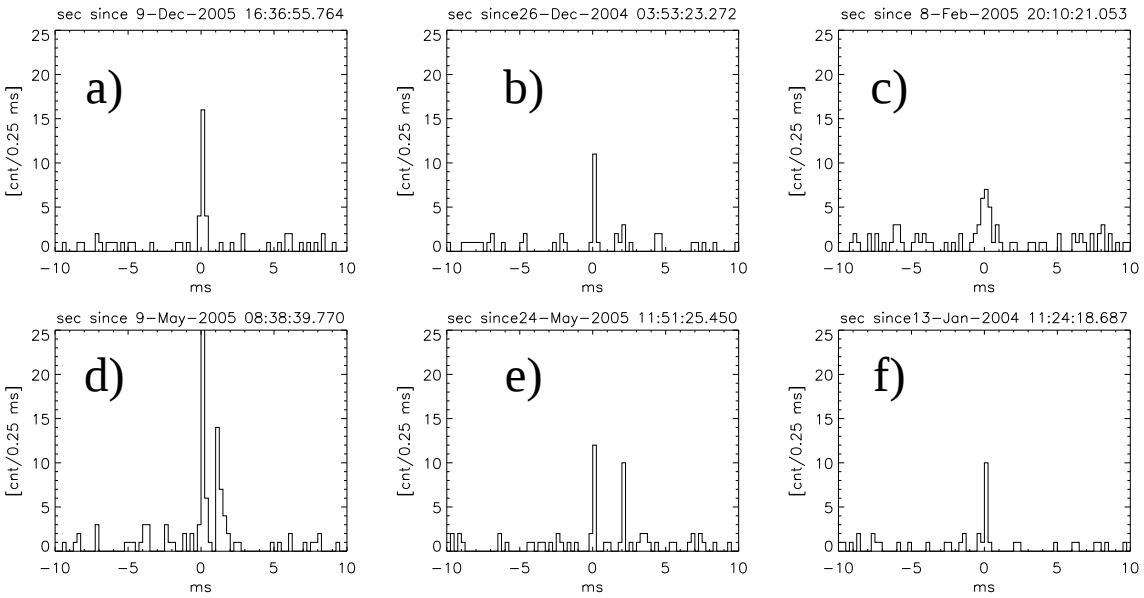

Figure 3.4: Lightcurve of RHESSI TGFs. a) and d) are RHESSI TGFs presented in the RHESSI catalog [*Grefenstette et al.*, 2009]. b), c) ,e) and f) are new TGFs identified by a new search algorithm presented by *Gjesteland et al.* [2012]

The first spectral analysis of RHESSI TGFs was done by *Dwyer and Smith* [2005]. They used a superposed spectrum of RHESSI TGF which were compared to Monte Carlo simulations. Their conclusion is that the superposed RHESSI spectrum is consistent with a source range of $15 - 21$ km, which is lower than previously assumed. These results were later confirmed by *Carlson et al.* [2007]. These new results with a production altitude below ~ 20 km points towards the cloud tops and not red sprites as the source for TGFs. *Cummer et al.* [2005] linked the RHESSI measurements to intra cloud (IC) lightning (See section 3.5), and *Williams et al.* [2006] used the properties of gamma attenuation as well as the polarity properties of lightning to support this production altitude.

Hazelton et al. [2009] identified thunderstorms near the RHESSI sub-satellite point at the time TGFs were observed. By superposing the spectrum of TGFs which had a thunderstorm within 300 km of the sub-satellite point (close events) and compare it with the superposed spectrum of TGFs without thunderstorms within 300 km (distant events), *Hazelton et al.* [2009] found that the spectrum of the distant events are softer. This is in agreement with the simulation results from *Østgaard et al.* [2008] as well as BATSE measurements which were softer at increasing observation angle [*Østgaard et al.*, 2008]. In order to determine the spatial distribution of TGF emission *Hazelton*

et al. [2009] compared the superposed spectra (close and distant) to Monte Carlo simulations. They concluded that either an emission within a narrow cone at 21 km altitude or an emission within a wide cone at 15 km altitude could best represent their measurements. Paper III *Gjesteland et al.* [2011] have addressed the same question by using RHESSI TGFs which are exactly geolocated. *Gjesteland et al.* [2011] found the same softening for distant TGFs and therefore conclude that the photons in a TGF are emitted within a cone with half angle of $\sim 30^\circ - 40^\circ$. This is in agreement with emission within the narrow cone as described by *Hazelton et al.* [2009].

Figure 3.5 shows the location of RHESSI TGFs from 2004-2006 divided into seasons. The red circles are from *Gjesteland et al.* [2012] and the green dots are TGF presented in the catalog TGFs. The grey scale is lightning activity measured by the Lightning Imaging Sensor (LIS) and Optical Transient Detector (OTD), which are optical instruments that measures lightning flashes from space [*Christian*, 2003]. The dashed lines are the limits of the RHESSI orbit. There are no TGFs in most of South America since RHESSI does not provide data for this region (SAMA). The distribution of TGFs follows the seasonal variation in lightning activity. For example during the northern hemisphere winter only one TGF occurs over the Caribbean while the vast majority of TGFs in the Caribbean occur during the northern hemisphere summer and fall.

The relation between RHESSI TGFs and lightning is also studied by *Splitt et al.* [2010]. They used data from WWLLN to identify storms related to RHESSI TGFs. The analysis shows that the TGFs are both spatially and temporally correlated with tropical thunderstorm systems. By comparing the RHESSI TGFs to the average tropopause pressure *Smith et al.* [2010] found that RHESSI TGFs tend to occur in times and places when the tropopause is high. Lightning have the same behaviour, but since the TGFs measured by RHESSI are shifted to even higher tropopause altitude it indicates that RHESSI is only detecting the TGFs that are produced at high altitude. There may be more events that are produced at lower altitude, but they are, due to atmospheric attenuation, too weak to be detected from space.

3.2.1 RHESSI dead-time

Grefenstette et al. [2008] found that both BATSE and RHESSI saturates from losses due to dead-time when they measure the high fluxes of photons in TGFs. RHESSI is a semi paralyzable detector and work as follows. If the time between two counts is less than 0.84 μs they are combined into one count (pile-up). If the time is greater than 0.84 μs and less than 5.6 μs both counts are removed by the veto system. If the time is between 5.6 μs and 9.6 μs the first count is recorded while the second is removed [*Grefenstette et al.*, 2009].

In order to determine the true TGF intensities distribution *Østgaard et al.* [2012] implemented the RHESSI dead-time effects in a Monte Carlo simulation. An example is shown in Figure 3.6. This is a TGF observed on November 26, 2004. The paralyzation curve is obtained by increasing the number of photons into a Monte Carlo simulation of the RHESSI response. The photons are distributed as a Gaussian within the estimated duration of the TGF, which for the TGF in figure 3.6 was 0.290 ms. As the number of incoming photons increase the measured count rate starts to deviate from the one-to-one relation. Simulation of a specific number of incoming photons was repeated 100

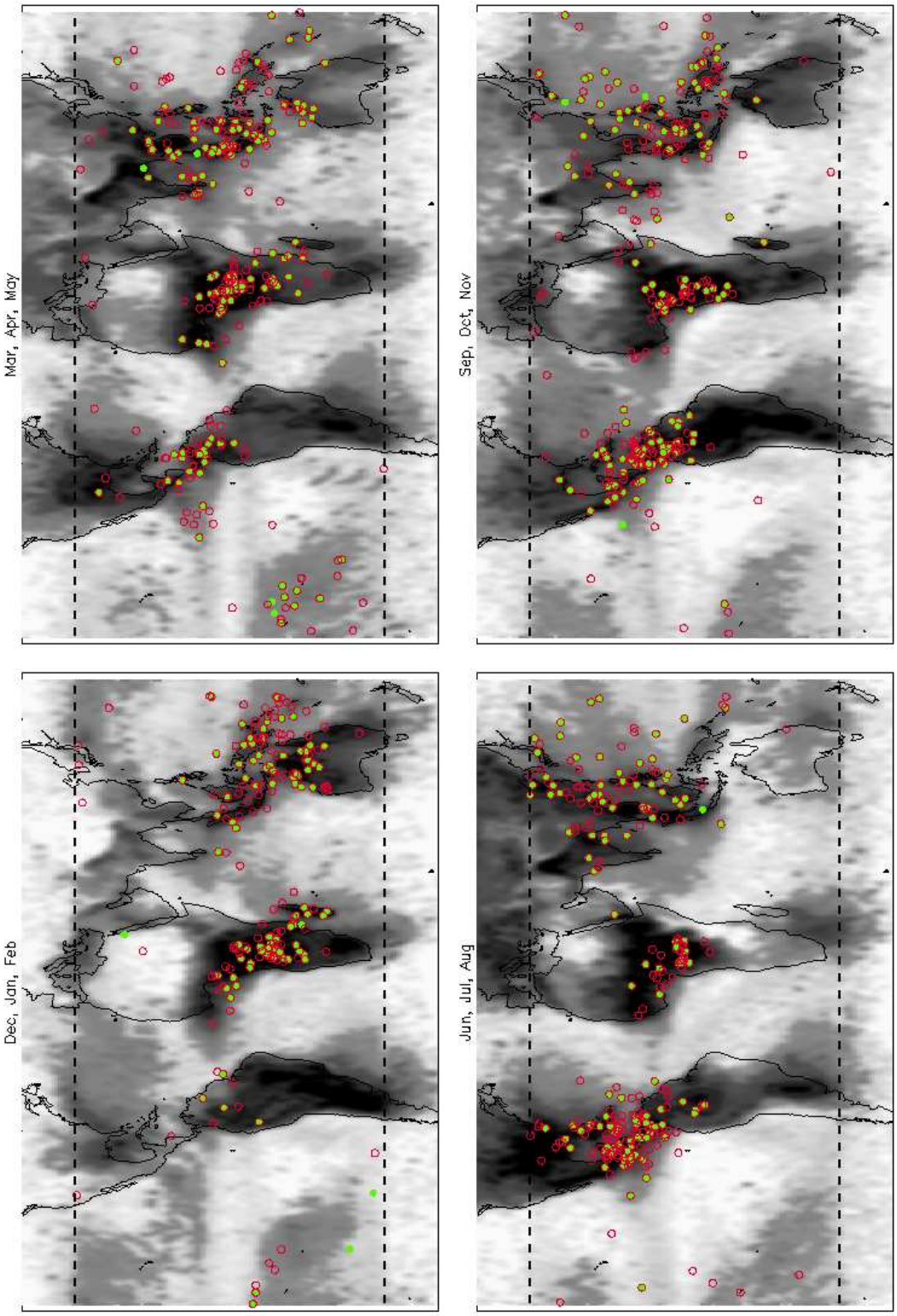

Figure 3.5: RHESSI TGFs for the years 2004, 2005 and 2006. The red circles are the TGFs found with the new search algorithm and green dots are the TGFs from the RHESSI TGF catalog. There are no TGFs in most of South America since RHESSI does not provide data for this region (SAMA). The grey scale indicates lightning activity measured by LIS/OTD. The dashed lines are the limits of the RHESSI 38° inclination orbit.

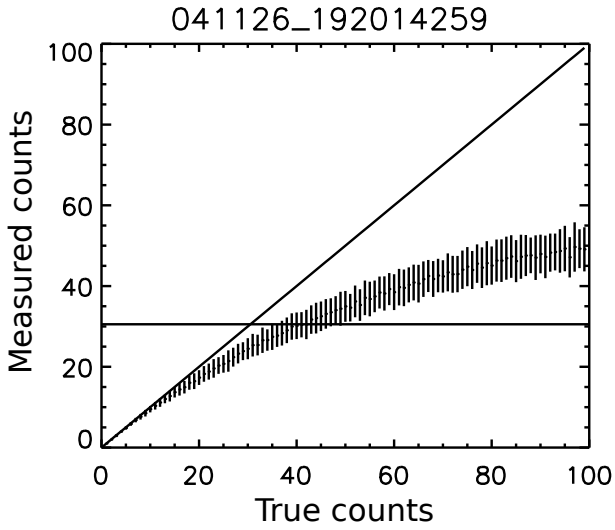

Figure 3.6: Monte Carlo simulation of the dead time losses of TGF November 26, 2004. The TGF duration is 0.290 ms. The vertical line is the number of measured counts by RHESSI. The tilted line shows the relation between measured and true counts without losses.

times to estimate the errors. The TGF in figure 3.6 contained 31 counts. By calculating where this line (31 counts) crosses the paralyzation curve this TGF is estimated to contain between 38 and 50 counts in the detectors, of which only 31 are recorded by the read-out electronics.

Østgaard et al. [2012] found that, due to the semi paralyzable behaviour, RHESSI is never totally paralyzed and it is very unlikely for RHESSI to measure a single pulse TGF as a double pulse TGF as *Gjesteland et al.* [2010] suggest BATSE did. Also, RHESSI does not have an energy dependency on the dead-time losses such as BATSE. It is therefore likely to assume that the dead-time losses in RHESSI do not influence the spectral analysis. This is also strengthened by the spectral analysis from BATSE and RHESSI that both suggest that TGFs are produced below $\sim$ 20 km altitude.

3.3 Fermi Gamma Ray Space Telescope

Fermi Gamma Ray Space Telescope (figure 3.7) was launched June 11, 2008 into a low earth orbit ($\sim$ 560 km altitude) with an inclination of 25.6° and it's primary objective is to study GRB [*Briggs et al.*, 2010]. It consists of two instruments; the Large Area Telescope (LAT) and the Gamma-ray Burst Monitor (GBM). So far only GBM have been used to identify TGFs. GBM has 12 NaI scintillator detectors with energy range $\sim$ 8 keV to 1 MeV and two Bismuth Germanate (BGO) scientillator with energy range $\sim$ 200 keV to $\sim$ 40 MeV [*Briggs et al.*, 2010]. Like BATSE, Fermi GBM has an on-board trigger algorithm. It triggers when the count rate is significant above background. The time scale and energy range can be modified in the flight software.

Fermi has an on board link to GPS to achieve very precise timing [*Connaughton et al.*, 2010]. The relative data time resolution is 2 μs. By a temporal analysis of the Fermi TGFs *Fishman et al.* [2011] found that the durations of the TGFs could be as short as $\sim$ 0.05 ms with rise times down to $\sim$ 10 μs. If one assume the speed of light

Figure 3.7: Illustration of Fermi Gamma Ray Space Telescope . Image credit: NASA.

this constrains the source region to ~ 2 km [*Briggs et al.*, 2010].

Fermi is still operating and recently the Fermi team has started to download all data from the regions where most TGFs are produced. By doing a ground search 234 TGFs were identified in 591.8 houers of data [*Briggs*, 2011]. This is ten times more TGFs than found in the trigger mode. This TGF count rate are used in paper V to estimate the true TGF fluence distribution as seen from space.

3.4 Astrorivelatore Gamma a Immagini Leggero (AGILE)

AGILE was launched April 23, 2007 into a low Earth orbit ($\sim$ 550 km altitude) with an inclination of 2.5° *Marisaldi et al.* [2010a]. It is sensitive to photons in the range 0.35–100 MeV. The Mini-Calorimeter (MCAL) instrument has an average detection rate of 10 TGFs/month [*Fuschino et al.*, 2011]. The first results showed TGFs with energies up to 40 MeV [*Marisaldi et al.*, 2010a], and later results indicate that TGFs can have energies up to 100 MeV [*Tavani et al.*, 2011]. The spectrum from the events with very high photon counts do not have the exponential fall off at higher energies, which the modelling results from RREA predicts. Instead the spectrum seems to have a broken power law shape. with $dn/d\varepsilon \sim \varepsilon^{-0.5\pm0.1}$ for 1 MeV $< \varepsilon <$ 7.1 $\pm$ 0.5 MeV and $dn/d\varepsilon \sim \varepsilon^{-2.7\pm0.1}$ above [*Tavani et al.*, 2011].

The AGILE MCAL has located 8 TGFs with gamma-ray photons of energies above 20 MeV with an accuracy of $\sim 5° - 10°$. All these events occurred within 600 km of the AGILE sub-satellite point [*Marisaldi et al.*, 2010b].

The small inclination orbit of AGILE results in high exposure time in the tropical region where the lightning density is the highest. *Fuschino et al.* [2011] found geographical differences in the TGF to lightning correlation which suggests that there are geographical and climatological modulation in the processes of TGF production. If one assumes that the TGF/lightning flash ratio holds at all latitudes *Fuschino et al.* [2011] estimate a global rate of 220 - 570 TGFs per day.

3.5 Sferics measurements

When TGFs were discovered they were found to occur in association with thunderstorms [*Fishman et al.*, 1994]. Lightning produce strong radio atmospheric (sferics) in

the Extremely Low Frequency (ELF < 3 kHz) and Very low Frequency (VLF, $3 - 30$ kHz) frequency range [*Rakov and Uman*, 2003, p.443]. ELF and VLF radio waves propagates well in the Earth-ionosphere wave guide with only a few dB attenuation per Mm and can therefore be detected far away from the lightning [*Cohen et al.*, 2010b]. Triangulation of sferics from several stations can be used to estimate the lightning location. It is assumed that the TGFs originate at the same location as the sferics [*Cummer et al.*, 2005; *Cohen et al.*, 2010b; *Collier et al.*, 2011; *Gjesteland et al.*, 2011].

In paper II of this thesis data from the World Wide Lightning Location Network (WWLLN) and the Atmospheric Weather Electromagnetic System for Observation, Modelling, and Education (AWESOME) network are used to calculate the distance between RHESSI sub-satellite point and the location of the source lightning. This distribution was then compared to Monte Carlo simulation of TGFs to constrain the initial angular distribution of the TGF emission [*Gjesteland et al.*, 2011].

In paper IV of this thesis [*Gjesteland et al.*, 2012] the matches between WWLLN and TGFs is also used to verify the new search algorithm on the RHESSI data. WWLLN is an expanding network which consisted of 38 stations in 2009 [*Abarca et al.*, 2010] and currently of more than 50 broadband receivers all over the world [`http://www.wwlln.net`]. It uses Time of Group Arrival (TOGA) algorithm to triangulate the source position of the emitted sferic. The quality of the network is improving due to adding more stations and improving the algorithm. In 2008-2009 WWLLN detected $\sim 10\%$ of cloud to ground (CG) lightning with currents stronger than 35 kA [*Abarca et al.*, 2010]. WWLLN has temporal and spatial accuracies of ~ 30 μs and 10 km [*Rodger et al.*, 2005].

Connaughton et al. [2010] searched for correlation between TGFs detected by Fermi GBM and sferics measured by WWLLN and found 15 good matches of 50 available TGFs. In 13 of these TGFs the lightning were simultaneous to ~ 40 μs of the peak of the the TGF. *Collier et al.* [2011] search for correlation between RHESSI TGFs and WWLLN and found 93 matches of 972 available TGFs. In the 93 matches *Collier et al.* [2011] found that the TGFs were preceding the associated lightning events with a mean of 0.77 ms. This suggest that the TGFs are produced in the initial stage of the lightning discharge. However, one also needs to consider that the timing of the RHESSI clock, which may not be constant, and an uncertainty of 2 ms should be included [*Grefenstette et al.*, 2009]. However, the results from *Collier et al.* [2011] indicate a systematic, rather than a random timing uncertainty.

Figure 3.8 shows the distance between the source lightning and the RHESSI sub-satellite point for the 93 TGFs which were found by *Collier et al.* [2011]. Most of the TGFs were observed closer than 400 km from the sub-satellite point but there are some events located as far as ~ 800 km away.

An interesting result from *Collier et al.* [2011] is that the matched TGFs were from the weaker end of the TGF intensity distribution. This result were further strengthen by a comparable match percentage in the new RHESSI TGFs found by *Gjesteland et al.* [2012], which contains TGFs weaker than in the RHESSI TGF catalog.

AWESOME uses wire-loop antennas which are sensitive to the orthogonal magnetic field and it is operating in the VLF range [*Cohen et al.*, 2010a]. It uses a similar technique as WWLLN to determine the source of the spheric but it also include magnetic direction finding. AWESOME have nine sites [*Cohen et al.*, 2010b] and is only sensitive to lightning from the Americas and West Pacific. A full description of AWESOME

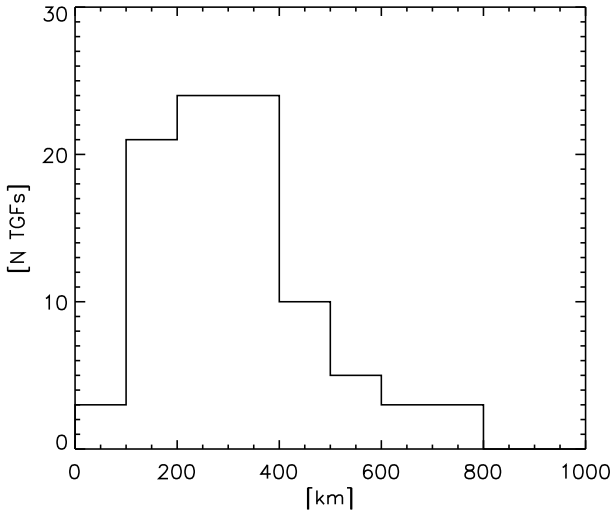

Figure 3.8: Distribution of distances between RHESSIsub-satellite point and the source lightning from WWLLN. The figure contains 93 TGFs presented in *Collier et al.* [2011].

can be found in *Cohen et al.* [2010a].

In the study by *Cohen et al.* [2010b] 36 RHESSI TGFs were geolocated, 16 of these were geolocated with measurements from 3 or more stations and they have and uncertanty in the geolocation of ~ 30 km [*Cohen et al.*, 2010b]. The two-stations cases have larger uncertainties and were not used in Paper III [*Gjesteland et al.*, 2011].

The first study indicating that there is a connection between sferics and TGFs was done by *Inan et al.* [1996] who found that two BATSE TGFs occurred in association with lightning activity. For one of the TGF their detector observed a sferic within ± 1.5 ms of the TGF. *Cohen et al.* [2006] found six additional BATSE TGFs showing a clear relation between sferics and TGFs. By studying 116 RHESSI TGFs *Inan et al.* [2006] found that 24% did not have associated sferics. However, several of these TGFs were later rejected as false events, and in a later study *Cohen et al.* [2010b] found that only 9 out of 158 TGFs are not associated with sferics. The remaining nine TGFs could be statistical anomalies or they could be associated with lightning which emits sferics below the detection threshold.

Meanwhile *Cummer et al.* [2005] compared RHESSI TGFs to sferics and found thirteen TGFs occurring within $-3/+1$ ms of a lighting discharge. All these lightning were of positive polarity. They calculated mean charge moment change to the lightning strokes associated with the TGFs to be 49 Ckm. Six of eight available RHESSI TGFs were linked to positive IC lightning by the Los Alamos Sferic Array (LASA) stations by *Stanley et al.* [2006] clearly showing that IC lighting is related to TGFs. A similar study of nine additional RHESSI events and LASA measurements also found that IC lightning and TGFs are closley related [*Shao et al.*, 2010].

In a study using the North Alabama Lightning Mapping Array (LMA) *Lu et al.* [2010] found a RHESSI TGF which were produced in association with an upward propagating leader. This TGF was followed by a slow pulse in the Ultra Low Frequency (ULF, $< 0.1 - 400$ Hz) range. The same slow pulse ($\sim 2 - 6$ ms) were found in 54 of 56 RHESSI TGFs for which the magnetic broad band data (< 0.1 Hz -30 kHz) were analysed [*Lu et al.*, 2011]. More recently *Cummer et al.* [2011] presented

two cases where a shorter, ($\sim$ 50 μs) but still slow, pulse in the broadband magnetic data that have a strong temporal connection with the gamma-ray count rate from Fermi GBM. Both the magnetic field data and the Fermi GBM data have very precise timing. It therefore indicates that the slow pulse and the TGF are simultaneously. However, *Cummer et al.* [2011] did not conclude whether or not the slow pulse is driven by lightning processes or by the RREA itself. However, *Dwyer* [2012] suggests that this slow pulse is emitted by the TGF producing electron avalanche as predicted by the relativistic feedback discharge (RFD) model of TGF. The RFD model is further discussed in section 4.4.3.

Chapter 4

Terrestrial gamma ray flashes

TGFs are a short flash of gamma radiation produced by thunderstorms. Based on average RHESSI TGF fluence the number of bremsstrahlung producing relativistic electrons at the production altitude must be on the order of $> 10^{16} - 10^{18}$ depending on the production altitude [*Dwyer and Smith*, 2005]. The energy of the electrons must be larger than the highest photon energy measured in TGFs, which is several tens of MeV [*Smith et al.*, 2005; *Marisaldi et al.*, 2010a]. This chapter will give a short introduction to how runaway electrons can be accelerated to relativistic energies and how a runaway avalanche can form. This chapter will also give an introduction to thunderstorms properties and discuss the theories that are suggested to explain TGF production. In section 4.5 a discussion of how these theories relates to the observations are presented, and section 4.6 gives a short introduction to electrons beams which are made by TGFs.

4.1 Runaway electrons

TGFs are assumed to be bremsstrahlung from relativistic electrons. To accelerate electrons to such high energies in the Earth atmosphere implies a runaway process. In a sufficiently large electric field energetic electrons will gain energy at a higher rate than they lose energy due to ionizing and radiation. As a results the energy of the electrons will increase and the electron becomes a runaway electron. As already known by the time C.T.R Wilson did his experiments, an electron with energy, ε, which collide with an electron or atom can be described as a Coulomb collision. The scattering from such collisions have a cross section, σ, given by $\sigma \propto 1/\varepsilon^2$. The friction force, F_D, on the electron is given by $F_D \propto \varepsilon\sigma\rho$, where ρ is the density. If one apply an electrical field, $E > F_D(\varepsilon)/q$, where q is the charge of the electron, the electrons will gain more energy than they loose due to collisions. This is the concept of runaway electrons which *Wilson* [1924] used to predict X and gamma radiation from thunder clouds.

Figure 4.1 shows the rate of energy loss of an energetic electron in a standard temperature and pressure (STP) atmosphere as a function of electron energy. This energy loss is the effective friction force, F_D on the electrons. The acceleration force on an electron due to an electric field is given by $F_a = qE$, where E is the electrical field strength and q is the electron charge. For electrons with energy ~ 1 MeV there is a minimum in the friction force and the break even electrical field $E_t \sim 2$ kV/cm, which is when $F_D = F_a$. As seen in figure 4.1 the break even field is far less than the conventional breakdown threshold in air ($E_k \sim 32$ kV/cm) and also lower than the threshold for

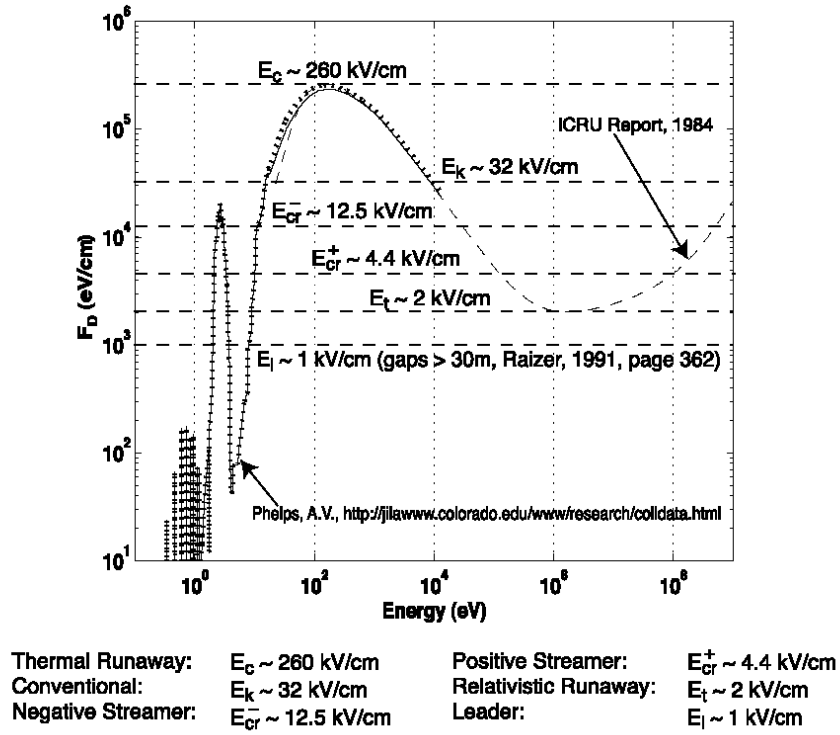

Figure 4.1: The friction force on electrons in air in a STP atmosphere. The figure is from *Moss et al.* [2006].

negative ($E_{cr}^- \sim 12.5$ kV/cm) and positive ($E_{cr}^+ \sim 4.4$ kV/cm) streamers to propagate. If the electric field is larger than $E_c \sim 260$ kV/cm thermal electrons will be accelerated over the peak in the friction force, which occur at electron energies ~ 200 eV, and into the runaway regime. This process is called cold runaway acceleration and is further discussed in section 4.4.4

It is worth to mention that runaway electrons have an upper energy limit. As the electrons energy increase the cross section for radiation increase and hence the friction fore increase. For example if the electrical field is 4.4 kV/cm the highest energy one can accelerate runaway electrons to is ~ 100 MeV (Se figure 4.1).

4.2 Relativistic runaway electron avalanche (RREA)

In strong electric fields an avalanche of runaway electrons can be formed. If the electric field accelerates an electron to such energies that it remains in the runaway regime after hard elastic scattering with atomic electrons, it is a runaway electron. If now the bounded electron gets knocked off and gain an energy such that both the runaway electron and the knock off electron are in the runaway regime after collision one gets avalanche formation. Motivated by the idea from *Wilson* [1924] and the measurements from *Mccarthy and Parks* [1985], *Gurevich et al.* [1992] studied these processes theoretical and found that relativistic runaway electron avalanche (RREA) can occur in thunderstorms. The threshold for a RREA to develop is $\sim$ 3kV/cm in STP air [*Dwyer*, 2012], which is appropriately ten times less field strength than needed for conventional

breakdown in air and 100 times less than cold runaway threshold. The RREA threshold scales with the densities which, in the atmosphere, decreases almost exponentially with an scale hight of ~ 7 km.

To initiate RREA one need seeds electrons which are in the runaway regime. In a thundercloud such electrons are constantly produced as secondary particles from cosmic rays [*Gurevich et al.*, 1992].

The avalanche growth factor, which is the number of particles one seed electron produce through the avalanche region, is highly dependent on the electrical field strength. According to [*Dwyer*, 2007, eq. 15] one can approximate the growth factor, N_{re}, by

$$N_{re} = \exp\left(\int_0^L \frac{dz}{\lambda}\right), \tag{4.1}$$

where λ is the avalanche length and L is the length of the avalanche region. For the Earth's atmosphere [*Coleman and Dwyer*, 2006, eq. 2] have estimated λ to

$$\lambda = \frac{7300 \pm 60\text{kV}}{E - 276 \pm 4\text{kV/m}} \tag{4.2}$$

solving 4.1 yields

$$N_{re} = \exp\left(\frac{E - 276\text{kV/m}}{7300\text{kV}} \times L\right). \tag{4.3}$$

In table 4.2 N_{RE} and L are calculated for various electric field strength, E and total available potential, $U = EL$. The numbers are presented are for STP air at sea level. At an altitude z the electric field scales with $n(z)/n_0$ and the length scales with $n_0/n(z)$, where n_0 is the density at sea level and $n(z)$ is the density at altitude z. The electrical fields in table 4.2 are chosen such that the electric field is larger than the RREA threshold, $E_t = 3 \times 10^5$ V/m for STP air, and lower than the conventional breakdown threshold, $E_K = 3.2 \times 10^6$ V/m for STP air. The numbers in table 4.2 shows that for total available potentials ≤ 100 MV the maximum growth factor $N_{RE} < 10^6$, while for electric fields close to the conventional breakdown threshold and total potential of 400 MV the growth factor can be $> 10^{21}$. However, there are no measurements that supports that one can have such large electric fields and potentials inside thunder clouds. Most measurements of the voltage in a thundercloud concludes that the maximum potential in a thunder cloud is in the order of ~ 100 MV [*Marshall and Stolzenburg*, 2001], however one can not exclude that higher potential exists. More discussion about thunder cloud electric fields and potential are presented in section 4.3.

If we assume that the maximum potential in a thundercloud is ~ 100 MV one sees that the maximum growth factor in RREA is $N_{RE} < 10^6$. This is far from the required $10^{16} - 10^{18}$ electrons which is needed to produce a TGF detectable in space. Therefore a model that explains TGFs must either relay on seed particles or an additional growth such as feedback first suggested by *Dwyer* [2003].

As discussed in the section above, to produce a TGF one either needs very strong electric field and high potential or additional seeding to gain the high fluence. Section 4.3 will present typical conditions in thunderstorms, and then section 4.4 will discuss the proposed theories for TGF production.

Table 4.1: The maximal growth rate, N_{RE}, and avalanches length, L, for STP air for various electric fields and total potentials. At an altitude z the E-field scales with $n(z)/n_0$ and the length scales with $n_0/n(z)$, where n_0 is the density at sea level and $n(z)$ is the density at altitude z.

	Total potential		
E-field (STP air)	100 MV	200 MV	400 MV
3.0×10^6V/m ($\sim 10\times E_t$)	$N_{RE}=2.5\times10^5$ $L=33$ m	$N_{RE}=6.0\times10^{10}$ $L=67$ m	4.0×10^{21} $L=133$ m
1.5×10^6V/m ($\sim 5\times E_t$)	$N_{RE}=7.1\times10^4$ $L=67$ m	5.0×10^9 $L=133$ m	$N_{RE}=2.6\times10^{19}$ $L=267$ m
0.7×10^6V/m ($\sim 2.5\times E_t$)	$N_{RE}=4.0\times10^3$ $L=143$m	$N_{RE}=1.6\times10^7$ $L=285$ m	$N_{RE}=2.6\times10^{14}$ $L=571$ m

4.3 Thunderstorms

Thunderstorms are complicated and the picture presented in this section is simplified to only include typically properties of thunderstorms. For more details I refer to the books by *Rakov and Uman* [2003] and *MacGorman and Rust* [1998].

Two hundred and fifty years ago Benjamin Franklin found that thunderclouds are electrically charged, and nearly 100 years ago C.T.R Wilson used ground based measurements to suggest that thunderclouds have a dipole structure with typically positive charge above the negative [*MacGorman and Rust*, 1998, p. 49]. This type of dipole is refereed to as a positive dipole. More recent in-situ measurements of thunderclouds shows that a simple description of a thundercloud can be a positive dipole with a small positive charge region below the main negative [*Rakov and Uman*, 2003, p. 68]. This structure is refereed to as the tripole structure as shown in figure 4.2. The altitudes and charge magnitudes are typically values and are adapted from [*Rakov and Uman*, 2003, p.69].

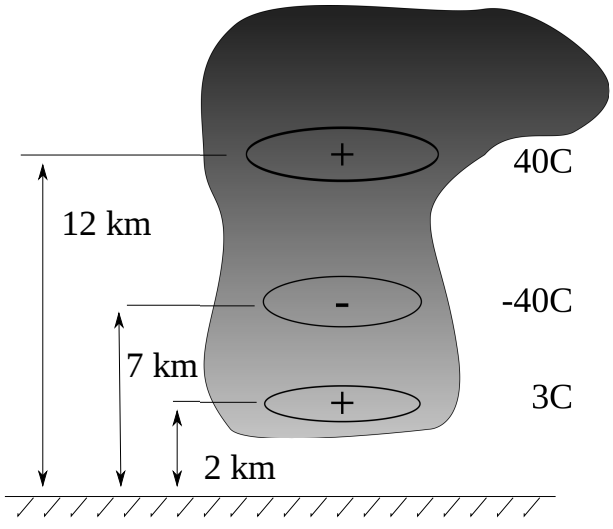

Figure 4.2: The tripole structure of a thundercloud. The altitudes and the magnitudes of the main charge regions are adapted from [*Rakov and Uman*, 2003, p.69]

As the thundercloud charges, via up-draft air, and form the tripole structure, an ambient electric field is build up between the charge regions. Several sounding balloon study have tried to measure the strength of the electrical fields inside thunderclouds. Typical values are higher than the RREA threshold but $\sim 2-3$ times lower than the threshold for conventional breakdown [*Williams*, 2006]. These observations have lead to the suggestion that RREA processes are involved in the initiation of lightning [*Gurevich and Zybin*, 2005; *Dwyer*, 2005], but one cannot reject the hypothesis that local electric field can be much higher and initiates the lightning. As soon as an leader is initiated, the electric field strength needed for leaders to propagate is lower than the conventional breakdown threshold as shown in figure 4.1.

The potential between the main positive and negative charge region is estimated to be $\sim 50-500$ MV [*Rakov and Uman*, 2003, p.111]. However, the highest in-situ measurement of the thundercloud potential is ~ 100 MV [*Marshall and Stolzenburg*, 2001]. Even if there is theoretical suggestion for higher potential in thunderclouds it is likely to assume that ~ 100 MV is a typically maximum potential. With potential above 50 MV the electric field can accelerate electrons up to 50 MeV, which is consistent with the highest photon energies measured in TGFs.

4.3.1 Lightning flash

The lightning flash is the entire process including leader formation, the stage where the leader connects two charge regions, either inside the clouds or from cloud to ground, and finally the discharge of the electrical fields via high currents flowing in the leader channels. A globally estimate of the lightning flashes are 44 ± 5 flashes per second [*Christian*, 2003]. They are most frequent in tropical regions over the continents. Figure 4.3 shows a map of the annual lightning flash rate from LIS/ODT. LIS and OTD are optical satellite born instruments which record the optical emissions from the lightning flashes. LIS/OTD cannot distinguish between IC or CG flashes. More information about LIS/OTD can be found in *Christian* [2003].

About 90% of the lightning flashes are intra cloud (IC) lightning between the main charge regions as seen in figure 4.2, and the remaining 10% are cloud to ground (CG) lightning [*Rakov and Uman*, 2003, p.108]. When CG lightning strikes the ground they produce a high current, called the return stroke. IC lightning do not strike any high conducting regions and therefore contain weaker current pulses [*Rakov and Uman*, 2003, p.341]. Due to the high current in the return stroke (high peak current) CG lighting emits more VLF radiation such that VLF networks are biased to locate CG lightning.

4.4 Production mechanisms for TGFs

As discussed above a thundercloud has the potential sufficient to produce photons with energies of several tens of MeV. In addition to the ambient field between the main charge regions, there are other electric fields which are candidates for TGF production. The following sections will discuss the production mechanisms of TGFs.

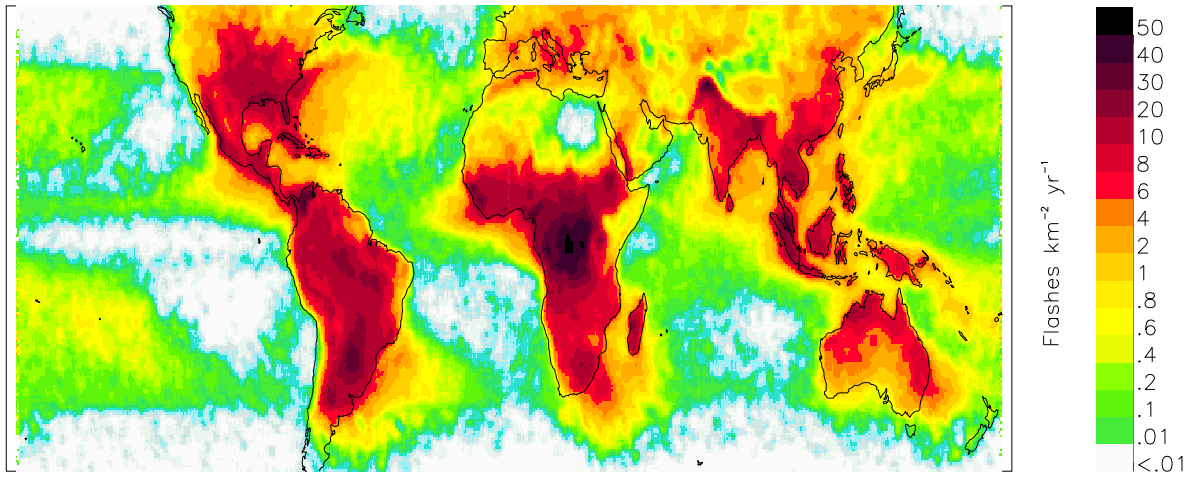

Figure 4.3: The annual lightning flash rate from LIS/ODT. The data are adapted from `http://thunder.nsstc.nasa.gov/data/`.

4.4.1 Quasi electro-static fields

A lightning discharge, either IC or CG, will discharge the electric field on a time scale much shorter than the relaxation time of the screening charges which surrounds the main charge regions. As a result a Quasi electro-static (QS) field will be present above the thunder cloud [*Pasko et al.*, 1995; *Lehtinen et al.*, 1996]. Figure 4.4 shows a simple model of the QS field after an IC lightning with the parameters in figure 4.2. The model assumes that the positive charges (40 C) is distributed uniformly inside a sphere with radius 1 km with located at 12 km altitude. The negative charge region (-40 C) is located at 7 km in a similar sphere. The lower positive region, as shown in figure 4.2, is ignored. An IC lightning stroke between the charge layers is modelled as a fast current which neutralize the charge regions. As a result the screening charges around the charge regions will make an quasi electro static field. The relaxation time for the screening charges are in order of seconds at 12 km altitude and longer at lower altitudes [*Rycroft*, 2000]. If we assume that the lightning discharge is much shorter than the relaxation time a quasi electrostatic field above the initial positive charge region is given by

$$E = \frac{Q}{4\pi\varepsilon_0}\left(\frac{1}{(z-h_t)^2} - \frac{1}{(z-h_m)^2}\right), \; z > h_t + R \tag{4.4}$$

where, Q is the charges of the main charge regions, $\varepsilon_0 = 8.85 \cdot 10^{-12}$ F/m (the electric constant), $h_t = 12$ km, $h_m = 7$ km and $R = 1$ km, which is the radius of the charge sphere. Inside the sphere, with radius R, of positive charge $(12-13$ km) the electric field is given by

$$E = \frac{Q}{4\pi\varepsilon_0}\left(\frac{z-h_t}{R^3} - \frac{1}{(z-h_m)^2}\right), \; z \in (h_t, h_t + R]. \tag{4.5}$$

The first terms in equation 4.4 and 4.5 are from the main positive charge region and the last terms are the contribution from the main negative charge region.

Equation 4.4 and 4.5 are plotted in figure 4.4. The dashed line in figure 4.4 is the

electric field threshold for RREA, E_t, and the dotted line is the threshold for conventional breakdown, E_k.

$$E_t = 3.0 \times 10^5 [V/m] \times \exp\{-z/H\} \tag{4.6}$$

$$E_k = 3.2 \times 10^6 [V/m] \times \exp\{-z/H\} \tag{4.7}$$

where H is the atmospheric scale hight of 7 km.

This simple model of an IC lightning shows that one may exceed the conventional threshold at ~ 90 km altitude and the RREA threshold at ~ 70 km. But it also shows that the RREA threshold is exceeded very close to or inside the thundercloud. For the case shown in figure 4.4 the total potential when $E > E_t$ in the region 12-15 km is ~ 118 MV.

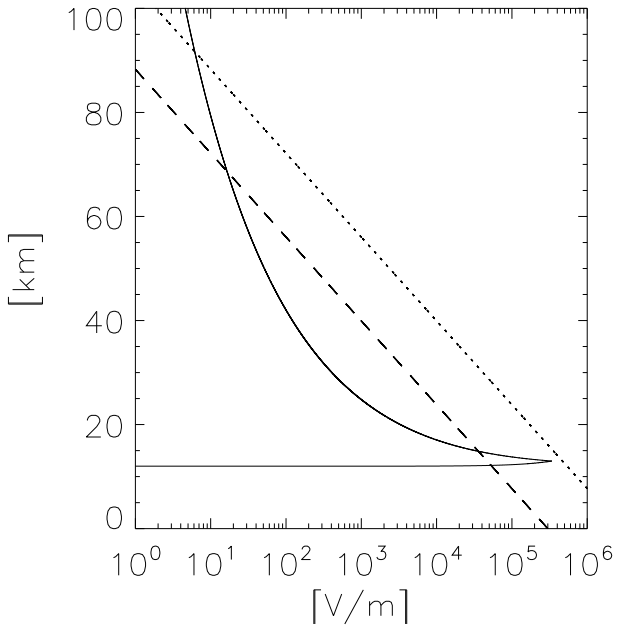

Figure 4.4: A simplified model of the electric field, E, after an intra cloud lightning is shown in solid. The threshold for RREA, E_t ,is dashed and the threshold for conventional breakdown, E_k, is dotted.

Lehtinen et al. [1997] simulated runaway avalanches in QS fields and found that they could produce TGFs at heights of 60-70 km. Their simulations result were comparable to those measured by BATSE if the lightning brought > 250 C from cloud to ground. In a later study *Lehtinen et al.* [1999] found that if the geomagnetic field was included in the simulations the QS field could only produce TGFs below ~ 40 km altitude. At altitudes > 40 km the electrons gyro frequency around magnetic field lines are larger than the collision frequency such that one cannot accelerate the electrons in the electric field direction and gain the required energy for runaway avalanches. To produce the photon fluxes measured at satellite altitudes the theoretical models for QS needed extremely high charge moment change (~ 2500 Ckm) from the lightning making the QS field [*Lehtinen et al.*, 2001]. This indicates that TGFs produced by QS fields should be a rare phenomena, which was consistent with the low BATSE detection rate (78 TGFs in eight years), but not with the more recent observation by RHESSI, Fermi

and AGILE. Also, the mean charge moment change found in lightning associated with TGFs by the *Cummer et al.* [2005] is 49 Ckm which is far less than the ($\sim$ 2500 Ckm) needed in the QS model. *Gurevich et al.* [2004] suggested that QS fields inside a thundercloud at $<$ 20 km altitude could produce TGFs. But due to atmospheric attenuation this theory also needs very large charge moment to make enough initial photons in a TGFs that are detectable at satellite altitude. However, *Gurevich et al.* [2004] did not include feedback effects in this estimate. How feedback would change their results are not studied.

4.4.2 TGF produced by an electromagnetic pulse

The TGF observations by RHESSI reported 10-20 TGFs per month [*Smith et al.*, 2005]. The increased number of observed TGFs could not be explained by the QS-field model and therefore *Inan and Lehtinen* [2005] suggested that TGFs could be produced in the electrical fields from an electromagnetic pulse (EMP) emitted by the lightning return stroke. However, their model implies very high peak currents with peak currents ($>$ $450-700$ kA) and fast return strokes (99-99.5% the speed of light). Such lightnings are rare and they concluded that EMP fields could produce $\sim 6-8$ TGFs per day which is less than the estimate of $\sim$ 50 TGFs per day by *Smith et al.* [2005] and far less than more recent estimates like 220-250 TGFs per day [*Fuschino et al.*, 2011] and $>$ 50.000 TGFs per day [*Østgaard et al.*, 2012].

4.4.3 The relativistic feedback discharge model

The relativistic feedback discharge model of (RFD) terrestrial gamma ray flashes is developed by Dwyer in numerous papers [*Dwyer*, 2003, 2007, 2012]. As shown in table 4.2 the avalanche growth factor in electric field varying from $\sim 2.5-10$ times E_t provides fewer electrons than the $10^{16}-10^{18}$ required in an average RHESSI TGF. Only if the total potential is in the order of $\sim$ 400 MV and the electrical field is close to the conventional breakdown threshold (E_k) the needed number of electrons by RREA can be obtained. As discussed in section 4.2 such fields are not likely to occur in thunderstorms.

The feedback idea was presented in *Dwyer* [2003] where he modelled RREA involving positive feedback effects from positrons and photons. In this model the runaway electrons produce X- and gamma-rays that may be backscattered via Compton scattering. The downward propagating photons may then create secondary avalanches via Compton scattering and photoelectric absorption. Alternatively, the gamma-photons in a RREA may produce positrons via pair production. Such positrons may turn around and propagate in the opposite direction of the electric field. As a result one would get runaway positrons which create secondary avalanches. Via this positive feedback effects the runaway discharge may become self sustaining leading to a dramatic increase in the number of produced relativistic electrons. Figure 4.5 shows a Monte Carlo simulations from *Dwyer* [2007] where runaway electrons trajectories are black and positrons are blue. The top panel contain particles at time $t < 0.5$ μs ,the middle at $t < 2$ μs and bottom at $t < 10$ μs. The figure shows how rapidly the RFD model increases the number of runaway electrons and leads to a breakdown of the electric field.

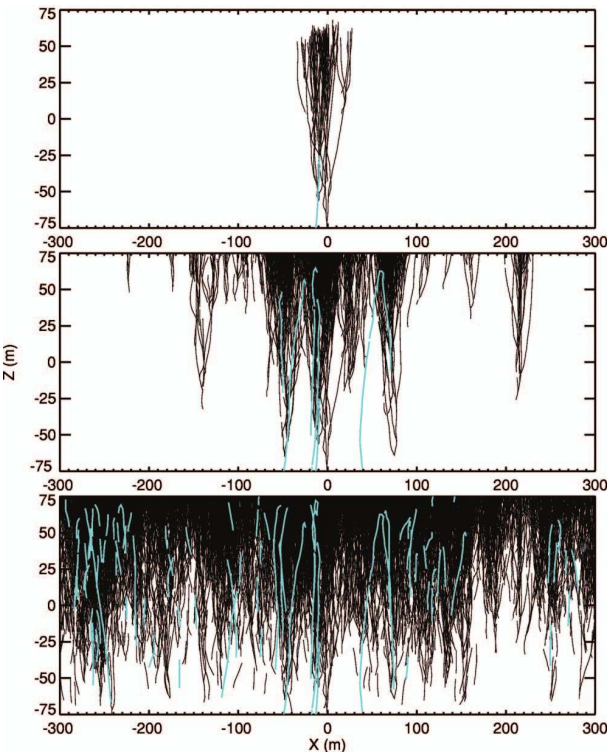

Figure 4.5: RFD in a 750 kV/m electric field at STP air. Black trajectory are runaway electrons and blue are positrons traveling back and creating new avalanches. Top panel is for time $t < 0.5$ μs , middle $t < 2$ μs and bottom $t < 10$ μs. The figure is from *Dwyer* [2007].

The feedback factor, γ_D, is defined as the number of runaway electrons in an avalanched divided by the number of runaway electrons in the previous avalanche. If $\gamma_D = 1$ the avalanche will be self-sustaining. If $\gamma_D > 1$ the number of runaway electrons will grow with time, and discharge the electric field.

In order for RFD to be efficient in the production of TGF high potential is needed [*Carlson et al.*, 2009]. The potential used in RFD are typically 200-400 MV, but *Dwyer* [2012] have found that RFD can generate a TGF in potential as low as 50 MV if the average electric field is near the conventional breakdown field. This would correspond to an electric field of $\sim 3 \times 10^6$ V/m over a region of < 20 m in STP air and $\sim 1 \times 10^6$ over < 60 m at 8 km altitude.

The RFD model of TGFs suggests that the runaway electrons in a TGF produce large currents. *Dwyer* [2012] estimated this current to be comparable to or larger than the currents produced in IC lightnings and consequently emits sferic of VLF-frequency. *Dwyer* [2012] further suggests that ground based lightning detection network such as WWLLN misidentifies the sferic from TGFs as lightning discharges. This could explain the close connection which has been found between TGF and sferics [*Connaughton et al.*, 2010; *Cohen et al.*, 2010b; *Collier et al.*, 2011]. Also, a new type of sferic related to TGFs are recently discovered. *Cummer et al.* [2011] found a strong temporal connection between the Fermi gamma-ray count rate and a slower process sferics data. This slow process could be the signature expected from the TGF producing electron avalanche [*Dwyer*, 2012].

4.4.4 Cold relativistic runaway electron avalanches

Cold RREA suggest that thermal electrons are accelerated over the peak of the friction force, which is shown in figure 4.1. This means that the electric field locally has to be above ~ 280 kV/cm. A significant work by *Moss et al.* [2006] show that it is possible for electrons to become runaway in the strong fields around streamer and leader tips. They're simulations show that the electric field in the streamer tip may be $\sim 10E_k$, which is the field needed to push the thermal electrons over the peak in the friction force and into the runaway regime. Production of thermal runaway electrons in streamers and leaders are also found in other theoretical studies e.g *Chanrion and Neubert* [2008, 2010].

In a leader step *Moss et al.* [2006] estimate the runaway electron production rate to 10^{18} s^{-1} which is $\sim 10^{12}$ for a 1 μs leader step. In a survey of relevant lightning physics *Carlson et al.* [2009] suggests that TGFs are produced in a current pulse. In this mechanism a current pulse would create cold runaway electrons that are seeded in the strong electric field close to the leader tip or leader channel and undergo RREA. Due to the high number of seed electrons $\sim 10^{12}$ only 'small' ($\sim 10^4 - 10^6$) avalanche multiplication is needed to make a TGF observable in space.

Further investigations of cold runaway is done by *Celestin and Pasko* [2011]. They have found that it is possible to gain $\sim 10^{17}$ energetic electrons in a corona streamer flash from a negative leader such that no further avalanche multiplication is needed. The duration of a corona flash is short (~ 10 μs). Therefore *Celestin and Pasko* [2012] suggest that Compton dispersion of photons, as described in *Østgaard et al.* [2008], will make the event ~ 50 μs when observed at satellite altitudes. A TGF duration of 50 μs is consistent with the new results from Fermi [*Fishman et al.*, 2011]. The longer events,

such as the estimate from *Gjesteland et al.* [2010] which found that the BATSE TGF was ~ 250 μs at origin, are explained by *Celestin and Pasko* [2012] as overlapping emissions from individual leader steps. In each leader step a TGF is emitted, and if the time between the leader steps is small the dispersion by Compton scattering would combine the individual events into one TGF at satellite altitude.

4.5 Summary of TGF production theories

When TGFs were first discovered they're origin were placed at > 40 km altitude [*Nemiroff et al.*, 1997] and they were though to be related to read sprites. Also, because the high attenuation of gamma in the atmosphere *Nemiroff et al.* [1997] argued that altitudes above 40 km are the most likely source for TGFs. As a consequence Wilson's original idea about the QS field above thunderclouds was suggested to produced TGFs. However, due to the influence of the geomagnetic field, it was shown that the QS-model could not produce TGFs above ~ 40 km altitude [*Gurevich et al.*, 2004; *Lehtinen et al.*, 1999]. The idea that TGFs were produced in a QS field below 40 km altitude was rejected since the model needed extremely high charge moment changes to make a TGF detectable in space [*Lehtinen et al.*, 2001]. The idea that TGFs were produced in the electric field from an EMP can explain TGF produced at altitudes > 40 km, but this idea also require strong lightning discharges and it can only account for some of the TGF observations [*Inan and Lehtinen*, 2005].

The spectral analysis of TGFs [*Dwyer*, 2005; *Carlson et al.*, 2007; *Østgaard et al.*, 2008; *Gjesteland et al.*, 2010] all suggest that TGFs are produced below ~ 20 km altitude. These results are also an argument against the QS model at high altitude and the EMP model.

As shown in section 4.2 the avalanche multiplication factor are too low to produce TGFs. It is therefore suggested that cosmic ray secondary particles could act as seed particles to increase this number to the required $10^{16} - 10^{18}$ electrons. The number of relativistic seed particles from cosmic rays are typically $\sim 10^6$ per TGF [*Carlson et al.*, 2008]. However, this number may increase significantly if a very high energy cosmic ray deposit its energy at the right place at the right time. But such cosmic rays are too rear to account for the number of TGFs detected so far [*Carlson et al.*, 2008]. *Dwyer* [2008] Also concludes that an external sources of seed particles, such as cosmic rays, are insufficient to account for TGF fluxes.

Today there the most compelling theories are that TGFs are either produced via cold RREA or by the RFD model of TGF. The RFD model assumes that the TGFs are emitted as the lightning leaders develops between the main charge regions of the thunder cloud [*Dwyer*, 2012]. This implies that the TGF should occur before the lightning. If very accurate VLF data are available it may be possible to test whether TGFs do occur before the lightning. However, *Dwyer* [2012] suggests that the RREA itself produce a sferic which is observable in VLF radio and that VLF detectors will misinterpreter this pulse emitted by RREA as the lightning. *Dwyer* [2012] suggests that the slow radio pulse measured by *Cummer et al.* [2011] is evidence for the latter.

RFD can also explain the multi pulse TGFs, which is common in the BATSE measurements, but not in RHESSI. The main problem with RFD is the required potential needed to make feedback important. *Dwyer* [2012] shows that typically values are 200-

400 MV which is less than the measured values in thunderstorms ($\sim$ 100 MV [*Marshall and Stolzenburg*, 2001]). It is, however, still not known what the maximum potential in thunderstorms is [*Dwyer*, 2012].

In the new search of the RHESSI data *Gjesteland et al.* [2012] found more than twice as many TGFs as previously reported. *Østgaard et al.* [2012] studied the relative detection rates between RHESSI and Fermi and argue that one cannot reject the hypothesis that all lightning produce TGFs. These studies indicates that TGFs are a common phenomenon and therefore may be produced in thunderstorms with lower potentials than needed in the RFD model. More studies of potentials in thunder clouds are needed to address this question.

In the RFD model *Dwyer* [2012] assumes that the TGFs are produced in the ambient field between the main charge regions of the thundercloud. As shown in section 4.4.1, with the simplified model of a QS-field, it is also possible for RFD to be efficient in the QS field of a modest IC lightning. When *Lehtinen et al.* [2001] rejected the QS model at < 40 km altitude, they did not include feedback effects. Whether or not their conclusions would change if they included feedback effects should be investigated further. If RFD occur in a QS field one would expect the TGFs to be emitted towards the end of, or after the lightning discharge.

Experiments have found X-rays in laboratory sparks. Both *Rahman et al.* [2008] and *Nguyen et al.* [2008] have used a 1 MV Marx generator to produce $\sim$ 1 m long sparks in STP air. Both studies reports of X-ray emission together with the spark. It is also found that lightning leader steps emits gamma-rays. *Moore et al.* [2001] found burst of gamma radiation before three negative lightning strokes. They suggest that the gamma emission were associated with the leader step. With a collimated gamma-detector *Dwyer et al.* [2011] measured gamma photons emitted from the tip of the lightning leader as it propagates down towards the ground. These observations, together with the results from laboratory sparks are manifestations that cold runaway electrons are produced in leaders and streamers. The question is whether or not cold runaway acceleration are effective enough to make the amount of photons and the high photon energies that is measured in a TGF.

The width of the initial photon emission in a TGF is suggested to be $30^\circ - 40^\circ$ [*Gjesteland et al.*, 2011]. This is also consistent with the results from *Carlson et al.* [2007] and *Hazelton et al.* [2009]. Such emission implies that the electric field is vertical or nearly vertical ($< 20^\circ$ from vertical) orientated electric field. Both RFD and the simulation from *Celestin and Pasko* [2012], where TGF are suggested to be produced in the electrical field from leaders, implies comparable spatially broadening of the gamma emissions.

One can not reject the hypothesis that both RFD and cold runaway accelerations are involved in the production of TGFs. In the RFD model it is assumed that the TGFs occurs while the lightning leaders develops. It would be interesting to investigate how the RFD model is modified when cold runaway seeding are included, and whether seeding from streamers and leaders are more important than the increase in the avalanche growth factor due to feedback.

4.6 Terrestrial Electron Beams

Lehtinen et al. [2000, 2001] found that the runaway electrons that produces TGF, and the knock off electrons from Compton scattering, could escape the atmosphere. Such electrons will be bounded to the geomagnetic field and escape the Earth's atmosphere as a beam. Figure 4.6 shows a possible TGF electron beam first found by *Smith et al.* [2006]. This event occurred event on January 17, 2004 when RHESSI was over the Sahara dessert, which is not a place where one expects to find lightning activity. They suggest that this was an electron beam coming from the conjugate hemisphere. As shown in figure 4.6 the lightcurve shows two pulses. The first pulse is the direct electron beam coming from the conjugate hemisphere while the second pulse is electrons which have mirrored due to the increase in magnetic field strength and moves upwards again.

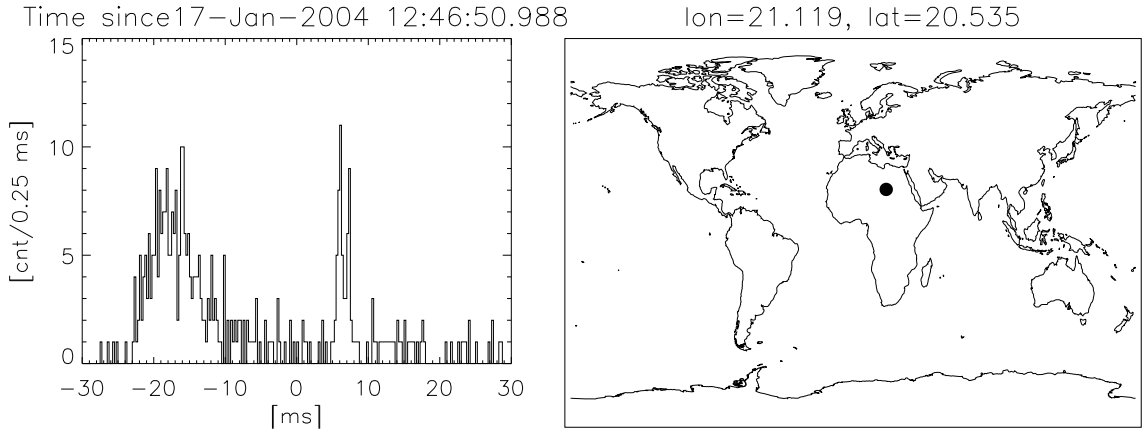

Figure 4.6: The lightcurve of the electron beam on Januar 17 2004. The map shows the RHESSI sub-satellite point a the time of the detection.

Similar events are also found in BATSE. *Dwyer* [2008] suggests that six of the 36 BATSE TGFs they analysed were electron beams. *Briggs et al.* [2011] identified electron beams measured by Fermi GBM. Spectral analysis from these electron beams shows strong 511 keV positron annihilation lines, which indicates that a significant portion (estimated to 11 %) of the particles that escape the atmosphere are positrons created by pair production. The electron beams measured by Fermi GBM were also connected to specific lightning strokes, which were from the most intense part of the distribution (peak current) of their thunderstorms [*Cohen et al.*, 2010c].

Carlson et al. [2011] have simulated electrons beams produced by TGFs and estimated the ratio of detected TGFs per electron beam for satellite borne instruments. This ratio was measured to 5 (30 TGF and 6 electron beams) for BATSE [*Dwyer et al.*, 2008] and 13 (77 TGFs and 6 electron beams) for Fermi [*Briggs et al.*, 2011]. This large fraction of electron beams are most likely biased due to the long trigger windows in BATSE and Fermi. If the ratio is 10 then it implies that the effective observation radius for TGF observation by satellite instrument are $\leq$ 100 km [*Carlson et al.*, 2011, Figure 5], which is not consistent with the geolocation of TGFs, which find TGFs out to $\sim$ 800 km from the sub satellite point [*Cohen et al.*, 2010b; *Collier et al.*, 2011]. In comparing there have, so far, only been identified one electron beam in the RHESSI data [*Smith et al.*, 2006] (Figure 4.6).

Chapter 5

Summary of papers

5.1 Paper I: Production altitude and time delays of the terrestrial gamma flashes: Revisiting the Burst and Transient Source Experiment spectra

The motivation for this paper was, for the first time, to do spectral analysis of individual TGFs. Previously spectral analysis of TGFs had only used superposed spectrum [*Dwyer and Smith*, 2005; *Carlson et al.*, 2007], and the effect of mixing spectra observed at different angles were not known. At this time it was also an open question whether TGFs were produced at high altitude, as the BATSE data indicated [*Fishman et al.*, 1994; *Nemiroff et al.*, 1997], or at lower altitudes as the more recent RHESSI data indicated [*Dwyer and Smith*, 2005; *Cummer et al.*, 2005; *Carlson et al.*, 2007].

A Monte Carlo simulation, which accounted for photoelectric absorption, Compton scattering, pair production and bremsstrahlung from Compton electrons, were developed. The Monte Carlo simulation were tested against the GEANT simulation tool with good agreement. The simulation inputs were different production altitudes and initial distributions of photons spatial and spectral.

Only based on the simulations several features of TGFs were discovered. The energy spectrum has a low energy cut off which moves to lower energies as the production altitude increases. Also the energy spectra of TGFs at large angles has a softer energy spectrum which is a result of Compton scattering. The time dispersion between high and low energy photons as described by *Feng et al.* [2002] are also found in the simulations if the production altitude are below ~ 20 km. This is also explained as an effect of Compton scattering. The high energy photons have a more straight way through the atmosphere than the lower energy photons. Lower energy photons that escape the atmosphere were originally of higher energies, but reduced in energy as they were Compton scattered on their way from the production altitude to the satellite.

By comparing the simulation results to the BATSE measurements the production altitude were determined to be below 20 km. However, a significant portion of the TGFs were found to be produced at higher altitudes e.g. $30-40$ km. These TGFs were single pulse with high fluxes.

It is also found a softening in the BATSE spectra for increasing observation angles. This is also interpreted as an effect of Compton scattering. Assuming a narrow emission of the photons in a TGF, only scattered photons, which are reduced in energy, are

detected at large angles.

5.2 Paper II: Effects of dead-time losses on terrestrial gamma ray flash measurements with the Burst and Transient Source Experiment

Shortly after the analysis of the BATSE data by *Østgaard et al.* [2008] is was shown that BATSE suffered from dead-time saturation [*Grefenstette et al.*, 2008]. By comparing the peak fluxes in BATSE and RHESSI *Grefenstette et al.* [2008] found that BATSE TGFs could have ~ 4 times higher peak fluxes than measured. These findings questioned all results based on the BATSE measurements. Since BATSE operates in a trigger mode, with long trigger window (64 ms) compared to the duration of TGFs, BATSE was biased to multi pulse TGFs. The single pulse TGFs needed very high fluxes to be triggered. Therefore, in order to quantify the effect of the dead-time saturation, five single pulse BATSE TGFs were re-analysed.

Based on pre-flight measurements and documentation *Grefenstette et al.* [2008] showed that BATSE were a paralyzable detector with energy dependent dead-time. In Paper II the properties of the BATSE read-out electronics were implemented in a Monte Carlo model.This Monte Carlo model was used to determine the effects of dead-time in BATSE.

The main result is that the energy spectrum becomes softer for increased losses due to dead-time. In a TGF the high energy photons arrive before the low energy photos due to the Compton dispersion as described in *Østgaard et al.* [2008]. Since the high energy photons arrive earlier, at the time when the flux in the TGFs are the highest, mostly high energy photons are lost due to dead-time. The later arriving Compton tail are not as influenced by the dead-time losses.

When the dead-time corrected simulated spectrum are compared to BATSE measurements it results in a lower estimated production altitude. All the single pluse TGFs with high fluxes are now determined to be produced < 20 km altitude.

Since BATSE was a paralysable detecor it is also found that a double pulse TGF measured by BATSE were in fact a single pulse. But since the dead-time losses increases dramatically for high fluxes this TGF may be measured as a double pulse. If this is the case, this TGF is in fact 6 times brighter than measured.

By only investigating the highest energy channel of BATSE (>300 keV) an estimate of the TGF production time were made. These 5 single pulse TGF are estimated to last between $200 - 555$ μs, which is less than the previously assumed ~ 1 ms duration and consistent with later detailed analyses of Fermi TGFs [*Fishman et al.*, 2011; *Briggs et al.*, 2010].

5.3 Paper III: Confining the Angular Distribution of Terrestrial Gamma-ray Flash Emission

The basic idea in this study is that the initial angular distribution of the TGF emission will reflect the electric fields that produces TGFs.

The 106 TGFs, which were geolocated by AWESOME [*Cohen et al.*, 2010b] and WWLLN [*Collier et al.*, 2011], were available for this study. To compare these measurements to simulations two approaches were used. First the the distribution of observation angles, which is the angle between RHESSI nadir and a straight line to the source lightning, which is assumed to be the location where the TGFs are produced, are compared to a simulation of the expected observation angle distribution. In the simulations assumptions were made about the TGFs energy spectrum, production altitude, spatially distribution and intensity distribution. The energy spectrum were assumed to be a RREA spectrum ($dn/d\varepsilon \propto 1/\varepsilon$). The production altitude were from 15-20 km and the spatially distribution were assumed to be isotropical within a cone with half angle ranging from $10^\circ - 60^\circ$. The initial number of photons in each TGF were assumed to be distributed according to a power law, which is shown to be feasible [*Collier et al.*, 2011], with the spectral index ranging from 1.5 to 3. With these assumptions the Monte Carlo simulations from *Østgaard et al.* [2012] were used to simulate the photons through the atmosphere. At satellite altitude all TGFs which have a fluence larger than the detection threshold where included in the simulated observation angle distribution. This distribution is a competition between the area, which is increasing at increasing observation angle, and the TGF fluence, which is decreasing at increasing observation angle.

The simulated observation angle distribution were compared to the observed distribution with a Kolmogorov-Smirnov two-sample test and it shows that simulations where the photons were emitted within a cone with half angle $> 30^\circ$ can represent the measurements.

The dataset contained 10 TGFs which were observed at large angles ($> 40^\circ$). The spectrum from these TGFs were superposed and compared to simulated spectra. The superposed RHESSI spectrum of TGF measured at large angles is significantly softer than the superposed RHESSI spectrum from smaller angles. This is also found in simulations were the emission cone had a half angle $< 40^\circ$.

With the results from the observation angle distribution and the results from the spectral analysis of TGFs measured at large angles *Gjesteland et al.* [2011] confine the TGF emission to a cone with half angle of $30^\circ - 40^\circ$.

If one assumed that the TGF intensities are distributed as a power law the simulations found that the spectral index of the intensity distribution is confined within 1.9 and 2.5.

5.4 Paper IV: A new method reveals more TGFs in the RHESSI data

I has been suggested in the TGF community that the instruments so far has only detected the tip of the iceberg. Meaning that if one increases the sensitivity of ones instrument the number of detected TGFs would increase significantly. For example the increase from the 78 TGFs found in BATSE to the ~ 1000 found by RHESSI is due to a better sensitivity in RHESSI since RHESSI do not work in a trigger mode. Also Fermi GBM increased the number of identified TGFs when the sensitivity threshold was reduced [*Briggs*, 2011].

In the RHESSI catalog paper *Grefenstette et al.* [2009] present results from an additional search algorithm applied on the RHESSI data. The algorithm is not described

and neither is the quality and number of new events quantified. But it clearly indicates that there are more TGFs in the RHESSI data than presented in the RHESSI catalog. This was the motivation to develop a new search algorithm and apply it on the raw RHESSI data. The new search algorithm were based on Poison statistic with search windows 0.3 ms, 1 ms and 3 ms. Also the possible events had to pass five selection criteria which were based on properties of TGFs from the RHESSI catalog and other measurements.

In the RHESSI data from 2004, 2005 and 2006 the new algorithm identified 1012 TGFs. This is more than twice as many as in the RHESSI catalog, which presented 474 for the same period. The new TGFs follows the same seasonal and geographical variation as previously identified TGFs, and they also follow the seasonal pattern of lightning activity.

The new RHESSI TGFs have also been matched with WWLLN sferics by the method as presented in *Collier et al.* [2011]. Of the 1012 new TGFs 91 were matched with WWLLN events. This is comparable with the results presented in *Collier et al.* [2011].

5.5 Paper V: The true fluence distribution of terrestrial gamma flashes at satellite altitude

Since *Gjesteland et al.* [2012] found more than twice as many TGFs by relaxing the search algorithm, this study's motivation was to determine how big the 'iceberg' of TGFs actually is. It is important to know how common TGFs are in order to put constrains on the production mechanism.

If one assume that the fluence distribution of TGFs follows a power law as suggested by *Collier et al.* [2011], one expects that RHESSI and Fermi GBM are mesuring TGFs from the same distribution. However, the two instruments have different orbits, effective area and sensitivity threshold. If these differences are corrected for one can compare the daily TGF detection rate to obtain the true fluence distribution. By this method *Østgaard et al.* [2012] show that the TGF fluence distribution follows a power law with spectral index 2.3 ± 0.2 at satellite altitudes.

It is known that RHESSI suffers from losses due to dead-time [*Grefenstette et al.*, 2008] (se section 3.6). The losses due to dead-time are most significant for the events with highest fluxes. As a consequence the weak TGF are hardly influenced by dead-time losses, while the stronger ones are. If one fits a power law curve to the measured fluence distribution of RHESSI, one get a spectral index of 3.5, which is larger than the 2.3 mentioned above. Therefore a simulation to calculate the losses due to dead-time were applied on the RHESSI measurements. This method clearly shows that the TGFs with highest fluence suffer more from dead-time losses than the TGFs with lower fluence. A power law fit to the dead-time corrected RHESSI fluence distribution is found to have a spectral index between 2.3 and 3.0. The dead-time corrected RHESSI fluence distribution also shows indications of a roll off with a spectral index of 1.7 for the lower part of the distribution.

The fluence distribution at the source are found to be different than the measured fluence distribution at satellite altitude. If one uses the method from *Carlson et al.*

[2012] one find that the spectral index for the distribution at the production altitude is shifted to lower spectral indexes. E.g. if the true fluence distribution in space have a spectral index 2.3 ± 0.2, which the results in *Østgaard et al.* [2012] indicates, than the fluence distribution at the production altitude have a spectral index 2.0 ± 0.2.

If one assume a sharp cut-off at 5/600 of the RHESSI sensitivity threshold and that the true TGF fluence distribution of TGFs follows a power law with spectral index 2.0 the estimated number of TGFs within $\pm 38^\circ$ latitude are 50.000 TGFs/day, which is $\sim 2\%$ of all IC lightning. If one assumes a roll off with spectral index 1.7 at satellite altitudes which corresponds to 1.3 at the source one cannot reject the hypothesis that all lightning produces TGF. Both the scenarios above are consistent with the results from ADELE, which only detected one TGF even if the detector was within 10 km of 1213 lightning flashes [*Smith et al.*, 2011].

The results are also consistent with *Gjesteland et al.* [2012] who identified more than twice as many TGFs by reducing the lower detection threshold from ~ 17 counts per TGF, as used by *Grefenstette et al.* [2009], to ~ 12 counts per TGFs, which are the weakest TGFs found in the new search by *Gjesteland et al.* [2012].

This paper also shows that the dead-time losses in an average RHESSI TGF is $\sim 25\%$.

Bibliography

Abarca, S. F., K. L. Corbosiero, and T. J. jr. Galarneau (2010), An evaluation of the Worldwide Lightning Location Network (WWLLN) using the National Lightning Detection Network (NLDN) as ground truth, *Journal of Geophysical Research*, *115*, doi:10.1029/2009JD013411. 3.5

Briggs, M. S. (2011), More TGFs from GBM, in *paper presented at Terrestrial Gamma-Ray Flash Workshop 2011, Cent. for Space Plasma and Aeron. Res., Univ. of Ala., Huntsville.* 3.3, 5.4

Briggs, M. S., et al. (2010), First results on terrestrial gamma ray flashes from the Fermi Gamma-ray Burst Monitor, *Journal of Geophysical Research*, *115*(A7), doi:10.1029/2009JA015242. 3.3, 3.3, 5.2

Briggs, M. S., et al. (2011), Electron-positron beams from terrestrial lightning observed with Fermi GBM, *Geophysical Research Letters*, *38*(2), doi:10.1029/2010GL046259. 4.6

Carlson, B. E., N. G. Lehtinen, and U. S. Inan (2007), Constraints on terrestrial gamma ray flash production from satellite observation, *Geophysical Research Letters*, *34*(8), doi:10.1029/2006GL029229. 3.1, 3.2, 4.5, 5.1

Carlson, B. E., N. G. Lehtinen, and U. S. Inan (2008), Runaway relativistic electron avalanche seeding in the Earth's atmosphere, *Journal of Geophysical Research*, *113*(A10307), doi:10.1029/2008JA013210. 2.3, 4.5

Carlson, B. E., N. G. Lehtinen, and U. S. Inan (2009), Terrestrial gamma ray flash production by lightning current pulses, *Journal of Geophysical Research*, *114*, A00E08, doi:10.1029/2009JA014531. 4.4.3, 4.4.4

Carlson, B. E., T. Gjesteland, and N. Østgaard (2011), Terrestrial gamma-ray flash electron beam geometry, fluence, and detection frequency, *Journal of Geophysical Research*, *116*(A11), doi:10.1029/2011JA016812. 4.6

Carlson, B. E., T. Gjesteland, and N. Østgaard (2012), Connecting the terrestrial gamma-ray flash source strength and observed fluence distributions, *Journal of Geophysical Research*, *117*(A1), doi:10.1029/2011JA017122. 5.5

Celestin, S., and V. P. Pasko (2011), Energy and fluxes of thermal runaway electrons produced by exponential growth of streamers during the stepping of lightning leaders and in transient luminous events, *Journal of Geophysical Research*, *116*(A3), doi:10.1029/2010JA016260. 4.4.4

Celestin, S., and V. P. Pasko (2012), Compton scattering effects on the duration of terrestrial gamma-ray flashes, *Geophysical Research Letters*, *39*(2), doi:10.1029/2011GL050342. 4.4.4, 4.5

Chanrion, O., and T. Neubert (2008), A PIC-MCC code for simulation of streamer propagation in air, *Journal of Computational Physics*, *227*(15), 7222–7245, doi:10.1016/j.jcp.2008.04.016. 4.4.4

Chanrion, O., and T. Neubert (2010), Production of runaway electrons by negative streamer discharges, *Journal of Geophysical Research*, *115*, doi:10.1029/2009JA014774. 4.4.4

Christian, H. J. (2003), Global frequency and distribution of lightning as observed from space by the Optical Transient Detector, *Journal of Geophysical Research*, *108*(D1), doi:10.1029/2002JD002347. 3.2, 4.3.1

Cohen, M., U. Inan, and E. Paschal (2010a), Sensitive Broadband ELF/VLF Radio Reception With the AWESOME Instrument, *IEEE Transactions on Geoscience and Remote Sensing*, *48*(1), doi:10.1109/TGRS.2009.2028334. 3.5

Cohen, M. B., U. S. Inan, and G. Fishman (2006), Terrestrial gamma ray flashes observed aboard the Compton Gamma Ray Observatory/Burst and Transient Source Experiment and ELF/VLF radio atmospherics, *Journal of Geophysical Research*, *111*(D24), doi:10.1029/2005JD006987. 3.5

Cohen, M. B., U. S. Inan, R. K. Said, and T. Gjestland (2010b), Geolocation of terrestrial gamma-ray flash source lightning, *Geophysical Research Letters*, *37*(2), doi:10.1029/2009GL041753. 3.5, 3.5, 4.4.3, 4.6, 5.3

Cohen, M. B., U. S. Inan, R. K. Said, M. S. Briggs, G. J. Fishman, V. Connaughton, and S. A. Cummer (2010c), A lightning discharge producing a beam of relativistic electrons into space, *Geophysical Research Letters*, *37*(L18806), doi:10.1029/2010GL044481. 4.6

Coleman, L. M., and J. R. Dwyer (2006), Propagation speed of runaway electron avalanches, *Geophysical Research Letters*, *33*(11), doi:10.1029/2006GL025863. 4.2

Collier, A. B., T. Gjesteland, and N. Østgaard (2011), Assessing the power law distribution of TGFs, *Journal of Geophysical Research*, *116*(A10), doi:10.1029/2011JA016612. (document), 3.5, 3.5, 3.8, 4.4.3, 4.6, 5.3, 5.4, 5.5

Connaughton, V., et al. (2010), Associations between Fermi Gamma-ray Burst Monitor terrestrial gamma ray flashes and sferics from the World Wide Lightning Location Network, *Journal of Geophysical Research*, *115*(A12), doi:10.1029/2010JA015681. 3.3, 3.5, 4.4.3

Cummer, S. A., Y. Zhai, W. Hu, D. M. Smith, L. I. Lopez, and M. A. Stanley (2005), Measurements and implications of the relationship between lightning and terrestrial gamma ray flashes, *Geophysical Research Letters*, *32*(8), doi:10.1029/2005GL022778. 3.2, 3.5, 3.5, 4.4.1, 5.1

Cummer, S. A., G. Lu, M. S. Briggs, V. Connaughton, S. Xiong, G. J. Fishman, and J. R. Dwyer (2011), The lightning-TGF relationship on microsecond timescales, *Geophysical Research Letters*, *38*(14), doi:10.1029/2011GL048099. 3.5, 4.4.3, 4.5

Dwyer, J. R. (2003), A fundamental limit on electric fields in air, *Geophysical Research Letters*, *30*(20), doi:10.1029/2003GL017781. 4.2, 4.4.3

Dwyer, J. R. (2005), The initiation of lightning by runaway air breakdown, *Geophysical Research Letters*, *32*(20), doi:10.1029/2005GL023975. 3.1, 4.3, 4.5

Dwyer, J. R. (2007), Relativistic breakdown in planetary atmospheres, *Physics of Plasmas*, *14*(4), doi:10.1063/1.2709652. (document), 4.2, 4.4.3, 4.5

Dwyer, J. R. (2008), Source mechanisms of terrestrial gamma-ray flashes, *Journal of Geophysical Research*, *113*(D10), doi:10.1029/2007JD009248. 3.1, 4.5, 4.6

Dwyer, J. R. (2012), The relativistic feedback discharge model of terrestrial gamma ray flashes, *Journal of Geophysical Research*, *117*(A2), doi:10.1029/2011JA017160. 3.5, 4.2, 4.4.3, 4.4.3, 4.5

Dwyer, J. R., and D. M. Smith (2005), A comparison between Monte Carlo simulations of runaway breakdown and terrestrial gamma-ray flash observations, *Geophysical Research Letters*, *32*(22), doi:10.1029/2005GL023848. 3.2, 4, 5.1

Dwyer, J. R., B. W. Grefenstette, and D. M. Smith (2008), High-energy electron beams launched into space by thunderstorms, *Geophysical Research Letters*, *35*(2), doi:10.1029/2007GL032430. 4.6

Dwyer, J. R., M. Schaal, H. K. Rassoul, M. a. Uman, D. M. Jordan, and D. Hill (2011), High-speed X-ray images of triggered lightning dart leaders, *Journal of Geophysical Research*, *116*(D20), doi:10.1029/2011JD015973. 4.5

Eack, K. B., W. H. Beasley, W. D. Rust, T. C. Marshall, M. Stolzenburg, and M. C. S. Norman (1996), Initial results from simultaneous observation of X rays and electric fields in a thunderstorm, *Journal of Geophysical Research*, *101*(D23), 637–640. 2.3

Feng, H., T. P. Li, M. Wu, M. Zha, and Q. Q. Zhu (2002), Temporal and spectral properties of gamma-ray flashes, *Geophysical Research Letters*, *29*(3), doi:10.1029/2001GL013992. 3.1, 5.1

Fishman, G. J., et al. (1994), Discovery of Intense Gamma-Ray Flashes of Atmospheric Origin, *Science*, *264*(5163), 1313–1316. 1, 2.2, 2.3, 3.1, 3.1, 3.5, 5.1

Fishman, G. J., et al. (2011), Temporal properties of the terrestrial gamma-ray flashes from the Gamma-Ray Burst Monitor on the Fermi Observatory, *Journal of Geophysical Research*, *116*(A7), doi:10.1029/2010JA016084. 2.3, 3.3, 4.4.4, 5.2

Fuschino, F., et al. (2011), High spatial resolution correlation of AGILE TGFs and global lightning activity above the equatorial belt, *Geophysical Research Letters*, *38*(14), doi:10.1029/2011GL047817. 3.4, 4.4.2

Gjesteland, T., N. Østgaard, P. H. Connell, J. Stadsnes, and G. J. Fishman (2010), Effects of dead time losses on terrestrial gamma ray flash measurements with the Burst and Transient Source Experiment, *Journal of Geophysical Research*, *115*, doi: 10.1029/2009JA014578. 1, 3.1, 3.1.1, 3.2.1, 4.4.4, 4.5

Gjesteland, T., N. Østgaard, A. B. Collier, B. E. Carlson, M. B. Cohen, and N. G. Lehtinen (2011), Confining the Angular Distribution of Terrestrial Gamma-ray Flash Emission., *Journal of Geophysical Research*, *116*, doi:10.1029/2011JA016716. 1, 3.2, 3.5, 3.5, 4.5, 5.3

Gjesteland, T., N. Østgaard, a. B. Collier, B. E. Carlson, C. Eyles, and D. M. Smith (2012), A new method reveals more TGFs in the RHESSI data, *Geophysical Research Letters*, *39*(5), doi:10.1029/2012GL050899. (document), 1, 3.2, 3.4, 3.2, 3.5, 3.5, 4.5, 5.5

Grefenstette, B. W., D. M. Smith, J. R. Dwyer, and G. J. Fishman (2008), Time evolution of terrestrial gamma ray flashes, *Geophysical Research Letters*, *35*(6), doi: 10.1029/2007GL032922. 3.1, 3.1, 3.1.1, 3.1.1, 3.1.1, 3.2.1, 5.2, 5.5

Grefenstette, B. W., D. M. Smith, B. J. Hazelton, and L. I. Lopez (2009), First RHESSI terrestrial gamma ray flash catalog, *Journal of Geophysical Research*, *114*(A2), doi: 10.1029/2008JA013721. (document), 1, 2.3, 3.2, 3.2, 3.4, 3.2.1, 3.5, 5.4, 5.5

Gurevich, A., Y. Medvedev, and K. P. Zybin (2004), Thermal electrons and electric current generated by runaway breakdown effect, *Physics Letters A*, *321*(3), 179–184, doi:10.1016/j.physleta.2003.10.062. 4.4.1, 4.5

Gurevich, A. V., and K. P. Zybin (2005), Runaway Breakdown and the Mysteries of Lightning The observed electric fields in thunder, *Physics Today*, *May*, 37–43. 4.3

Gurevich, A. V., G. M. Milikh, and R. Roussel-Dupré (1992), Runaway electron mechanism of air breakdown and preconditioning during a thunderstorm, *Physics Letters A*, *165*, 463–468, doi:10.1016/0375-9601(92)90348-P. 2.3, 4.2

Gurevich, A. V., J. A. Valdivia, G. M. Milikh, and K. Papadopoulos (1996), Runaway electrons in the atmosphere in the presence of a magnetic field, *Radio Science*, *31*(6), 1541–1554. 2.3

Hazelton, B. J., B. W. Grefenstette, D. M. Smith, J. R. Dwyer, X.-M. Shao, S. a. Cummer, T. Chronis, E. H. Lay, and R. H. Holzworth (2009), Spectral dependence of terrestrial gamma-ray flashes on source distance, *Geophysical Research Letters*, *36*(1), doi:10.1029/2008GL035906. 3.2, 4.5

Inan, U. S., and N. G. Lehtinen (2005), Production of terrestrial gamma-ray flashes by an electromagnetic pulse from a lightning return stroke, *Geophysical Research Letters*, *32*(19), doi:10.1029/2005GL023702. 4.4.2, 4.5

Inan, U. S., S. C. Reising, G. J. Fishman, and J. M. Horack (1996), On the association of terrestrial gamma ray bursts with lightning and implications for sprites, *Geophysical Research Letters*, *23*(9), 1017–1020. 3.5

Inan, U. S., M. B. Cohen, R. K. Said, D. M. Smith, and L. I. Lopez (2006), Terrestrial gamma ray flashes and lightning discharges, *Geophysical Research Letters*, *33*(18), doi:10.1029/2006GL027085. 3.5

Knoll, G. (1989), *Radiation Detection and Measurements*, John Wiley, New York. 3.1.1

Lehtinen, N. G., M. Walt, U. S. Inan, T. F. Bell, and V. P. Pasko (1996), gamma ray emission produced by a relativistic beam of runaway electrons accelerated by quasi electrostatic thundercloud fields, *Geophysical Research Letters*, *23*(19), 2645–2648. 4.4.1

Lehtinen, N. G., T. F. Bell, V. P. Pasko, and U. S. Inan (1997), A two dimensional model of runaway electron beams driven by quasi electrostatic thundercloud fields, *Geophysical Research Letters*, *24*(21), 2639–2642, doi:10.1029/97GL52738. 4.4.1

Lehtinen, N. G., T. F. Bell, and U. S. Inan (1999), Monte Carlo simulation of runaway MeV electron breakdown with application to red sprites and terrestrial gamma ray flashes, *Journal of Geophysical Research*, *104*(A11), 24,699–24,712, doi:10.1029/1999JA900335. 4.4.1, 4.5

Lehtinen, N. G., U. S. Inan, and T. F. Bell (2000), Trapped energetic electron curtains produced by thunderstorm driven relativistic runaway electrons, *Geophysical Research Letters*, *27*(8), 1095–1098. 4.6

Lehtinen, N. G., U. S. Inan, and T. F. Bell (2001), Effects of thunderstorm driven runaway electrons in the conjugate hemisphere: Purple sprites, ionization enhancements, and gamma rays, *Journal of Geophysical Research*, *106*(A12), 28,841–28,856, doi:10.1029/2000JA000160. 4.4.1, 4.5, 4.6

Lu, G., et al. (2010), Lightning mapping observation of a terrestrial gamma-ray flash, *Geophysical Research Letters*, *37*(11), doi:10.1029/2010GL043494. 3.5

Lu, G., S. A. Cummer, J. Li, F. Han, D. M. Smith, and B. W. Grefenstette (2011), Characteristics of broadband lightning emissions associated with terrestrial gamma ray flashes, *Journal of Geophysical Research*, *116*(A3), doi:10.1029/2010JA016141. 3.5

MacGorman, D. R., and W. D. Rust (1998), *The electrical nature of storms*, Oxford University Press. 4.3

Marisaldi, M., et al. (2010a), Detection of terrestrial gamma ray flashes up to 40 MeV by the AGILE satellite, *Journal of Geophysical Research*, *115*, doi:10.1029/2009JA014502. 1, 2.3, 3.4, 4

Marisaldi, M., et al. (2010b), Gamma-Ray Localization of Terrestrial Gamma-Ray Flashes, *Physical Review Letters*, *105*(12), doi:10.1103/PhysRevLett.105.128501. 3.4

Marshall, T. C., and M. Stolzenburg (2001), Voltages inside and just above thunderstorms, *Journal of Geophysical Research*, *106*(D5), 4757–4768, doi:10.1029/2000JD900640. 4.2, 4.3, 4.5

Mccarthy, M., and G. K. Parks (1985), Further observations of X-rays inside Thunderstorms, *Physics*, *12*(6), 393–396. 2.3, 4.2

Moore, C. B., K. B. Eack, G. D. Aulich, and W. Rison (2001), Energetic radiation associated with lightning stepped-leaders, *Geophysical Research Letters*, *28*(11), 2141–2144. 4.5

Moss, G. D., V. P. Pasko, N. Liu, and G. Veronis (2006), Monte Carlo model for analysis of thermal runaway electrons in streamer tips in transient luminous events and streamer zones of lightning leaders, *Journal of Geophysical Research*, *111*(A2), doi: 10.1029/2005JA011350. (document), 4.1, 4.4.4

Nemiroff, R. J., J. T. Bonnell, and J. P. Norris (1997), Temporal and spectral characteristics of terrestrial gamma flashes, *Journal of Geophysical Research*, *102*(A5), 9659–9665. 3.1, 3.1, 4.5, 5.1

Nguyen, C. V., a. P. J. van Deursen, and U. Ebert (2008), Multiple x-ray bursts from long discharges in air, *Journal of Physics D: Applied Physics*, *41*(23), doi:10.1088/0022-3727/41/23/234012. 4.5

Østgaard, N., T. Gjesteland, J. Stadsnes, P. H. Connell, and B. Carlson (2008), Production altitude and time delays of the terrestrial gamma flashes: Revisiting the Burst and Transient Source Experiment spectra, *Journal of Geophysical Research*, *113*(A2), doi:10.1029/2007JA012618. 1, 3.1, 3.1.1, 3.2, 4.4.4, 4.5, 5.2

Østgaard, N., T. Gjesteland, R. S. Hansen, a. B. Collier, and B. Carlson (2012), The true fluence distribution of terrestrial gamma flashes at satellite altitude, *Journal of Geophysical Research*, *117*(A3), doi:10.1029/2011JA017365. 1, 3.2.1, 4.4.2, 4.5, 5.3, 5.5

Parks, G. K., B. H. Mauk, R. Spiger, and J. Chin (1981), X-ray enhancements detected during thunderstorm and lightning activities, *Geophysical Research Letters*, *8*(11), 1176–1179. 2.3

Pasko, P., U. S. Inan, Y. N. Taranenko, and F. Bell (1995), Heating, ionization and upward discharges in the mesosphere due to intense quasi-electrostatic thundercloud fields, *Geophysical Research Letters*, *22*(4), 365–368. 4.4.1

Rahman, M., V. Cooray, N. A. Ahmad, J. Nyberg, V. a. Rakov, and S. Sharma (2008), X rays from 80-cm long sparks in air, *Geophysical Research Letters*, *35*(6), doi: 10.1029/2007GL032678. 4.5

Rakov, V. A., and M. A. Uman (2003), *Lightning Physics and Effect*, Cambridge University Press. (document), 3.5, 4.3, 4.2, 4.3, 4.3.1

Rodger, C. J., J. B. Brundell, and R. L. Dowden (2005), Annales Geophysicae Location accuracy of VLF World-Wide Lightning Location (WWLL) network : Post-algorithm upgrade, *Annales Geophysicae*, *23*, 1–14, doi:1432-0576/ag/2005-23-1. 3.5

Roussel-Dupré, R., and A. V. Gurevich (1996), On runaway breakdown and upward propagating discharges, *Journal of Geophysical Research*, *101*(A2), 2297–2311. 2.3

Roussel-Dupré, R. A., A. V. Gurevich, T. Tunnell, and G. M. Milikh (1994), Kinetic theory of runaway air breakdown, *Physical review E*, *49*(3), 2257–2271. 2.3

Rycroft, M. (2000), The global atmospheric electric circuit, solar activity and climate change, *Journal of Atmospheric and Solar-Terrestrial Physics*, *62*(17-18), 1563–1576, doi:10.1016/S1364-6826(00)00112-7. 4.4.1

Shao, X.-M., T. Hamlin, and D. M. Smith (2010), A closer examination of terrestrial gamma-ray flash-related lightning processes, *Journal of Geophysical Research*, *115*(April 2004), doi:10.1029/2009JA014835. 3.5

Smith, D. M., L. I. Lopez, R. P. Lin, and C. P. Barrington-Leigh (2005), Terrestrial gamma-ray flashes observed up to 20 MeV., *Science*, *307*(5712), 1085–8, doi:10.1126/science.1107466. 1, 3.2, 4, 4.4.2

Smith, D. M., et al. (2006), The Anomalous Terrestrial Gamma-ray Flash of 17 January 2004, *EOS Transactions AGU Fall Meeting Supplement*, *87*(52), Abstract AE31A—-1040. 4.6, 4.6

Smith, D. M., B. J. Hazelton, B. W. Grefenstette, J. R. Dwyer, R. H. Holzworth, and E. H. Lay (2010), Terrestrial gamma ray flashes correlated to storm phase and tropopause height, *Journal of Geophysical Research*, *115*, doi:10.1029/2009JA014853. 3.2

Smith, D. M., et al. (2011), The rarity of terrestrial gamma-ray flashes, *Geophysical Research Letters*, *38*(8), doi:10.1029/2011GL046875. 5.5

Splitt, M. E., S. M. Lazarus, D. Barnes, J. R. Dwyer, H. K. Rassoul, D. M. Smith, B. Hazelton, and B. Grefenstette (2010), Thunderstorm characteristics associated with RHESSI identified terrestrial gamma ray flashes, *Journal of Geophysical Research*, *115*, doi:10.1029/2009JA014622. 3.2

Stanley, M. a., X.-M. Shao, D. M. Smith, L. I. Lopez, M. B. Pongratz, J. D. Harlin, M. Stock, and A. Regan (2006), A link between terrestrial gamma-ray flashes and intracloud lightning discharges, *Geophysical Research Letters*, *33*(6), doi:10.1029/2005GL025537. 3.5

Tavani, M., et al. (2011), Terrestrial Gamma-Ray Flashes as Powerful Particle Accelerators, *Physical Review Letters*, *106*(1), doi:10.1103/PhysRevLett.106.018501. 3.4

Williams, E., et al. (2006), Lightning flashes conducive to the production and escape of gamma radiation to space, *Journal of Geophysical Research*, *111*(D16), doi:10.1029/2005JD006447. 3.2

Williams, E. R. (2006), Problems in lightning physics—the role of polarity asymmetry, *Plasma Sources Science and Technology*, *15*(2), S91–S108, doi:10.1088/0963-0252/15/2/S12. 4.3

Williams, E. R. (2010), The Origin and Context of C . T . R . Wilson ' s Ideas on Electron Runaway in Thunderclouds, *Journal of Geophysical Research*, *115*, doi: 10.1029/2009JA014581. 2.1

Wilson, C. T. R. (1924), The electric field of a thundercloud and some of its effects, *Proc. R. Soc. London A*, *37*, 32D–37D. 2.1, 4.1, 4.2

Wilson, C. T. R. (1925), The Acceleration of β-particles in Strong Electric Fields such as those of Thunderclouds, *Proc. Cambridge Philos. Soc.*, *22*, 534–538. 2.1, 2.2

List of abberviations

ADELE	Airborne Detector for Energetic Lightning Emissions
AGILE	Astrorivelatore Gamma a Immagini Leggero
ASIM	Atmosphere-Space Interactions Monitor
AWESOME	Atmospheric Weather Electromagnetic System for Observation, Modelling, and Education
BATSE	Burst and Transient Source Experiment
CG	Cloud to Ground (lightning)
CGRO	Compton Gamma Ray Observatory
ELF	Extremely Low Frequency
EMP	Electromagnetic pulse
GBM	Gamma-ray Burst Monitor
GRB	Gamma Ray Burst
IC	Intra cloud (lightning)
LAD	Large Area Detector
LASA	Los Alamos Sferic Array
LAT	Large Area Telescope
LIS	Lightning Imaging Sensor
LMA	Lightning Mapping Array
MCAL	Mini-Calorimeter
OTD	Optical Transient Detector
QS	Quasi electro-static
RREA	Relativistic Runaway Electron Avalanche
RFD	Relativistic Feedback Discharge
RHESSI	Reuven Ramaty High Energy Solar Spectroscopic Imager
SAMA	South Atlantic Magnetic Anomaly
STP	Standard Temperature and Pressure
TARANIS	Tool for the Analysis of Radiations from lightNIng and Sprites
TGF	Terrestrial Gamma ray Flash
TLE	Transient Luminous Event
TOGA	Time of Group Arrival
ULF	Ultra Low Frequency
UT	Universal Time
VLF	Very low Frequency
WWLLN	World Wide Lightning Location Network

Chapter 6

Scientific results

6.1 Paper I

Production altitude and time delays of the terrestrial gamma flashes: Revisiting the Burst and Transient Source Experiment spectra
N. Østgaard, T. Gjesteland, J. Stadsnes, P. H. Connell, and B. E. Carlson

J. Geophys. Res. , 113, A02307, doi:10.1029/2007JA012618, 2008

JOURNAL OF GEOPHYSICAL RESEARCH, VOL. 113, A02307, doi:10.1029/2007JA012618, 2008

Production altitude and time delays of the terrestrial gamma flashes: Revisiting the Burst and Transient Source Experiment spectra

N. Østgaard,[1] T. Gjesteland,[1] J. Stadsnes,[1] P. H. Connell,[2] and B. Carlson[3]

Received 29 June 2007; revised 20 September 2007; accepted 31 October 2007; published 19 February 2008.

[1] On the basis of the RHESSI results it has been suggested that terrestrial gamma flashes (TGFs) are produced at very low altitudes. On the other hand some of the Burst and Transient Source Experiment (BATSE) spectra show unabsorbed fluxes of X rays in the 25–50 keV energy range, indicating a higher production altitude. To investigate this, we have developed a Monte Carlo code for X-ray propagation through the atmosphere. The most important features seen in the modeled spectra are (1) a low-energy cutoff which moves to lower energies as TGFs are produced at higher altitudes, (2) a high-energy cutoff which moves to lower energies as TGFs are observed at larger zenith angles, and (3) time delays are observed for TGFs produced at $\leq$20 km (and some at 30 km) altitude when observed at larger zenith angle than the half-angle defining the initial isotropic X-ray beam. This is a pure Compton effect. The model results and an optimization procedure are used to estimate production altitudes of the BATSE TGFs. The main findings are (1) half or more of the BATSE TGFs are produced at low altitudes, $\leq$20 km, (2) a significant portion of the BATSE TGFs are produced at higher altitudes, 30 km to 40 km, (3) for the TGFs produced at $\leq$20 km (and some at 30 km) altitudes the dispersion signatures can be explained as a pure Compton effect, and (4) the softening of the BATSE spectra for increasing zenith angles and the time dispersions both indicate that the initial TGF distribution is beamed.

Citation: Østgaard, N., T. Gjesteland, J. Stadsnes, P. H. Connell, and B. Carlson (2008), Production altitude and time delays of the terrestrial gamma flashes: Revisiting the Burst and Transient Source Experiment spectra, *J. Geophys. Res.*, *113*, A02307, doi:10.1029/2007JA012618.

1. Introduction

[2] Following the discovery of the terrestrial gamma flashes (TGF) [*Fishman et al.*, 1994] by the Burst and Transient Source Experiment (BATSE) on the Compton Gamma Ray Observatory (CGRO), there has been a debate about their production mechanism. Despite many unresolved questions there seems to be a consensus that these very short lived flashes ($\sim$1 ms) of photon energies up to 20 MeV [*Smith et al.*, 2005] are in fact bremsstrahlung produced by a beam of relativistic runaway electrons (RRE) produced above large thunderstorm systems. The controversy, however, is whether the electrons are accelerated by the quasi-static electric field (QES) following large positive cloud-to-ground lightening strokes [e.g., *Gurevich and Zybin*, 2001] or other mechanisms like the electromagnetic impulses (EMP) suggested by *Inan and Lehtinen* [2005]. When TGFs were first discovered, the QES theory was considered as the most likely production mechanism [*Fishman et al.*, 1994]. However, the shape of measured spectra did not give a consistent picture for such an interpretation. While the QES mechanism is thought to be most important closer to cloud top at 10–20 km, many of the spectra did not show the expected absorption signatures at low photon energies. Consequently, many BATSE spectra indicate a higher production altitude. This argument was repeated by *Nemiroff et al.* [1997] who performed a more detailed analysis of the spectral and temporal behavior of the BATSE measurements. They based their conclusion on the statement that the atmosphere is not very transparent for X-rays produced below 40 km. This mismatch of altitudes resulting from QES theory and observations were further modeled by *Lehtinen et al.* [1997, 1999, 2001] who found that QES mechanism could only be efficient up to 20 km at most. These findings motivated the EMP theory [*Inan and Lehtinen*, 2005] which allows for a production altitude of 50 km to 60 km. On the other hand the model results presented by *Roussel-Dupré and Gurevich* [1996] indicate that the electric field above thundercloud after an intracloud strike can exceed the threshold electric field for runaway process at two altitudes, one just above the thundercloud and the other at 40–60 km. New observational evidence of

[1]Department of Physics and Technology, University of Bergen, Bergen, Norway.
[2]Institute of Mechanical Science, University of Valencia, Valencia, Spain.
[3]Electric Engineering, STAR Laboratory, Stanford University, Stanford, California, USA.

0148-0227/08/2007JA012618

the TGFs have been provided by the Reuven Ramaty High Energy Solar Spectroscopic Imager (RHESSI). Owing to a more effective trigger algorithm, RHESSI has been able to observe 10–20 TGF per month, while BATSE reported about 70 over a 9-year period. On the other hand, BATSE measured typically 100 counts/TGF [*Nemiroff et al.*, 1997] due to larger detector area and provided spectral information about the individual TGF while the typical RHESSI event only have 20–30 counts/TGF. Thus in order to study the spectral shape of the RHESSI observations, all observed TGFs were superposed and, based on a Monte Carlo simulation, *Dwyer and Smith* [2005] found that the superposed spectrum was indicative of a production altitude of 15 km to 21 km. However, to obtain this result, they had to make assumptions about the spatial distribution of TGFs within the field of view of RHESSI, that is, the distribution of entering angles, which depends on production altitude, X-ray propagation, and instrument sensitivity. Discussing the missing attenuation signatures at low energies in many of the BATSE spectra, they also considered the possibility that there might be two types of TGFs, a low-altitude TGF and a high-altitude TGF. If the latter is true, the superposition of all the RHESSI spectra will mix the two types of spectra. A similar approach, that is, adding all RHESSI spectra and averaging over all BATSE entering angles, was used by *Carlson et al.* [2007], who found the most likely production altitude to be 15 km to 20 km and that the X-ray beam most likely was initially isotropic within a half-angle of 45° in contrast to the highly beamed initial X-ray distribution suggested by *Cummer et al.* [2005] and *Stanley et al.* [2006].

[3] To avoid the mixing of two possible types of TGFs and take advantage of the higher sensitivity as well as directional information from the BATSE measurements, we have revisited the BATSE spectra and performed a careful Monte Carlo (MC) simulation of the available individual spectra and their dispersion signatures. It will be shown that the information about entering angles is important and can help us understand the temporal behavior of TGF. Furthermore, information about entering angles has implications for the spectral shape and consequently the inferred production altitude. This study is also motivated by the upcoming experiment, Atmosphere-Space Interaction Monitor (ASIM), that will carry an X-ray detector to the International Space Station to monitor the low-energy part of the TGFs. Our study does not model the production of TGF by the relativistic electrons, but examine how a given X-ray energy spectrum with a power law ≥ 1 produced at some altitude or distribution of altitudes propagate through the atmosphere and what the output spectrum will be observed at different escaping angles at the top of the atmosphere. All effects that affect the propagation are taken into account, that is, absorption, Compton scattering and energy degradation, pair production, and new X rays produced by positrons and electrons.

2. BATSE Spectra and Time Profile

2.1. BATSE Measurements

[4] The BATSE spectra from the Large Area Detector are sampled in four bins with energy bins 24–60 keV, 60–110 keV, 110–320 keV, and 320–22,206 keV. Although the energy resolution of the BATSE spectra is not very good, this instrument was sensitive to X rays down to about 25 keV. As the absorption effects on X rays at low energies is assumed to be a strong indicator of production altitude, these measurements are the only ones, to date, where the expected fall-off at low energies can be used for altitude production estimates. Whereas *Nemiroff et al.* [1997] analyzed 13 spectra, we have found 21 spectra from the BATSE data base that had statistics good enough for the analysis presented in this paper. Furthermore, based on difference in counting rates in the eight various Large Area Detector of BATSE combined with the respond matrix for the instrument, the entering angle of the TGFs can be estimated. Our procedure will be described in section 4.

[5] Two BATSE spectra are shown in Figures 1a and 1b to illustrate the two types of spectra. The spectrum for trigger 2465 has a distinct fall-off at lower energies, indicating a production altitude deep in the atmosphere, whereas the spectrum for trigger 2144 does not resemble any signature of low energy absorption, even when the statistical error (vertical lines) are considered. One would assume that these two TGFs are produced at very different altitudes. This will be discussed later.

[6] Another significant result reported by *Nemiroff et al.* [1997] is the dispersion signatures which were present in most of the TGFs. In Figures 1c and 1d one can see the dispersion signatures for the same two trigger events. Dispersion signatures are seen for TGFs both with and without the low-energy cutoff. Figure 2 shows the distribution of time delays for the first three energy bins relative to the highest energy bin in 200 μs time bins for all the TGFs. While eight TGFs are in the $\pm$100 μs bin, 15 TGFs show a distinct dispersion signature of 100–300 μs, with an average of 240 μs. *Nemiroff et al.* [1997] reported time delays between 100 μs and 200 μs based on their 13 events.

3. Monte Carlo Simulations

[7] To model the BATSE spectra and dispersion signatures, we have developed a MC code for X-ray propagation through the atmosphere. The code takes into account photoelectric absorption, Compton scattering and energy degradation, pair production and, the most important contribution of new X-rays produced by pair-produced positrons and electrons. A detailed description of the code is given in Appendix A, and here we just give a brief overview of input, output and main features of the MC code. In our MC runs we initiate 1 or 5 million photons with six different power law distributions with an upper cutoff energy at 18 MeV produced at seven different discrete altitudes or distributed altitudes. Five million photons are only used for the lowest production altitudes, 10 km, 15 km, and 20 km, in order to obtain sufficient statistics of photons escaping the atmosphere. We let the power laws vary from 1 to 1.5, as the hardest spectrum that can be produced in the bremsstrahlung process is a power of 1. However, as will be seen the spectrum measured at the top of the atmosphere can be much harder than 1/E. In addition we run the code for two different initial angular distribution, one that is beamed vertically along z-axis and one isotropic within 20° solid angle. We sample the photons at the top of the atmosphere in seven different 10°-intervals of escaping angles, that is,

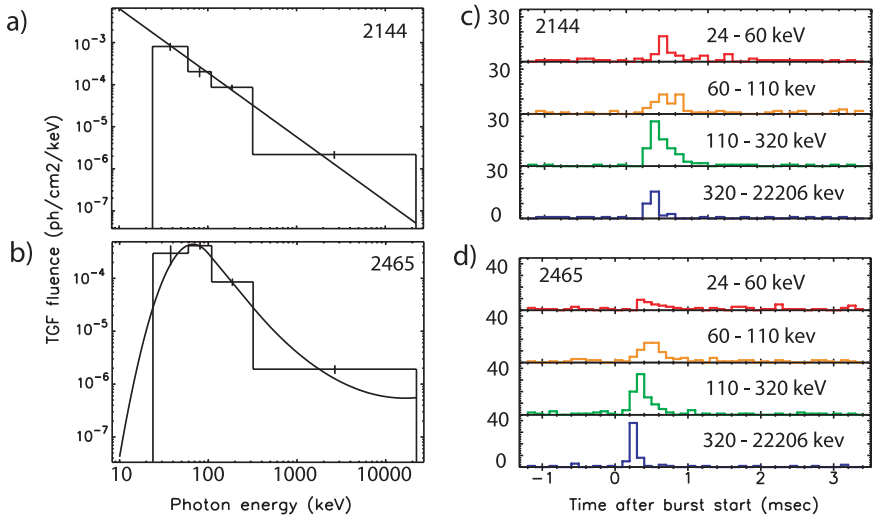

Figure 1. Two terrestrial gamma flashes (TGFs) measured by Burst and Transient Source Experiment (BATSE), showing (a and b) the spectra for trigger numbers 2144 and 2465 and (c and d) dispersion signatures for trigger number 2144 and 2465.

$\alpha = 0°–9°$, $10°–19°$, $20°–29°$,$30°–39°$, $40°–49°$, $50°–59°$ and $60°–69°$, that is, these are solid angle intervals. As explained in Appendix A2, this gives four libraries of a total of 1176 different spectra escaping the atmosphere. For each photon we keep track of energy, altitude, azimuth, zenith, radius from origin in xy-plane and the accumulated path length.

3.1. Comparison With GEANT

[8] The MC code is optimized to run fast and is much simpler (and faster) than the more complex GEANT code [*Agostinelli et al.*, 2003]. GEANT is a powerful Monte Carlo high-energy physics simulator used extensively in particle physics for detector design, radiation dosimetry, and predictive modeling. However, to verify our code, we have compared our results with GEANT for three different production altitudes. Both the GEANT runs and our MC runs are initiated with 1 million photons distributed as E^{-1} with cutoff at 10 keV and 10 MeV starting at three different discrete altitudes as a beam with $\alpha = 1°$.

[9] Besides showing almost identical profiles, the comparison shows that the total numbers of photons escaping the atmosphere only vary +3%, −2%, and +1% (MC versus GEANT). Although the differences are negligible, they can be explained by the exponential fit we use for the density profile, which misses the real density increase around 50 km,

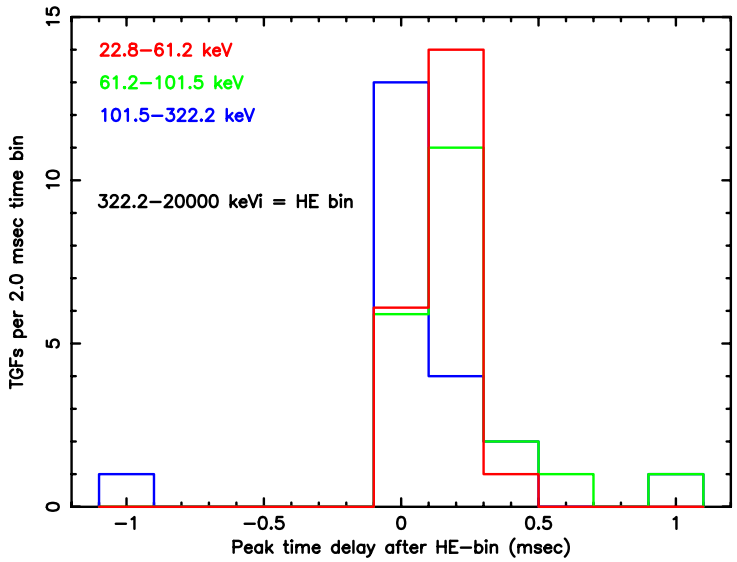

Figure 2. All 21 TGFs with peaking time in different energy bins relative to the high energy bin.

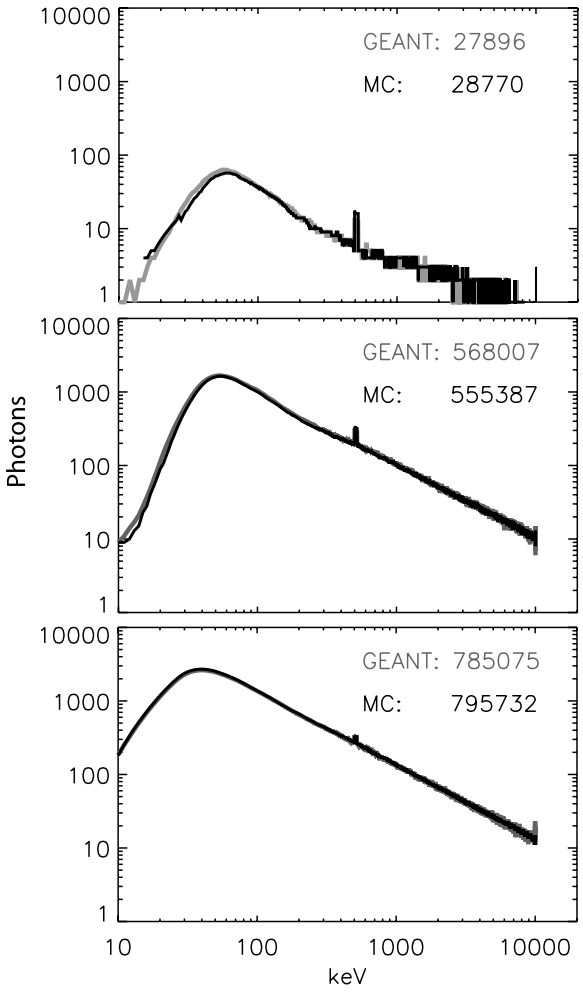

Figure 3. Comparison of the Monte Carlo code with the GEANT code for three different production altitudes, (a) 15 km, (b) 30 km, and (c) 40 km.

which was used for the GEANT run. We should emphasize at this point that we only model the X-ray propagation and not the original production of bremsstrahlung by runaway electrons. Thus only the new bremsstrahlung produced by pair-produced electrons are added to the X-ray distribution. Consequently, there is no electric field in either models accelerating the electrons produced by the pair production process.

3.2. Beamed Distributions From MC

[10] In Figure 4 we present the results for initial distributions of photons beamed at $\alpha = 0°$ produced at discrete altitudes (Figure 4, first, second, and third columns) compared with a distributed production altitude profile (Figure 4, fourth and fifth columns). The distributed production altitude profiles are shown in Figure A3 in Appendix A. The initial spectral distribution is E^{-1}. The photons are sampled at seven different escaping angle intervals (solid angle intervals due to the cylindric symmetry) at the top of the atmosphere.

[11] First, we want to focus on the spectra in the third and fourth columns. The spectrum in black is what we would see if we could sample all the photons escaping the atmosphere. The other lines are the spectra from escaping angles 0°–9° (light blue), 10°–19° (green), 20°–29° (light green), 30°–39° (orange), 40°–49° (red), 50°–59° (brown), and 60°–69° (blue).

[12] The following features in the spectra should be noticed.

[13] 1. Spectra from all production altitudes have a high-energy cutoff at decreasing energy for increasing escaping angle. This is due to the fact that the high-energy photons that escape the atmosphere have not interacted with the air, while lower-energy photons will experience multiple Compton scattering decreasing their energy and changing their direction. Thus the highest X-ray energies will only be measured if the initial X rays are beamed directly toward the detector. This is true for both the discrete altitude and the distributed altitude. Given that TGFs are initially beamed and randomly distributed in the field of view of any detector on a satellite it is more likely to observe TGFs at 40° escaping angle than at 0°. This implies that a distinct high-energy cutoff should be observed if one had the energy resolution or at least as a softening of the spectrum. This will be discussed later when we compare with the BATSE measurements.

[14] 2. For all escaping angles except 0°–9° the low-energy cutoff due to absorption gets steeper as the production occurs deeper in the atmosphere. The spectra from 60 km have a very broad energy peak compared to production at 15 km and 20 km.

[15] 3. The low-energy cutoff does not seem to depend very much on the assumption of a discrete altitude or a distributed altitude profile. This is somewhat surprising because in the distributed case some photons propagate through less air than in the discrete case and would be less affected by absorption. The similarities in shape indicate that the differences in absorption are insignificant as long as the peak production dominates.

[16] 4. If the TGFs are produced at very low discrete altitudes, for example, at 10 km or 15 km, there will be a

Figure 4. Distribution of photons beamed at $\alpha = 0°$, with a E^{-1} spectral distribution starting from four different altitudes (a) 15 km, (b) 20 km, (c) 40 km, and (d) 60 km. The first, second, and third columns show the result when all X rays are produced at discrete altitudes, while the fourth and fifth columns are the results when the X rays have distributed altitude profiles. The third and fourth columns show the spectra for different escaping angles (see text) and the first, second, and fifth columns show the predicted time delays at small escaping angles (first column) and at more likely escaping angles, that is, 40°–49° (second and fifth columns). The energy bins shown in Figure 4a, first column are used for all the panels in the first, second, and fifth columns. Y-axis is a linear scale (see Figure 4a, first column) with the number of photons as a scaling factor for each panel.

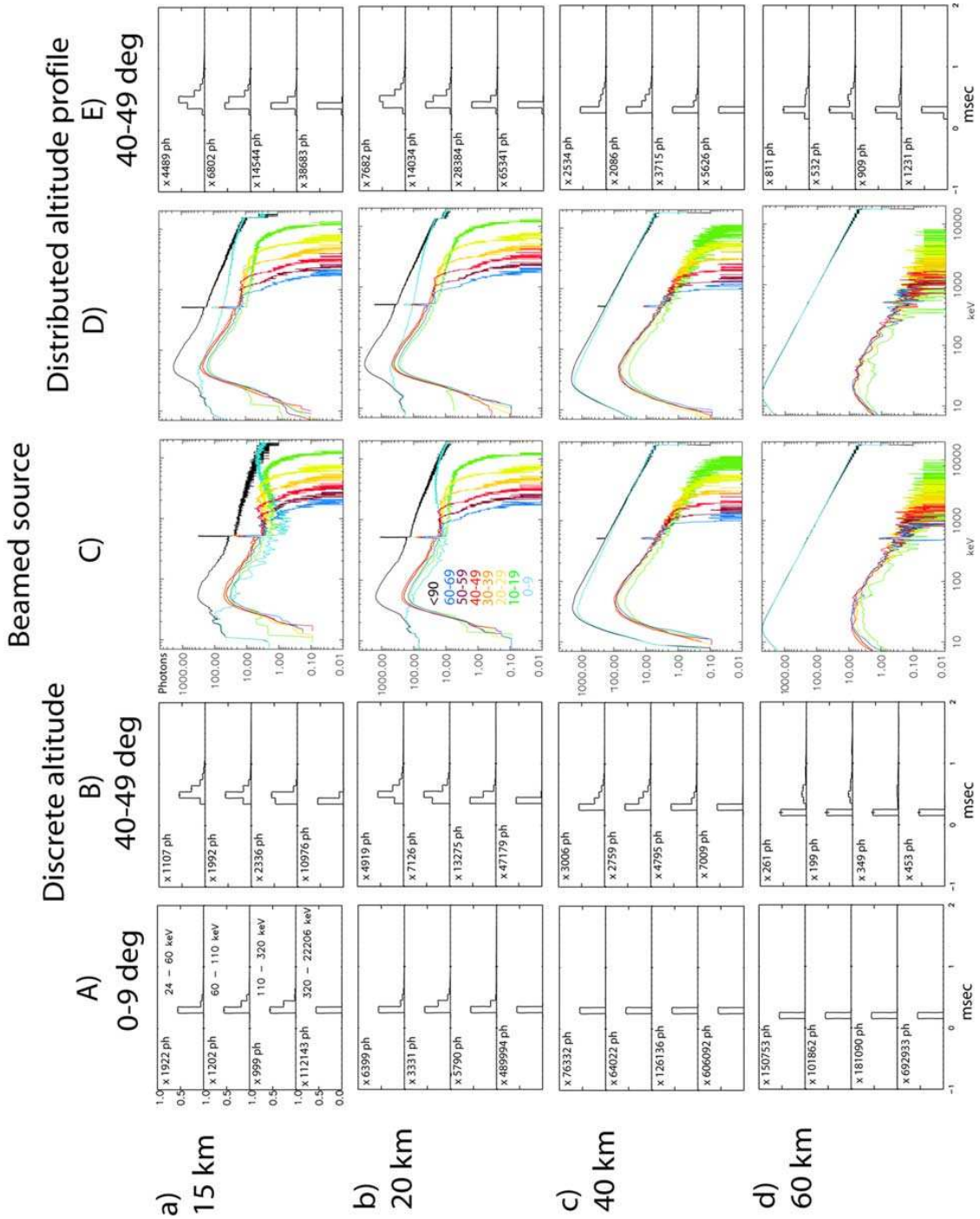
Beamed source
Discrete altitude
A)
0-9 deg
B)
40-49 deg
C)
Distributed altitude profile
D)
E)
40-49 deg
a)
15 km
b)
20 km
c)
40 km
d)
60 km
24 – 60 keV
60 – 110 keV
110 – 320 keV
320 – 22206 keV
Photons
msec
keV
<90
60-69
50-59
40-49
30-39
20-29
10-19
0-9

Figure 4

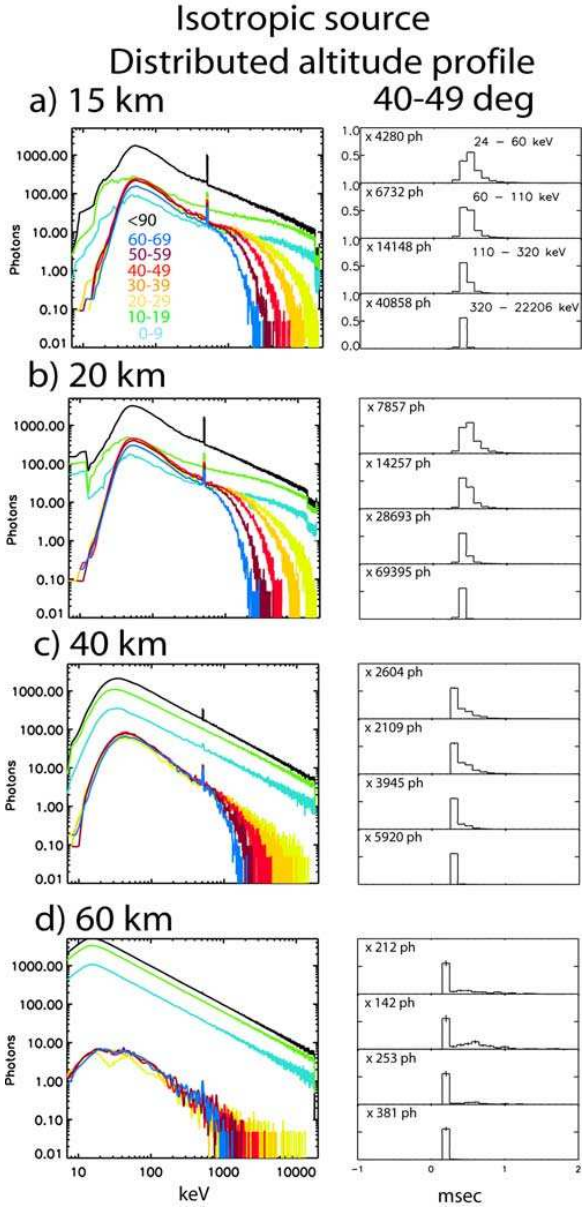

Figure 5. Distribution of photons isotropic within α = 20°, with a E^{-1} spectral distribution starting from four different altitudes (a) 15 km, (b) 20 km, (c) 40 km, and (d) 60 km. A distributed altitude profiles as in Figure 4, fourth and fifth columns, is used. The spectra are shown to the left, and the time profiles escaping at 40°–49° are shown to the right.

minimum around 0.7–1 MeV, see Figures 4a and 4b, third column. This minimum is very distinct for small escaping angles. This minimum, which is at lower energies (~500 keV) for the <90° curve they used, is what made *Dwyer and Smith* [2005] conclude that the RHESSI superposed spectra are most likely produced at very low altitudes. For the distributed altitude profile for 15 km and 20 km (Figures 4a and 4b, fourth column) there is not a minimum but a flattening of the spectra above ~500 keV.

[17] Now we turn to the predicted energy dispersion signatures. As we keep track of the accumulated path length before escaping the atmosphere at 100 km, the total time spent within the atmosphere is given for each photon as

$$t = \frac{s}{c} \tag{1}$$

where c is the speed of light and s is the accumulated path length. In the first, second, and fifth columns we show the time profiles for the photons in four different energy bins, which is the the same binning that was used for the BATSE measurements [*Nemiroff et al.*, 1997]. Time resolution is 100 μs and zero is the time of the TGF initiation at the production altitude. The counts have been normalized, but both the error bars (which are small and can only be seen in some of the plots) as well as the normalizing factor (i.e., the number in upper left corner) are indicated.

[18] The following features in the time profiles should be noticed:

[19] 1. Time delays of 100 μs can be seen for TGFs produced at 20 km and below when observed at the most likely zenith angles, 40°–49° (Figures 4a and 4b, third and fourth columns). For TGF produced at 30 km, only some escaping angles, that is, 30°–39°, show dispersion for all initial power indices, beamed and isotropic, while TGF produced at ≥40 km show no dispersion. The modeled dispersion signature is a pure Compton effect. The photons with low energies escaping the atmosphere are in fact initial high energy photons that have experienced multiple scattering and energy degradation. The high-energy photons escaping the atmosphere are the ones that propagated with only one or two interactions with air. Consequently, the low energy photons due to the multiple Compton scattering have a much longer accumulated path length than the high-energy photons.

[20] 2. If TGFs are observed at the same angle as they are produced, i.e., the instrument zenith angle and X-ray initial α angle are the same (for plane atmosphere), the majority of photons detected have not experienced any interaction with air, even from 10 km. However, as mentioned above, it is not very likely to observe TGFs at small escaping angles.

[21] 3. For TGFs produced at high altitudes (>30 km) and observed at large escaping angles, there are no peak in the time delay, but a tail can be seen at lower energies.

3.3. Isotropic Cone Distributions From MC

[22] Then we present (Figure 5) the results for photons with an initial isotropic angular distribution within a cone of α = 20°. The spectral distribution is again E^{-1} and a distributed altitude profile is used to make the results comparable with the two rightmost columns in Figure 4.

[23] Regarding both the spectra and time profiles the same features as pointed out for the beamed spectra can be seen. The only difference is that the high-energy cutoff now only appears for escaping angles larger than 20°. A detector sampling at angles smaller than the isotropy angle will see a mixture of directly escaping photons and photons that have experienced multiple Compton scattering. However, at sampling angles larger than the

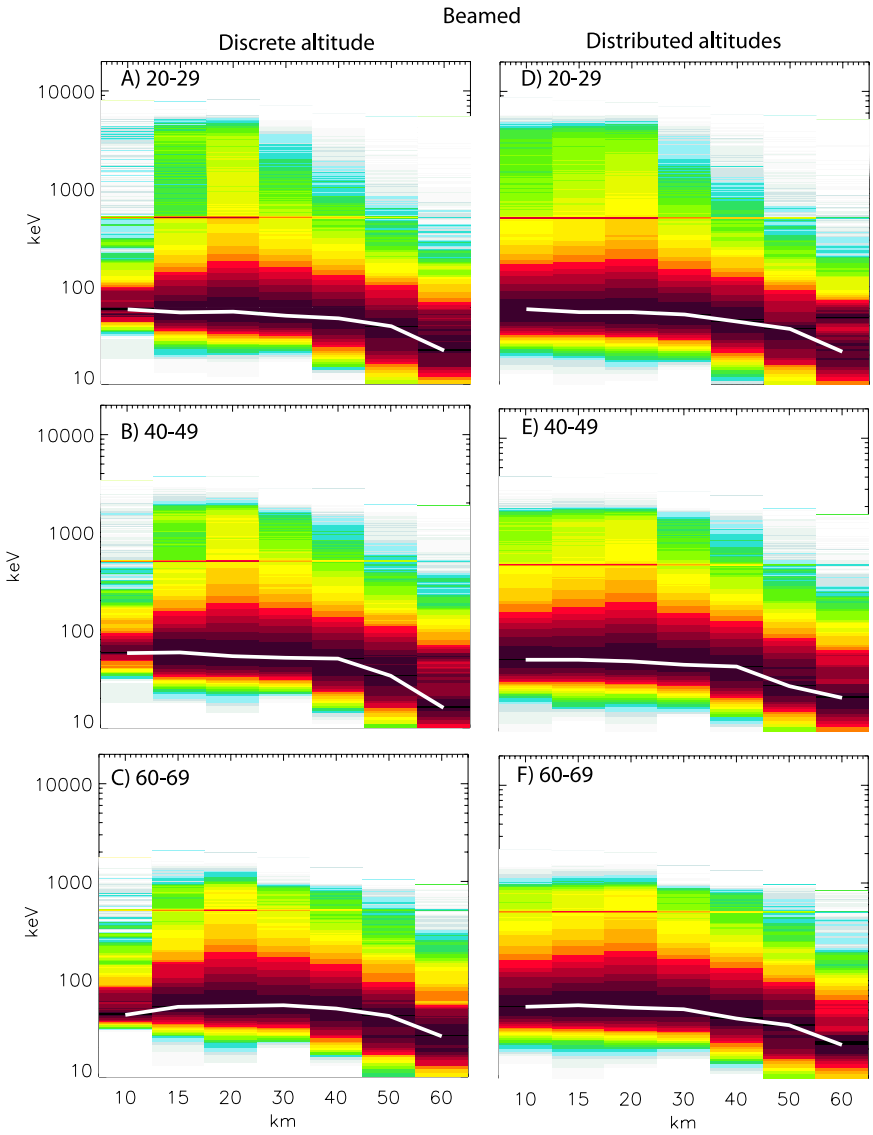

Figure 6. Spectrograms showing the energy spectra escaping the atmosphere for production altitudes ranging from 10 km to 60 km. All spectrograms are results from an initial beamed distribution. Left column is for a discrete altitude and right column is for a distributed altitude. Shown are the spectra escaping (a, d) at zenith angles between 20° and 29°, (b, e) at 40°–49° zenith angles, and (c, f) at 60°–69° zenith angles. The intensities are normalized to peak intensities.

isotropy angle the Compton scattered photons will dominate and give rise to a high-energy cutoff. Time profiles for both 0°–9° and 10°–19° (not shown) are similar to the profiles in Figure 4, first column, that is, as for photons escaping vertically out of the atmosphere. However, as soon as we sample at angles larger than the isotropic boundary a clear time delay is seen for TGFs produced $\leq$20 km. The explanation is again that we sample only photons that have experienced Compton scattering and energy degradation or reproduced by pair production. For TGFs produced at 30 km and above there are no time delay for the peaks but a tail can be seen.

3.4. Beamed Distributions From MC: Spectrograms

[24] To further see the spectral differences versus altitude and escaping angles, we present spectrograms (Figure 6) for three different escaping angles for discrete altitude (left column) and distributed altitude (right column). The initial X-ray distribution was beamed and E^{-1}. We want to point out the following: (1) The low-energy cutoff moves to lower energies as the TGFs are produced at higher altitudes. (2) The high-energy fall-off has a minimum for 10 km and 60 km with a maximum for 20 km. (3) The peak intensity (white line) are similar for 10 km to 30 km, but falls off for production altitudes above 30 km. (4) Production altitude of

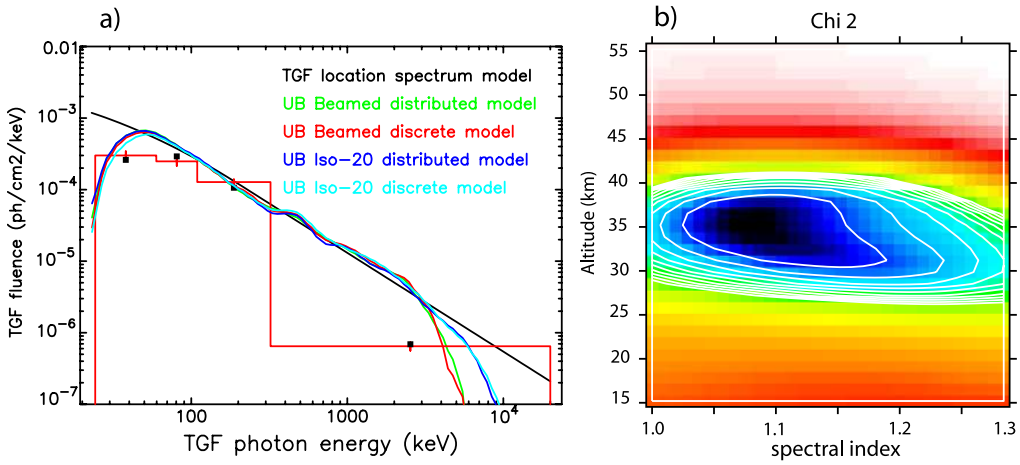

Figure 7. TGF trigger 106, showing (a) the first TGF location spectrum (TLS) used for the optimization (black) and the resulting best fit for the four libraries (red, green, blue, and cyan). The red histogram shows the best fit from the "beamed-discrete" library folded through the ERM with Poisson error bars (red vertical lines). Black squares are the mean input count values for the four BATSE detectors facing the TGF. Also shown is (b) χ^2 map giving the most likely production altitude for the "beamed-discrete" library.

15 km and 30 km gives very similar spectra which will be difficult to distinguish. (5) The similarities between a discrete altitude and a distributed altitude profile is striking except for TGFs produced at 10 km. To summarize so far, it should be possible to use the differences in low-energy and high-energy cutoffs as well as the peak energy to determine at what altitude the TGFs are produced.

4. Comparing With the BATSE Spectra and Time Profiles

[25] Now we describe how the library of all our modeled TGF spectra will be used to find the most likely production altitude and initial spectral index for each BATSE spectrum. The four different libraries of modeled spectra (the beamed-discrete, the beamed-distributed, the isotropic-cone-discrete, and the isotropic-cone-distributed) are used separately for each TGF. The production altitude and initial spectral index values are estimated by an optimization procedure which folds the modeled photon spectra through the BATSE Energy Response Matrix (ERM) to form a χ^2 parameter from actual BATSE data counts. The parameters of TGF amplitude, altitude, index, and spatial location are then varied in a continuum parameter space to find a minimum χ^2 value.

[26] For each BATSE TGF the procedure is carried out in three steps and the result for TGF trigger 106 is shown in Figure 7.

[27] 1. An initial coarse location map is created by scanning an image field of view below BATSE from the nadir out to the earth horizon (~70°). For each pixel a simple detector area vector (dot product) with the pixel direction vector is used to get a rough spectral amplitude and χ^2 parameter. This is done with just the four of the eight BATSE detectors which will be facing the pixel TGF flux direction. The result is a map of regions of detector "quadruples" showing how the χ^2 fitting parameter varies within them. This gives a sequence of coarse possible TGF locations which are then to be used as initial locations for a second finer search using some plausible spectral model.

[28] 2. For each possible location a first TGF Location Spectrum (TLS) is used and folded through the BATSE ERM to form a χ^2 optimization parameter with the BATSE count data (the black line in the Figure 7a). The TGF location and TLS parameters are varied to find a new location which is accurate to within about 5 degrees and close to the best TGF location estimate to be expected. The detector "quadruple" with the minimal χ^2 then gives the selection TGF location.

[29] 3. Using this finer location the procedure is then repeated to match with the MC modeled photon flux data and its altitude, spectral index, escape angle parameters to find a new optimal location and parameters. The resulting best fit for all four libraries are shown in Figure 7a as red, green, blue, and cyan lines. The beamed-discrete best fit is also shown as a red histogram after folded through the ERM with the Poisson uncertainties (red vertical lines). Black squares are the mean input count values for the four BATSE detectors facing the TGF.

[30] The results of the optimization for TGF trigger 106 can be seen in the altitude-index map (Figure 7b) showing the variation in the χ^2 fitting parameter around some optimum (altitude, index) point. From the first contour at χ^2 minimum +1.0, robust estimates in altitude and index can be obtained. Ideally, this contour should be a circle or ellipse but in some cases it is a long winding valley given a good estimate in altitude but a large error bar on the spectral index, perhaps so large that in some cases, the spectral index is not determinate.

[31] There are two criteria for including the TGFs in the final analysis. (1) The reduced χ^2 (i.e., the χ^2 divided by the degree of freedom) should be less than 1.5. (2) There is only one location, that is, zenith angle, that fulfills this criterion. Of the 25 BATSE TGFs we started with, a total 21 TGFs meet both these criteria. In Figure 8 the results of the optimization procedure described above for the four librar-

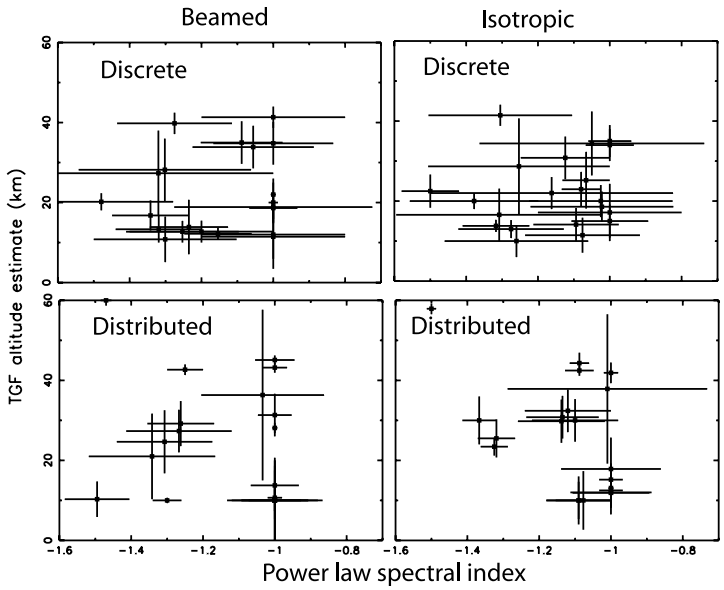

Figure 8. Optimized production altitude and initial power index of the 21 BATSE TGFs for the four libraries.

ies are shown with error bars for both altitude determination and initial spectral index.

5. Discussion

5.1. Production Altitude

[32] For all the four libraries the optimized production altitudes are found between 10 km to 40 km and in Figure 9 the distributions of altitudes are presented. Half or more of TGFs are produced at 20 km or below, and all libraries indicate that a significant portion of TGFs are produced at higher altitudes.

[33] The features that most significantly identify the altitude is the low-energy cutoff, the high-energy cutoff, and the bump in the spectrum around 1 MeV. All these features are highly dependent on what zenith angle the TGF

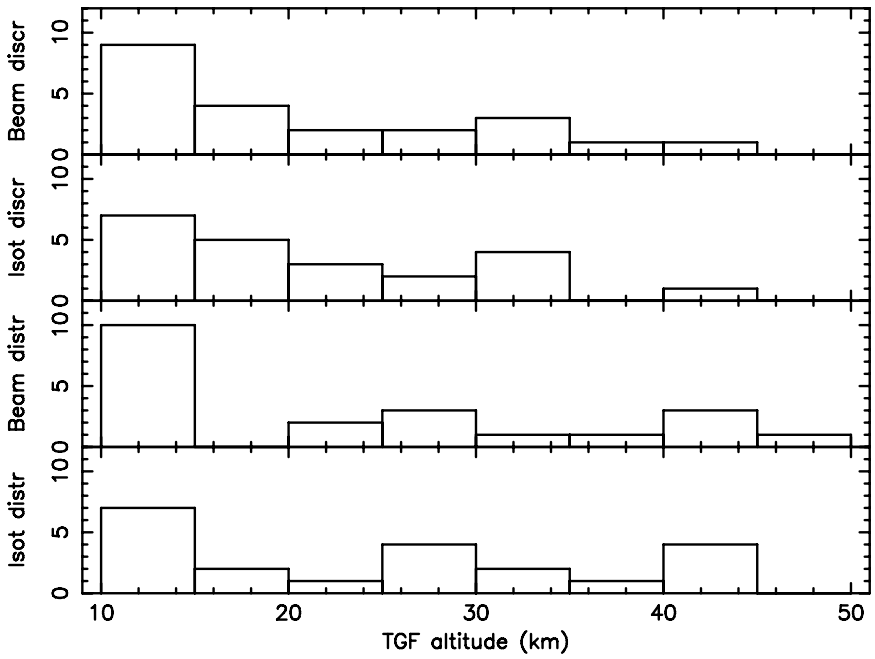

Figure 9. Histogram of production altitudes for all TGFs using the four libraries.

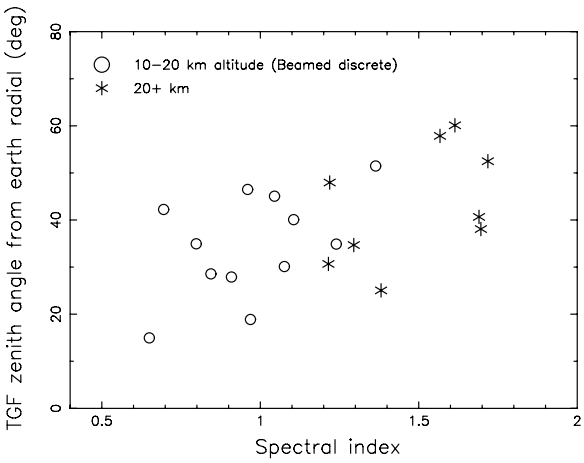

Figure 10. Zenith angles as a function of power spectral index for BATSE spectra. Using the results for the beamed-discrete library, the circles are TGFs produced at 10–20 km, and asterisks are TGFs produced above 20 km.

comes from, emphasizing how important this information is. Although the energy bins of the BATSE spectra are large we are able to distinguish the differences for low-energy and high-energy cutoff. The low-altitude TGFs are consistent with the results reported by *Dwyer and Smith* [2005] and *Carlson et al.* [2007] as well as observations of sferics correlated in time with TGFs [*Stanley et al.*, 2006]. *Cummer et al.* [2005] also suggested a low-altitude source due to insufficient charge moment changes to produce large electric fields at high altitudes for all the TGF they analyzed. On the other hand our results clearly indicate that a large portion of TGFs are produced at higher altitudes. The distributions in Figure 9 may indicate that there is a peak below 20 km and another from 30 km to 40 km. This would give some support to the modeling results by *Roussel-Dupré and Gurevich* [1996] showing that the electric field above thundercloud after an intracloud discharge can exceed the threshold electric field for runaway process at two altitudes, one just above the thundercloud and the other above 40 km.

5.2. Dispersion Signatures

[34] As shown in Figures 4a and 4b, second and fifth columns, the modeled X-ray distributions found from our library will give dispersion signatures of about 100μs for all TGFs produced $\leq$20 km (and even at 30 km for some escaping angles), in good agreement with the BATSE time delay distribution shown in Figure 2. In these cases the time delays can be explained as a pure Compton effect as explained earlier. No additional temporal behavior of the QES (or EMP) is then needed to explain this feature.

[35] For the two TGFs shown in Figure 1, when using the beamed-discrete library, we found that the trigger 2144 was most likely produced at 35 km while trigger 2465 was produced at 29 km, which is much closer in altitude than we would expect. Although our modeling result shows clear dispersion for TGFs produced $\leq$20 km, some escaping angles (i.e, at 30°–39°) also show dispersion from 30 km (not shown) and the dispersion signatures seen for both these TGFs can still be a Compton effect.

5.3. Beamed or Isotropic Initial X-Ray Distribution

[36] In section 3 we pointed out that there is a very clear high-energy cutoff that moves to lower energies as the TGFs are observed at larger zenith angles. However, this will only be seen when the zenith angle (of observation) is larger than the angle defining the initial isotropic X-ray distribution (for a plane atmosphere). Furthermore, we made the point that this distinct high-energy cutoff should be observed if one had the energy resolution. As BATSE does not have sufficient spectral resolution at high energies we will look for a softening of the spectrum.

[37] In Figure 10 the zenith angle is shown as function of power index. This power index is not the power index that defines the initial X-ray distribution of the TGF as it is produced in the atmosphere. The power index shown here is related to the TGF spectrum escaping the atmosphere and give a measure of softening due to the high-energy cutoff. There is a clear trend that the TGF spectra observed by BATSE is softer at larger zenith angle. Following our argument about high-energy cutoff for TGFs observed at zenith angles larger than the isotropy angle, this is an indication that the initial distribution of X-ray is fairly beamed. Using the altitudes estimates from the beamed-discrete library, we can also see that TGFs produced deep in the atmosphere (open circles) have a harder spectrum than the TGFs produced at higher altitudes (asterisk) in excellent agreement with the bump at 1 MeV or flattening seen in the modeled spectra in Figures 4a and 4b, third column.

[38] A second indicator of beamed distribution is the time dispersion that will not be seen if the angle of observation is within the isotropic cone angle. As dispersion signature is a common feature this indicates that the isotropic cone angle has to be small, probably $\leq$30°.

[39] To summarize, both the softening for increasing zenith (escaping) angles and the commonly observed time dispersion indicate that the initial X rays are fairly beamed as suggested by *Cummer et al.* [2005] and *Stanley et al.* [2006] and not isotropic within a half-angle of 45° [*Carlson et al.*, 2007].

[40] Finally, we want to emphasize once again that there are no electric field in our model. This means that the pair-produced positrons and electrons are not accelerated, which may underestimate the refilling of low-energy X rays somewhat. Future modeling efforts will aim at resolving this.

6. Conclusions

[41] By modeling the X-ray propagation through the atmosphere, taking into account all the important interaction processes the X-ray photons experience, we have built four libraries of the expected X-ray distributions at the top of the atmosphere for different escaping angles.

[42] Important features seen in the modeled spectra can be summarized:

[43] 1. A low-energy cutoff which moves to lower energies as TGFs are produced at higher altitudes.

[44] 2. A high-energy cutoff which moves to lower energies as TGFs are observed at larger zenith angles.

[45] 3. Time delays are observed for TGFs produced at $\leq$20 km (and some at 30 km) altitude when observed at larger zenith angle than the half-angle defining the initial isotropic X-ray beam. This is a pure Compton effect.

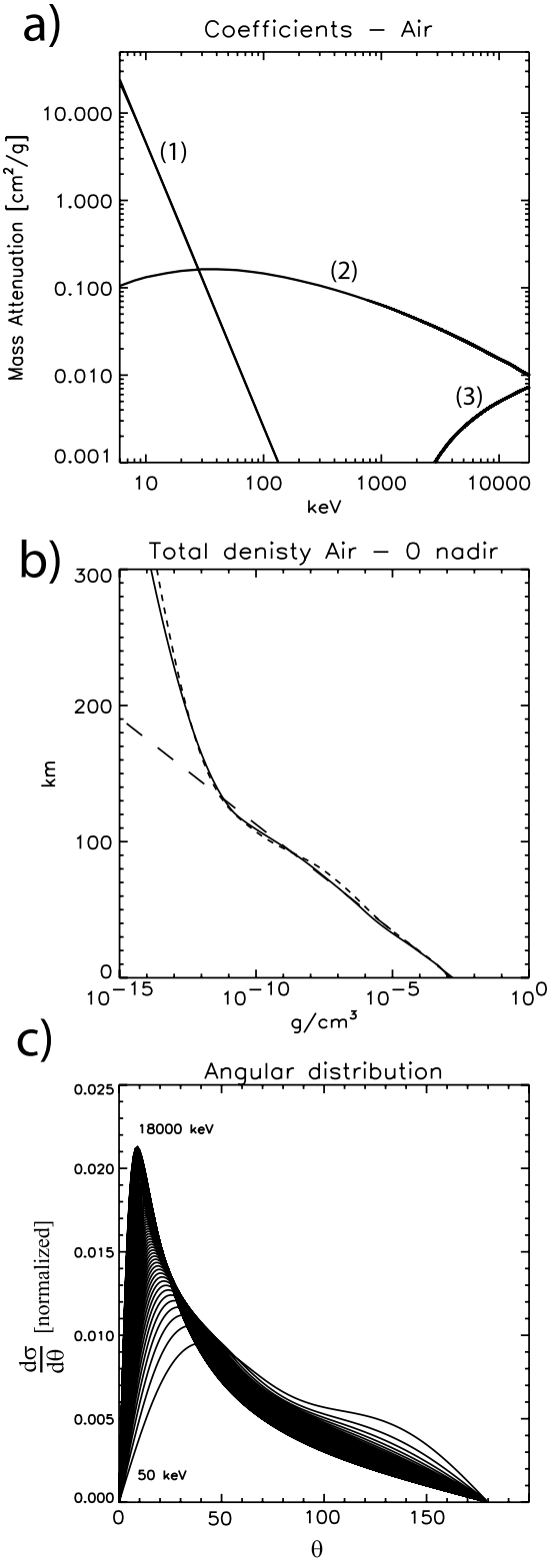

Figure A1. (a) Coefficient for photoelectric absorption (1), Compton (2), and pair production (3) in Air, (b) MSIS-E-90 density profiles at 55° latitude for July (dotted) and January (solid) overlaid an exponential fit (dashed), and (c) the angular probability for Compton scattering for energies from 50 keV to 18 MeV. Each profile is normalized to the total for that specific energy.

[46] Combined with an optimization procedure to determine the zenith angle from BATSE measurements and the most likely production altitude and initial power index of the TGF, we have reached the following conclusions: (1) Half or more of the BATSE TGFs are produced at low altitudes, $\leq$20 km. (2) A significant portion of the BATSE TGFs are produced at higher altitudes, 30 km to 40 km. (3) For the TGFs produced at $\leq$20 km (and some at 30 km) the dispersion signatures can be explained as a pure Compton effect. (4) The softening of the observed BATSE spectra for increasing zenith angles indicate that the initial TGF photon distribution produced at some altitude is highly beamed.

[47] As all four libraries give converging results, we believe that it is not crucial for these results whether we assume discrete or distributed altitude as long as the peak altitude is dominating. Furthermore, as long as the half-angle of initial isotropic X-ray distribution is kept smaller than the zenith angle of observation, the beamed and isotropic (within 20°) distribution give very similar results.

Appendix A: Monte Carlo Code

A1. Basic Elements of the MC Code

[48] As input to the MC code we need the coefficients in air for absorption (μ_A), Compton scattering (μ_C) and pair production (μ_P). We have used the coefficients given by *Storm and Israel* [1967] for different photon energies as shown in Figure A1a.

[49] In Figure A1b the MSIS-E-90 atmospheric density profile at 55° geographic latitude is shown for July (dotted) and January (solid). The dashed line is the exponential fit to the January profile, requiring that the column density below 100 km is identical for the MSIS January profile and the exponential fit. The exponential fit helps us solving the path length analytically (see below) on the expense of not getting the small increase in density between 50 km and 80 km. The column densities for the various discrete production altitudes used in this study is given in Table A1.

[50] As Compton scattering implies both scattering and energy decrease depending on scattering angle, we need information about the angular scattering probability. Noticing that incoherent scattering is only important at low X-ray energies where absorption is dominating anyway, the following expression for Compton scattering probability versus scattering angle [*Storm and Israel*, 1967] can be used

$$\frac{d\sigma}{d\theta} = \pi r_0^2 Z \sin\theta \frac{1}{[1+\alpha_n(1-\cos\theta)]^2} \times \left[1+\cos^2\theta + \frac{\alpha_n^2(1-\cos\theta)^2}{1+\alpha_n(1-\cos\theta)}\right] \quad \text{(A1)}$$

where r_0 is the electron radius, Z is average atomic number for air (7.35) and $\alpha_n = \frac{E}{511\text{keV}}$. E is the energy of the photon.

Table A1. Altitude and Atmospheric Column Density

Altitude, km	Column Density, g/cm^2
10	270
15	129
20	62
30	14
40	3.2
50	0.74
60	0.17

The normalized probability distributions for X-ray energies (E) from 50 keV to 18 MeV are shown in Figure A1c. For high energy X rays the Compton scattering are strongly forward scattered ($\theta = 0$ is forward). When the scattering angle is known the new energy of the X-ray photon is given by

$$E_{new} = \frac{1}{\left[\frac{1}{E} + \frac{1}{511\text{keV}}(1 - \cos\theta)\right]} \quad \text{(A2)}$$

We have not included bremsstrahlung from Compton accelerated electrons, see discussion below.

[51] Pair production is treated separately for positrons and electrons. We assume the positrons will lose their energy through multiple collisions and eventually annihilate with a cold electron and produce two photons with energy of 511 keV in arbitrary but opposite directions. Although many of these photons will be degraded in energy by Compton scattering the peak at 511 keV in the spectrum escaping the atmosphere is due to the contribution from X rays produced by positrons. We have not included bremsstrahlung production from the positrons, see discussion below. For pair-produced electrons we have included the bremsstrahlung production. The newly produced electrons will have energies given by

$$E_E = \frac{E_X - 2 \times 511\text{keV}}{2} \quad \text{(A3)}$$

These electrons will produce bremsstrahlung with energies ranging from 0 keV to E_E. A test run with GEANT starting with 1 million X-ray photons from a discrete altitude of 15 km beamed inside a cone of 1° zenith angle (similar setup as shown in Figure 3a) was made with and without this bremsstrahlung produced by all electrons (pair-produced and Compton accelerated) and pair-produced positrons. The result can be seen in Figure A2.

[52] At the top of the atmosphere the contribution over all escaping angles is about 7% distributed in energies below ~80 keV. For altitudes above 30 km the contribution is

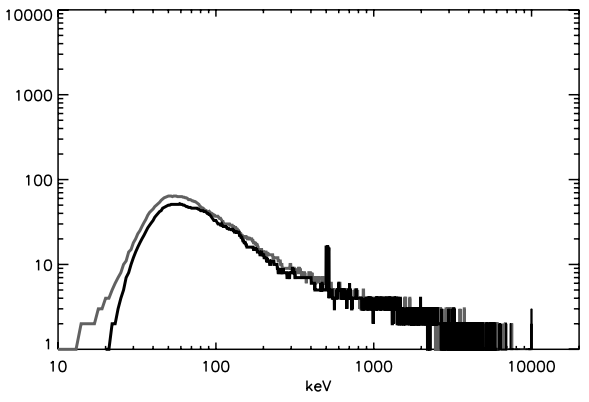

Figure A2. GEANT results from 15 km with (gray) and without (black) bremsstrahlung from electrons produced by the pair-production process.

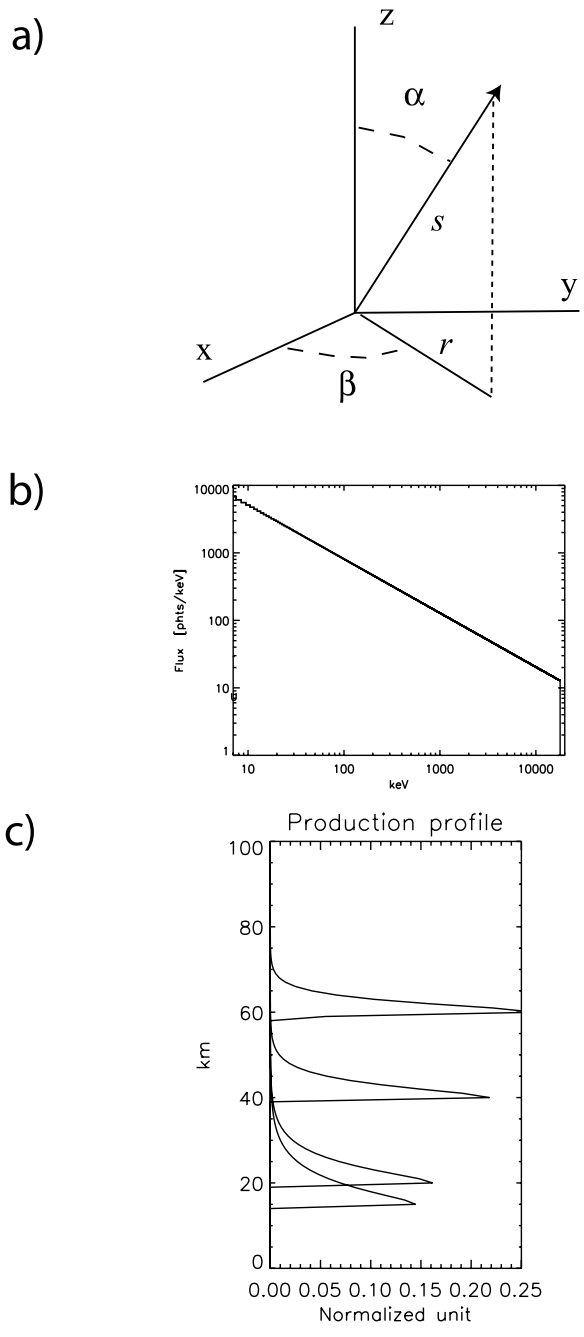

Figure A3. (a) Geometry for photon propagation, (b) the initial energy distribution of photons for $\lambda = 1.0$, and (c) the altitude profiles used for distributed production altitude starting at 15 km, 20 km, 40 km, and 60 km.

negligible. Although we do not think that this contribution will alter the results in this paper significantly, we have included the bremsstrahlung contribution from the pair-produced electrons in our MC code. The cross section for bremsstrahlung production for electrons is taken from *Evans* [1955] and the angular distribution is for simplicity assumed to be in the direction of the parent electron.

[53] Although we have not included all the bremsstrahlung processes correctly, the validation by comparing our model with GEANT, which is shown in Figure 3, convinces us that our simplistic approach to estimate the bremsstrahlung contribution is not crucial for the results presented in this paper.

[54] In our MC simulations we start out with 1 (or 5) million photons. Each photon holds information about (1) altitude, z, (2) energy, E, (3) polar angle relative to z-axis, α, (4) azimuthal angle, β, (5) distant from origo, r in the xy plane, and (6) accumulated path length, s. The geometry is shown in Figure A3a.

[55] For each photon we calculate the path length before an interaction takes place based on general MC approach using the total interaction probability and random numbers. Using the exponential fit to the atmospheric density, this path length can be solved analytically by the following equation

$$s\pm = \frac{-1}{a\cos\alpha}\ln\left[1 \pm \frac{\ln(1-rand)a\cos\alpha}{\mu_T \rho_{z1}}\right] \qquad \text{(A4)}$$

where upward is a plus symbol and downward is a minus symbol, the angle α is defined in Figure A3a. The random number is *rand* and μ_T is given by

$$\mu_T = \mu_A + \mu_C + \mu_P \qquad \text{(A5)}$$

The density, ρ_{z_1}, at the starting altitude, z_1 is given by equation (A6) where a is the coefficient in the exponential fit to the atmospheric density.

$$\rho_{z1} = \rho_0 e^{-az_1} \qquad \text{(A6)}$$

These analytic expressions are only valid for a planar atmosphere, which is used to speed up the code significantly. To find path lengths for a spherical atmosphere requires numerical integration. Our approach will underestimate the number of X-rays leaving the atmosphere and overestimate the accumulated path lengths slightly. As these effects are only significant for photons with α close to 90° we do not allow photons to have α angles between 85° and 95°. For angles <85° and >95° these effects are very small.

[56] The next step is to determine whether the interaction is absorption, Compton scattering or pair production by using their relative probabilities. For absorption the photon is lost. For Compton scattering, the angular probability function and energy formula (equation (A2)) gives us the new direction and energy. The new r and s are also calculated. For pair production the bremsstrahlung from electrons and the X rays produced from positron-electron annihilation are estimated. These X rays are added to the spectrum at this stage. This sequence is repeated until all photons have either reached the ground, escaped the atmosphere (>100 km), or been absorbed.

A2. Building the Library

[57] The 1 (or 5) million photons are initiated with a power law distribution, $E^{-\lambda}$ with a cutoff energy at 18 MeV (as shown in Figure A3b for $\lambda = 1$) at either a discrete altitude (z_1) or a distributed altitude (as shown for $z_1 = 15$ km and $z_1 = 30$ km). We also run the code for two different initial angular distributions.

[58] First, we initiate the photons as a beam along the z-axis, with $\alpha = 0$ for six different λs ranging from 1 to 1.5, starting at seven different altitudes, that is, 10, 15, 20, 30, 40, 50, and 60 km using two different profiles, a discrete altitude and a distributed profile. We sample each run at the top of the atmosphere in seven different 10°-intervals of escaping angles, that is, α = 0°–9°,10°–19°, 20°–29°, 30°–39°, 40°–49° 50°–59° and 60°–69°. For the beamed distribution from discrete altitude this gives $6 \times 7 \times 7 = 294$ different spectra escaping the atmosphere.

[59] The same procedure is repeated with beamed distribution and distributed production altitude profile, an initial isotropic distribution within $\alpha = 20$ from discrete altitude and an initial isotropic distribution within $\alpha = 20$ from distributed production altitude profile, giving four libraries of spectra ($294 \times 4 = 1176$).

[60] These four libraries, which are denoted "beamed-discrete," "beamed-distributed," "isotropic-cone-discrete," and "isotropic-cone-distributed," containing a total of 1176 spectra escaping the top of the atmosphere are then used for the fitting procedure for each measured BATSE spectrum.

[61] **Acknowledgments.** The authors would like to thank G. Fishman for the use of the BATSE data.

[62] Amitava Bhattacharjee thanks the reviewers for their assistance in evaluating this paper.

References

Agostinelli, X., et al. (2003), Geant4-A simulation toolkit, *Nucl. Instrum. Methods Phys. Res., Sect. A*, *506*, 250–303.

Carlson, B. E., N. G. Lehtinen, and U. S. Inan (2007), Constraints on terrestrial gamma ray flash production from satellite observation, *Geophys. Res. Lett.*, *34*, L08809, doi:10.1029/2006GL029229.

Cummer, S. A., Y. Zhai, W. Hu, D. M. Smith, L. I. Lopez, and M. A. Stanley (2005), Measurements and implications of the relationship between lightning and terrestrial gamma ray flashes, *Geophys. Res. Lett.*, *32*, L08811, doi:10.1029/2005GL022778.

Dwyer, J. R., and D. M. Smith (2005), A comparison between Monte Carlo simulations of runaway breakdown and terrestrial gamma-ray flash observations, *Geophys. Res. Lett.*, *32*, L22804, doi:10.1029/2005GL023848.

Evans, R. D. (1955), *The Atomic Nucleus*, McGraw-Hill, New York.

Fishman, G. J., et al. (1994), Discovery of intense gamma-ray flashes of atmospheric origin, *Science*, *164*, 1313.

Gurevich, A. V., and K. P. Zybin (2001), Runaway breakdown and electric discharges in thunderstorms, *Usp. Fiz. Nauk*, *44*, 1119–1140.

Inan, U. S., and N. G. Lehtinen (2005), Production of terrestrial gamma-ray flashes by an electromagnetic pulse from a lightning return stroke, *Geophys. Res. Lett.*, *32*, L19818, doi:10.1029/2005GL023702.

Lehtinen, N. G., T. F. Bell, V. P. Pasko, and U. S. Inan (1997), A two-dimensional model of runaway electron beams driven by quasi-electrostatic thundercloud fields, *Geophys. Res. Lett.*, *24*, 2639–2642.

Lehtinen, N. G., T. F. Belkl, and U. S. Inan (1999), Monte Carlo simulation of runaway MeV electron breakdown with application to red sprites and terrestrial gamma flashes, *J. Geophys. Res.*, *104*, 24,699–24,712.

Lehtinen, N. G., T. F. Belkl, and U. S. Inan (2001), Effects of thunderstorm-driven runaway electrons in the conjugate hemisphere: Purple sprites, ionization enhancements, and gamma rays, *J. Geophys. Res.*, *106*, 28,841–28,856.

Nemiroff, R. J., J. T. Bonnell, and J. P. Norris (1997), Temporal and spectral characteristics of terrestrial gamma flashes, *J. Geophys. Res.*, *102*, 9659–9665.

Roussel-Dupré, R., and A. V. Gurevich (1996), On runaway breakdown and upward propageting discharges, *J. Geophys. Res.*, *101*, 2297–2311.

Smith, D. M., L. L. Lopez, R. P. Lin, and C. P. Barrington-Leigh (2005), Terrestrial gamma-ray flashes observed up to 20 MeV, *Science*, *307*, 1085–1088.

Stanley, M. A., X. M. Shao, D. M. Smith, L. I. Lopez, M. B. Pongratz, J. D. Harlin, M. Stock, and A. Regan (2006), A link between terrestrial gamma-ray flashes and intracloud lightning discharges, *Geophys. Res. Lett.*, *33*, L06803, doi:10.1029/2005GL025537.

Storm, E., and H. I. Israel (1967), Photon cross section from 0.001 to 100 MeV for elements 1 through 100, *Tech. Rep. LA-3753*, Los Alamos Sci. Lab., Los Alamos, N. M.

B. Carlson, Electric Engineering, STAR Laboratory, Stanford University, Stanford, CA 94305, USA.

P. H. Connell, Institute of Mechanical Science, University of Valencia, P.O. Box 22085, Valencia E-46071, Spain.

T. Gjesteland, N. Østgaard, and J. Stadsnes, Department of Physics and Technology, University of Bergen, Allegt. 55, N-5007, Bergen, Norway. (nikolai.ostgaard@ift.uib.no)

6.2 Paper II

Effects of dead time losses on terrestrial gamma ray flash measurements with the Burst and Transient Source Experiment
T. Gjesteland , N. Østgaard, P. H. Connell, J. Stadsnes, and G. J. Fishman

J. Geophys. Res., 115, A00E21, doi:10.1029/2009JA014578, 2010

JOURNAL OF GEOPHYSICAL RESEARCH, VOL. 115, A00E21, doi:10.1029/2009JA014578, 2010

Effects of dead time losses on terrestrial gamma ray flash measurements with the Burst and Transient Source Experiment

T. Gjesteland,[1] N. Østgaard,[1] P. H. Connell,[2] J. Stadsnes,[1] and G. J. Fishman[3]

Received 18 June 2009; revised 17 November 2009; accepted 1 December 2009; published 5 May 2010.

[1] Measurements from the Burst and Transient Source Experiment (BATSE) instrument on the Compton Gamma Ray Observatory (CGRO) are the only ones where characteristics of single terrestrial gamma ray flashes (TGFs) have been obtained thus far. However, it has been reported that the measurements suffer from significant dead time losses which complicates the analysis and raises question about earlier BATSE studies. These losses are due to the high-intensity flux combined with limitations of the time resolution of the instrument. Since these losses will affect both the spectrum and the temporal distribution of the individual TGFs, results based on BATSE data need to be revisited, including our own. We have therefore developed a Monte Carlo method to study the effects of these dead time losses. We show that the energy spectrum of TGFs becomes softer as the dead time losses increase. We also show that the time delay between the light curves of hard ($E > 300$ keV) and soft ($E < 300$ keV) photons increases significantly as the dead time losses increase. The Monte Carlo approach also enables us to identify the BATSE TGFs where the dead time effects can be corrected. These are the short-duration single-peaked TGFs. Without correcting for dead time losses we find that these short single-peak TGFs have a softer energy spectrum and larger time delay than the multipeaked TGFs. After correcting for dead time losses we perform a new analysis of production altitudes and find that the production altitude is reduced compared to analysis without dead time losses. The new production altitudes combined with dead time losses are also consistent with the apparent large time delays. Our method gives consistent results regarding production altitude and time delays and indicates that the corrected TGF intensities measured by BATSE are 3 to 4 times brighter than the uncorrected measurements would indicate. We also show that the production mechanism of these TGFs has a typical duration of 250 μs.

Citation: Gjesteland, T., N. Østgaard, P. H. Connell, J. Stadsnes, and G. J. Fishman (2010), Effects of dead time losses on terrestrial gamma ray flash measurements with the Burst and Transient Source Experiment, *J. Geophys. Res.*, *115*, A00E21, doi:10.1029/2009JA014578.

1. Introduction

[2] Terrestrial gamma ray flashes (TGFs) were discovered by the Burst and Transient Source Experiment (BATSE) on board the Compton Gamma Ray Observatory (CGRO) [*Fishman et al.*, 1994]. They were found to be short (~1 ms) gamma bursts related to thunderstorms. Triangulation of ELF/VLF radio atmospherics (sferics) from lightning have shown that TGF are indeed related to lightning [*Inan et al.*, 1996; *Cummer et al.*, 2005; *Inan et al.*, 2006; *Cohen et al.*, 2006; *Stanley et al.*, 2006]. New observations of TGFs have been provided by the Reuven Ramaty High Energy Solar Spectroscopic Imager (RHESSI) [*Smith et al.*, 2005], showing gamma photons which energy were up to 20 MeV.

[3] While the production mechanism of TGF is still not determined, they are assumed to be bremsstrahlung from a relativistic runaway electric avalanche (RREA) [*Roussel-Dupre et al.*, 1994; *Gurevich and Zybin*, 2001]. TGF was first assumed to be associated with red sprites at 30–80 km altitude [*Nemiroff et al.*, 1997]. Thus, a quasi-electrostatic (QES) field [*Lehtinen et al.*, 1996] and electromagnetic pulses (EMPs) [*Inan and Lehtinen*, 2005] were suggested to explain how a relativistic runaway breakdown process could occur at these altitudes. However, other studies have suggested that leaders and streamers could be a source of runaway electrons [*Moss et al.*, 2006; *Chanrion and Nubert*, 2008] indicating a much lower production altitude. Recently, simulations by *Carlson et al.* [2009] found that RREA in lightning leaders can produce TGFs, implying a production altitude within thunder clouds.

[4] Because of the attenuation of X-rays and gamma rays propagating through the atmosphere, spectral measurements from BATSE and RHESSI are used to determine the production altitude of TGFs. *Dwyer and Smith* [2005] used a

[1]Department of Physics and Technology, University of Bergen, Bergen, Norway.
[2]Institute of Mechanical Science, University of Valencia, Valencia, Spain.
[3]NASA Marshall Space Flight Center, Huntsville, Alabama, USA.

0148-0227/10/2009JA014578

superposition of all the RHESSI TGFs to show that a simulated TGF produced at 15–21 km altitude could best reproduce the RHESSI spectrum. This average value of production altitude based on superposed RHESSI spectrum was also reported by *Carlson et al.* [2007]. *Carlson et al.* [2007] also found the BATSE measurements fit a production altitude of 15 km. A production altitude of ~15 km is consistent with tropical thunderstorm [*Williams et al.*, 2006]. *Østgaard et al.* [2008] used a different approach in the analysis of the BATSE TGFs. Instead of using a superposition of all events, *Østgaard et al.* [2008] analyzed each individual TGF and concluded that a majority were produced at low altitude (10 to 20 km) while a significant portion was produced at higher altitude, i.e., 30 to 40 km.

[5] Since then it has been shown that the BATSE instrument suffers from a significant dead time problem [*Grefenstette et al.*, 2008], i.e., that the read-out electronics of the BATSE instruments are not fast enough to count all the scintillation pulses from the detector material (NaI). In most cases this is an effect that can be corrected for, unless the system is paralyzed. On the basis of preflight data, *Grefenstette et al.* [2008] showed that BATSE was indeed a paralyzable detector. As the time delays observed by BATSE were systematically longer than what can be explained by Compton scattering, they claimed that the dead time losses in the detector could account for this extra time delay. They also showed that BATSE TGFs, which suffer from significant dead time losses, show a softer energy spectrum than the true spectrum.

[6] An analysis of the temporal behavior of TGFs by *Feng et al.* [2002] found the low-energy photons (25 keV < E < 110 keV) to have a ~100 μs delay compared to the high-energy photons (E > 110 keV). *Østgaard et al.* [2008] found that observed time delays can be explained qualitatively by Compton scattering effects of the X-rays as they propagate through the atmosphere. However, when we looked in more detail we found that the Compton scattering effect alone could not account for the entire time delay, which supports the hypothesis of dead time losses being responsible for the large time delays [*Grefenstette et al.*, 2008].

[7] Furthermore, as long as the effect of dead time losses has not been addressed it can be argued that all temporal and spectral results based on BATSE measurements without taking dead time effects into account are questionable.

[8] Because of the long trigger window (64 ms), a short event such as a TGF (which typically lasts 1 ms) needs to be very intense to cause a trigger. Several of the BATSE TGFs contain several peaks, each lasting approx 1 ms. On the basis of the same argument, we would assume that single-peaked TGFs suffer from more dead time losses than the multipeaked TGFs. In the work of *Østgaard et al.* [2008], a significant portion of the TGFs were found to be produced at 30 to 40 km altitude, most of them being short-duration single-peaked TGFs.

[9] In this study we present a Monte Carlo simulation of the BATSE detector and read-out electronics. We follow each photon from its entrance into the detector material using the Detector Response Matrix (DRM) to produce an electric pulse. Then we carefully model the read-out electronics with its characteristic decay time and reset level to obtain the measured count rates. We will show how we can determine whether the detector is paralyzed or not and why the dead time effects can be corrected for in detected single-peaked TGFs. This approach enables us to obtain new estimates of production altitude which is consistent with the measured time delays. The paper is organized as follows: First, a section describing the method applied to one TGF (section 2), then a section presenting the results for five single TGFs (section 3), followed by discussion and summary sections (sections 4 and 5).

2. Method

[10] To analyze the BATSE measurements, we have developed a Monte Carlo simulation where the input is the photon distribution in time and energy (spectrum). The Detector Response Matrix (DRM) gives the conversion of photons to electronic pulses. The readout electronics are then modeled with its characteristic decay time and reset level which define the dead time for different incoming flux levels. This enables us to estimate the measured count rates of the detector. Our tools in this analysis are (1) a Monte Carlo input-spectrum, with assumptions about initial spectral and spatial distribution for various production altitudes; (2) the Detector Response Matrix; and (3) Monte Carlo simulation of the dead time losses. The Monte Carlo simulation of photons propagating trough the atmosphere is the same as that described by *Østgaard et al.* [2008] with the following initial assumptions:

[11] 1. A photon energy spectrum on the form

$$F(E) = E^{-\gamma} \exp \frac{-E}{10\ \mathrm{MeV}}. \quad (1)$$

[12] 2. A beamed (half-angle 1°) or isotropic cone (half-angle 50°) distribution.

[13] 3. Discrete production altitude ranging from 10 km to 30 km.

[14] In the work of *Østgaard et al.* [2008], the energy spectrum was on the form $F(E) = E^{-\gamma}$, and the isotropic cone half-angle was 20°. The energy spectrum is modified with an exponential term (1) to avoid a sharp cut off at high energies, which is closer to the expected bremsstrahlung spectrum from the runaway electrons [*Dwyer and Smith*, 2005]. The broadness of the cone is here set to 50°, which is wider than given by *Østgaard et al.* [2008] where the half-angle was 20°. The rational for using a wider cone angle is that BATSE will then be inside that cone for all the TGFs we analyze in this paper. The wider beam is also similar to results from *Dwyer and Smith* [2005] and *Carlson et al.* [2007], who found that a wider beam (half-angle 45°) fits the RHESSI data for a 15 km source altitude.

[15] To analyze the production altitude and the TGF's temporal behavior, we present this method in seven steps using TGF 2955 as an example. The initial assumptions for our simulated TGF are a beamed distribution produced at 20 km altitude and an initial energy spectrum on the form of equation (1), where γ = 1.0, which is what one expects for a bremsstrahlung spectrum.

[16] Step 1: Determine the duration of the TGF production process. Since the dead time losses depend on both the total number of photons, their energy, and how they are distributed in time, the temporal properties of the TGF production

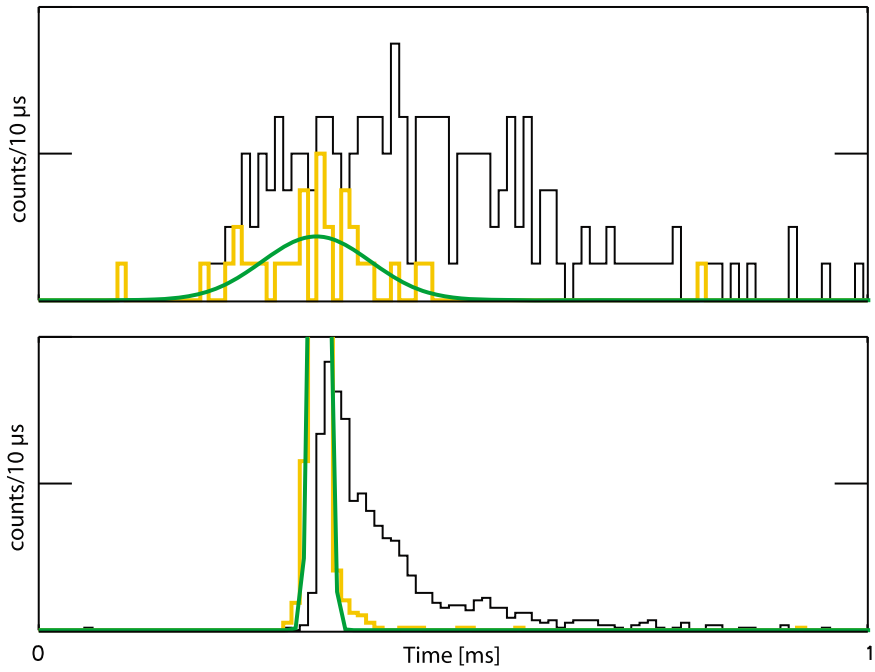

Figure 1. (top) Light curve of BATSE TGF 2955. (bottom) Light curve from MC simulation. The light curve of all photons is black, and the light curve of the hard photons (E > 300 keV) is orange.

mechanism must be included in the simulations. From our simulations of X-ray propagation through the atmosphere we know that most of the low-energy photons that escape the atmosphere are originally high-energy photons that are Compton scattered in the atmosphere and reduced in energy [*Østgaard et al.*, 2008]. This scattering process makes their travel path longer which again results in a dispersion. On the other hand, the high-energy photons that escape the atmosphere are hardly scattered and therefore travel almost directly from their origin up to satellite altitudes. Assuming no dispersion in the emitting process, we can assume that the temporal distribution of hard photons (E > 300 keV) measured by BATSE reflects the temporal distribution of the production mechanism with only a small dispersion effect. However, from our Monte Carlo model of X-rays through the atmosphere we can find the dispersion due to Compton scattering for photons E > 300 keV, which can be subtracted from the duration of the measured E > 300 keV photons. In Figure 1 (top) the light curve of TGF 2955 is black, and the light curve of hard photons (channel 4, E > 300 keV) is orange, with a green Gauss-fitted curve. Figure 1 (bottom) shows the total and the hard light curve from our simulations. All the photons start at the same time at the TGF's production altitude in our simulation. The duration of the hard light curves is determined as $\pm 2\sigma$ of the Gaussian-fitted curves. While the duration of high-energy photons in our simulation only lasts 10 μs, the hard light curve of BATSE TGF 2955 lasts 260 μs. For the duration of the TGF production mechanism we therefore use Gaussian temporal behavior which is 250 μs within $\pm 2\sigma$. As mentioned above, we use a photon distribution escaping the atmosphere from a production altitude of 20 km. For each of these photons a Gaussian-distributed random Δt between 0 and 250 μs is added to the time delays we already have from Compton scattering to have the most realistic distribution of photons in both energy and time.

[17] Step 2: Determine the zenith angle or angle of entrance to the detector. The relative total counts in the four Large Area Detectors (LADs) that have most counts are used to estimate the zenith angle. Of the escaping photons in our simulation we use the photons that would hit BATSE at the calculated zenith angle ±5°

[18] Step 3: Convert from photons to pulses in the detector material. The zenith angle and the DRM will give us the effective detecting area for each of the LADs. DRM give us then to covert the incoming photons to pulses in the four BATSE discriminator levels. For various numbers of incoming photons we use the DRM to determine whether or not the photon will interact with the LAD, which discriminator will respond to and produce a pulse. The four discriminators have the following energy ranges: 25 to 60 keV, 60 to 110 keV, 110 to 320 keV, and >320 keV.

[19] Step 4: Convert from pulse to count. If the pulses in the detector are coming faster than the electronics can register them, the detector will suffer from dead time losses. *Grefenstette et al.* [2008] showed that BATSE has a dead time given by

$$\tau \sim \alpha \ln \frac{E_p}{E_0}, \tag{2}$$

where α is the signal decay time, E_p is the energy of the photon, and E_0 is the reset level of the detector. A photon hitting a LAD will produce a pulse, V_p, that rises in a very

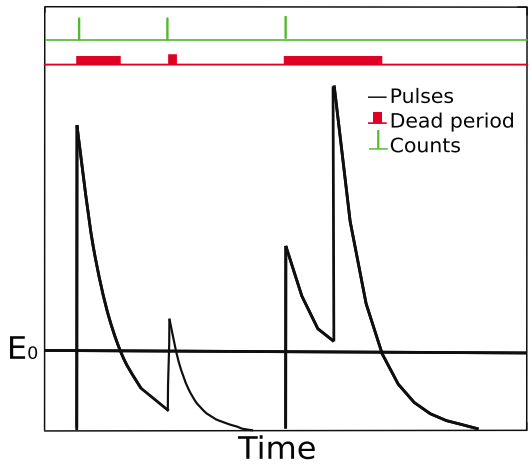

Figure 2. Sketch of dead time loss.

short time scale ($\ll 1$ μs) with amplitude proportional to the energy deposited by the photon (E_p). The pulse will then decay exponentially ($V(t) = V_p e^{-t/\alpha}$ corresponding to $E(t) = E_p e^{-t/\alpha}$) with a signal decay time α, while the electronics reads out the pulse. The LAD cannot register a new photon until the previous pulse is reduced to the reset level, expressed as energy, E_0. On the other hand, if a photon hits the detector before the previous signal is reduced to its reset level, the new photon is not registered. This effect results in dead time losses. Figure 2 shows a sketch of how the pulses and counts occur in a detector. The bold red area marks the time when the detector is dead. Green ticks show when a pulse is registered as a count. The last pulse occurs before the reset level is reached and is therefore not counted.

[20] On the basis of preflight data, *Grefenstette et al.* [2008] determined α = 0.75 μs and E_0 = 5.5 keV. No error bars were given; 0.75 μs is three times the fluorescence decay time of NaI scintillator, which is the scintillator used in the BATSE LADs. It can be argued that the decay time should be shorter, and in that case the dead time effects will be slightly less. However, we here assume the decay time from *Grefenstette et al.* [2008]. A discussion of how a change in the decay time influences the results is given in section 3.

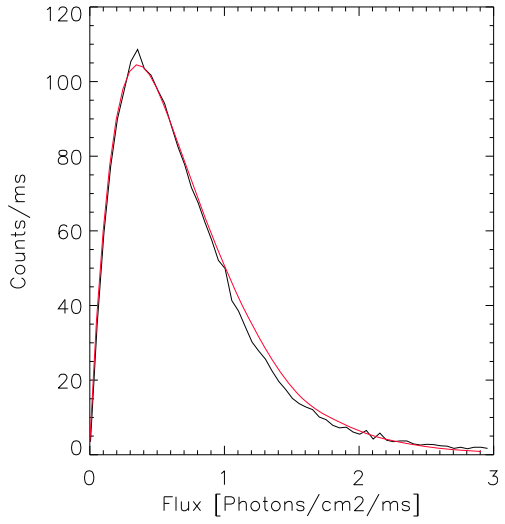

Figure 3. The paralyzation curve for equation (3) (red) and MC (black).

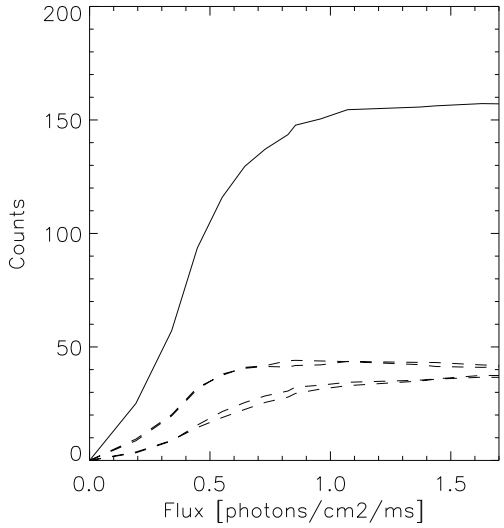

Figure 4. The solid curve is the sum of the paralyzation curves for the four brightest LADs, each of which is shown as a dashed curve.

[21] A paralyzable detector with dead time, which does not vary on the photons' energy, suffers from dead time losses on the form

$$m = ne^{-n\tau} \tag{3}$$

where m is the measured count rate, n is the incoming pulse rate, and τ is the instrument's dead time [*Knoll*, 1989]. In our simulation we use equation (2), with α = 0.75 μs and E_0 = 5.5 keV to calculate τ for each pulse or sequence of pulses (see Figure 2). With the input distribution of photons in energy and time we can vary the total number of incoming photons, i.e., the photon flux, and calculate the number of pulses by the DRM and then simulate what will be measured by BATSE. Figure 3 shows the paralyzation curve of equation (3) with a dead time of 3.3 μs in red and the result of our MC dead time simulation when the pulse rate increases. The x axis is the photon flux, and the y axis is the counts per ms. The input in the MC simulation a given number of 500 keV photons uniformly distributed in time (within 1 ms). This sample plot illustrates that for a given number of detected counts, e.g., 60, there are two possible incoming photon flux values, 0.1 and 0.9 photons/cm^2/ms. However, all the short-duration single-peaked TGFs in this study are on the left side of the maximum. Figure 4 shows the paralyzation curve for TGF 2955, where the spectral and temporal distributions from our simulation are included. The solid curve is combined of the four LADs facing the TGF. The dashed curves represent each of the four LADs. Two of the LADs have a larger effective area and therefore reach the

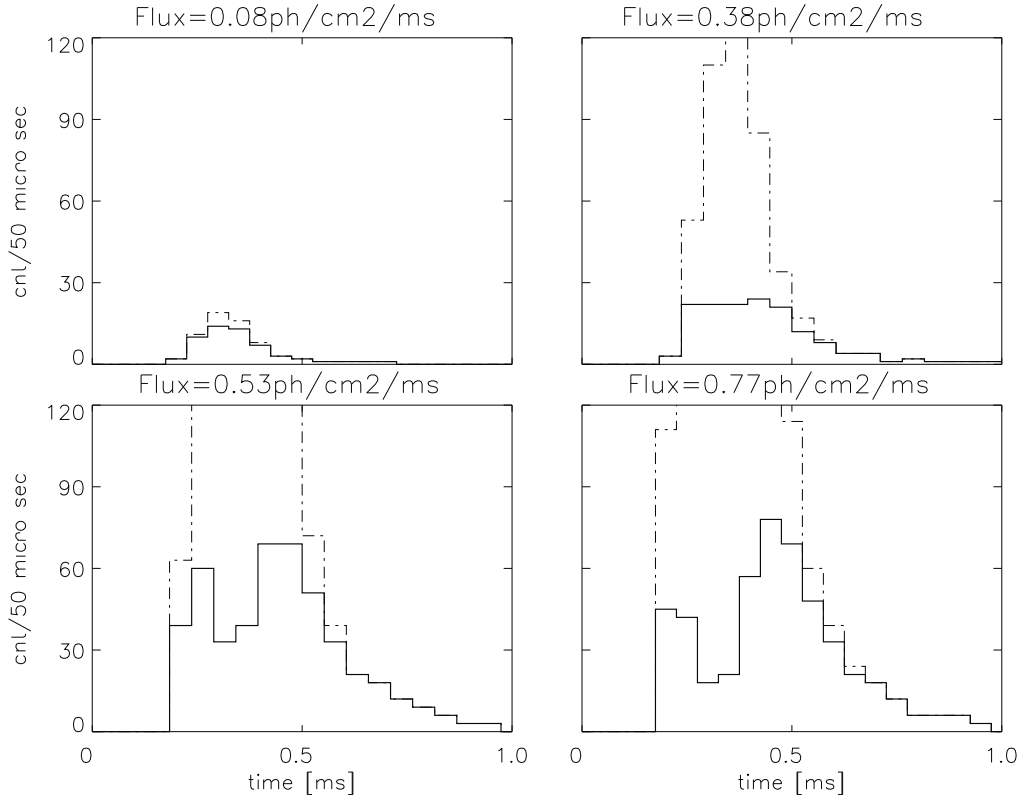

Figure 5. Light curves of a simulated TGF for various incoming photon fluxes. The light curves of pluses created in the LAD are dashed, and the counts in the LAD taking dead time losses into account are shown in solid.

maximum before the two others. The x axis unit is the average flux during the TGF. The y axis unit is the total number of counts per TGF when the incoming photons are folded through the DRM and scaled for dead time losses. Figure 5 shows the resulting light curves for various fluxes (given in the header of each panel). The dashed light curves describe the pulses created in one LAD, and the solid curves are counts with dead time effects included. As the flux approaches the value which gives the maximum in the paralyzation curve (1 photon/cm^2/ms), a single-peaked pulse–light curve transforms into a double-peaked counts–light curve. If the TGF's counts–light curve does not have this single-to-double transition form, then it must be on the left side of the maximum.

[22] Step 5: Determine the production altitude and incoming flux using χ^2 test. *Østgaard et al.* [2008] created a library of Monte Carlo simulated TGFs escaping the atmosphere with various initial assumptions. The library is now modified with the slightly different initial assumptions as already described in section 2. For all the modeled TGFs in our library [*Østgaard et al.*, 2008] we have followed steps 1 to 4. For each modeled TGFs we have also varied the total number of photons. Each of the TGFs are first converted from photons to pulses and then to counts to get an estimate of the measured counts in the four LADs facing the TGF. These estimates are then compared with what BATSE measured in the four LADs with most counts to create a χ^2 between the simulated and the measured TGFs. This calculation leads to a 3-D matrix of χ^2 with spectral index varied from 1.0 to 1.5, altitudes varying from 10 to 30 km and incoming photon number varying from 50 to 1050 photons per TGF where the TGF production duration is from step 1.

[23] Figure 6 (left) shows the χ^2 values of altitude and spectral index with an incoming photons flux of 0.51 photons/cm^2/ms. Figure 6 (right) shows the χ^2 values of altitude and various number of incoming photons fluxes with a constant spectral index 1.0. The degrees of freedom is three (four energy channels). For BATSE TGF 2955 the best fit is an altitude of 23 km with a spectral index of 1.0 and an average incoming photons flux of 0.51 photons/cm^2/ms. The energy spectrum of TGF 2955 is shown in black in Figure 7 (top). The simulated TGF folded through the DRM and corrected for dead time is shown in red in Figure 7.

[24] Step 6: Check if the photon distribution that gave the best fit in production altitude and spectral index also reproduces the observed time delay. After determining the production altitude, spectral index, and the incoming photon flux of the TGF we check the temporal properties by calculating the time delay for the best fit TGF and compare it with the measurements. Figure 7 (bottom) shows the light curve of TGF 2955 and the best-fit simulated TGF, with the corresponding time delay. The time delay is calculated from

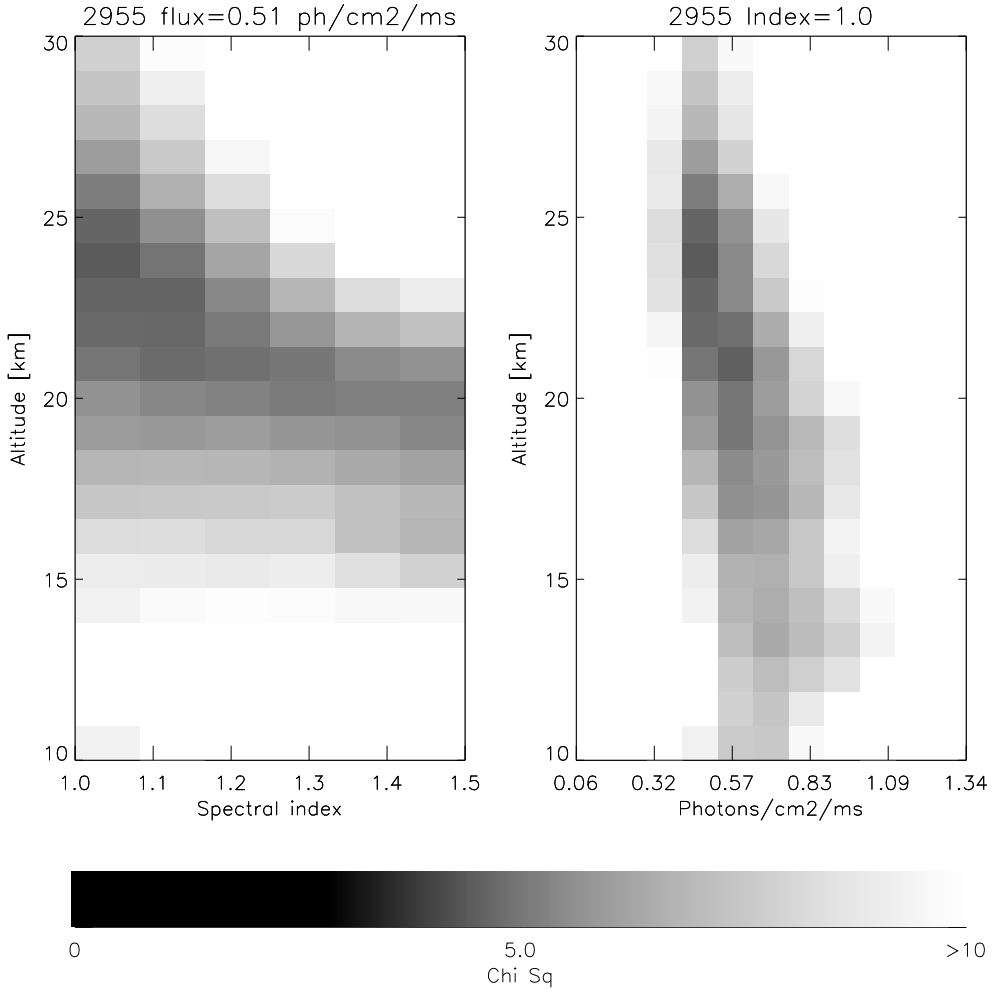

Figure 6. The χ^2 calculated for various production altitudes, spectral indexes, and fluxes. Altitude versus (left) spectral index and (right) average flux.

the light curves of hard and soft photons, where the division is set to 300 keV. The light curves are binned in 25 uniformly logarithmically distributed time bins ranging from 10 to 100 μs, and we use the mean of the minimums from the cross-correlation functions for each time bin size as the time delay. This method is described by *Feng et al.* [2002]. The light curve of TGF 2955 (Figure 7, bottom left) and our modeled TGF (Figure 7, bottom right) are shown. The time delay in our modeled TGF without taking dead time into account is 38 ± 18 μs. When the dead time effects are included, the time delay increases to 118 ± 16 μs. The measured time delay is 145 ± 40 μs.

[25] Step 7: Verifying the zenith angle. An initial assumption in this analysis was that the zenith angle calculated from the relative counts that were measured in each of the four brightest LADs. From equation (3) and Figure 3 it is clear that if the detector is totally paralyzed, the LAD that is hit by most photons may not be the LAD that has the most counts. In such cases the calculated zenith angle would be wrong. However, if we are on the left (lower) side of the peak of the paralyzation curve, in all four LADs, the dead time effects can be corrected and we can reestimate the zenith angle. For all the single-peaked TGFs analyzed in this study the change in zenith angle is less than 10°, which is the angle binning used for our modeled spectra in the library.

[26] Finally, we can also calculate the total number of pulses created in BATSE. The dead time ratio, R, is the ratio between pulses and counts.

$$R = \frac{n_{\text{pulses}}}{n_{\text{counts}}}, \tag{4}$$

and describes how many times brighter, than measurements from BATSE, TGFs are. For TGF 2955 the dead time ratio is 3.77.

3. Results

[27] During its lifetime, BATSE recorded 76 TGF events. The BATSE TGFs have three different time profiles: (1) the

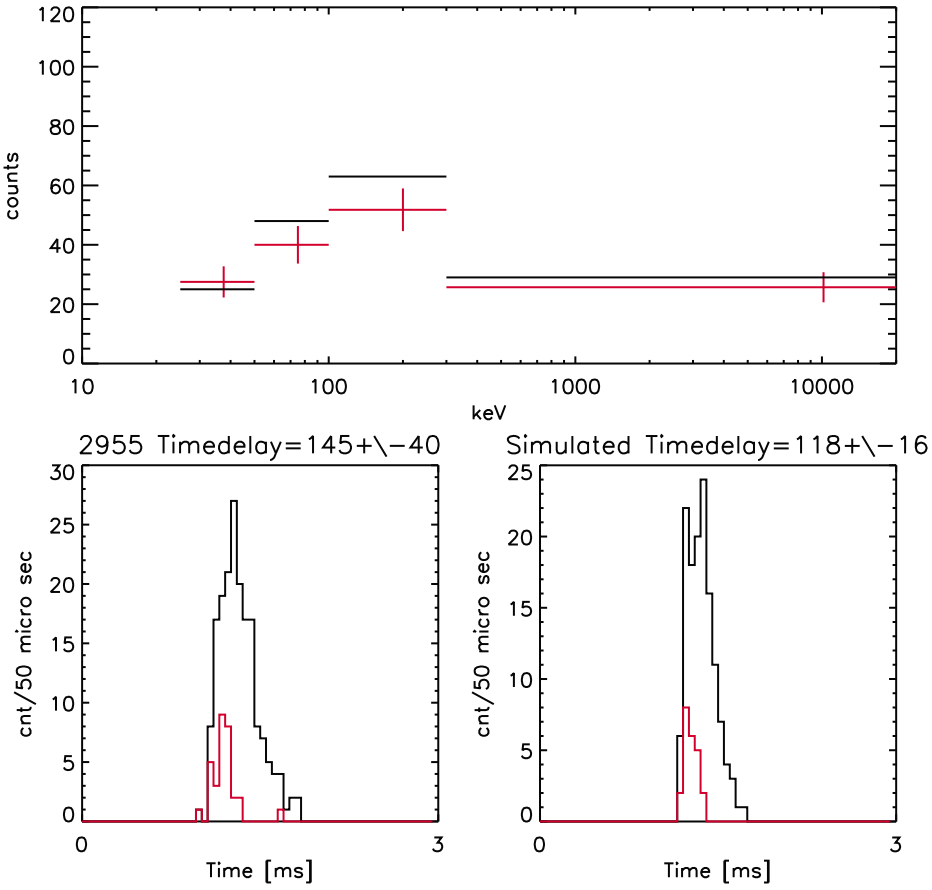

Figure 7. (top) Energy spectrum of BATSE TGF 2955 in black and a simulated TGF from 23 km altitude with a spectral index 1.0 in red. (bottom) Light curves of (left) BATSE TGF 2955 and (right) the simulated TGF light curve. The black curve is the total light curve (channel 1 to 4), and the red curve is the light curve of channel 4. The time delays given in the headers are between channel 1 to 3 and channel 4 in μs.

single-peaked TGFs; (2) the multipeaked TGFs, which contain two or more separate peaks during the event; and (3) the long duration bursts, which are events that last for several milliseconds. As already shown under step 5 in section 2, the TGFs that are measured as single peaks must be single peaks of incoming photons as well. Furthermore, for these TGFs we are confident that the LADs are not paralyzed, and we are on the left and lower side of the peak in Figure 4. For these TGFs the dead time losses can be corrected for.

[28] We have identified five short-duration, single-peaked TGFs that comply with this criterion. For each of them we have preformed the seven steps as described in section 2 to give an altitude, incoming flux, and time delay. We have also studied one double-peaked TGF that may be a result of dead time losses and will be shown and discussed in section 4. This method can also be used on multipeaked TGFs. However, we find that the number of counts in each peak in these cases was too low (<5 counts per channel per peak) to preform a χ^2 analysis.

[29] Table 1 summarizes the results for the five TGFs that have been reanalyzed by using the libraries with beamed spectra and isotropic within a 50° cone. From Table 1 it is clear that the production altitude is reduced when taking dead time into account both for the beamed and isotropic libraries. For TGF 5587 the dead time losses are small, and the results from *Østgaard et al.* [2008] still hold. The given uncertainties in production altitude are where the values of the χ^2 array are increased by $\leq$1 from its minimum.

[30] In the result presented in Table 1 we used $\alpha = 0.75$ μs and $E_0 = 5.5$ keV in equation (2). To see how the dead time effects vary with a different decay time, we did the same analysis with varying α. For $\alpha = 0.5$ μs we found the same production altitude, but the best fit was found at lower incoming photon fluxes. An increase in the dead time will reduce the maximum number of counts a detector can measure. With $\alpha = 1.0$ μs the number of counts in our simulation was significantly lower than in the BATSE TGFs, and consequently, the χ^2 value increases and was

Table 1. Time Delay and Production Altitude[a]

BATSE		Beamed					Cone				Duration
TGF	TD (μs)	Ø (km)	New (km)	TD (μs)	Flux	R	New (km)	TD (μs)	Flux	R	(μs)
2144	125 ± 22	39	17 ± 3	148 ± 22	0.62	3.72	25 ± 3	162 ± 22	0.62	4.52	266
2370	124 ± 18	40	16 ± 4	117 ± 21	0.36	3.08	22 ± 2	96 ± 12	0.36	3.30	222
2465	147 ± 19	26	21 ± 4	137 ± 20	0.49	3.68	24 ± 2	124 ± 17	0.49	4.38	208
2955	145 ± 40	39	22 ± 4	118 ± 16	0.51	3.77	26 ± 2	80 ± 21	0.51	3.77	237
5587	66 ± 34	14	12 ± 1	52 ± 17	0.20	1.46	29 ± 15	54 ± 17	0.28	2.11	555

[a]From *Østgaard et al.* [2008] (Ø) and this study (new) with the beamed and the cone case. The listed flux is the average flux of photons (ph/cm^2/ms) of the TGF. R is the dead time ratio calculated by equation (4). The calculated initial duration of TGFs are shown under the "Duration" column. TD, time delay.

found to be >10 in all TGF. Therefore, the decay time in the BATSE instrument must be ≤1.0 μs.

4. Discussion

4.1. Why Are the Production Altitudes Reduced?

[31] From Table 1, it is clear that the production altitude is significantly reduced when the dead time effects are included in the analysis. All of the single peak TGFs are now between 12 km and 23 km compared to 14 to 40 km from *Østgaard et al.* [2008]. These new altitude estimates are also in agreement with earlier studies [*Dwyer and Smith*, 2005; *Williams et al.*, 2006; *Carlson et al.*, 2007]. We will now discuss how the dead time effects leads to a softer spectrum and consequently a higher estimated production altitude than when dead time effects are included in the analysis.

[32] Figure 8 shows the relationship between the calculated spectral index and the dead time ratio, R, which is derived from equation (4). The spectral index is not the spectral index of the initial TGF spectrum at the production altitude, but the spectral index from a best-fit obtained power law curve of the LADs for energy channels in our simulation after folding the simulated TGF (same as in section 2) through the DRM and scaling it for dead time losses. As the losses due to dead time increase, the measured energy spectrum gets softer. This is a result of the Compton time-delayed tail, shown in Figure 5. The high-energy photons arrive mostly at the peak intensity time of the TGF, the time when the dead time losses are the most significant, while the softer Compton scattered photons arrive later and do not suffer from as much dead time losses. This was also shown by *Grefenstette et al.* [2008].

[33] In simulations performed by *Østgaard et al.* [2008] we showed that TGFs have a softer energy spectrum for increasing production altitudes. The same result is also shown in simulations by *Dwyer et al.* [2008] and *Carlson et al.* [2007]. Therefore, if the TGF suffers from significant dead time losses (i.e., appears softer than they should), an analysis of TGFs without taking dead time losses into account would result in a higher production altitude than an analysis taking this effect into account.

[34] Our results (shown in Table 1) give lower production altitude for beamed case than for the cone case. This is the opposite of results from *Dwyer and Smith* [2005] and *Carlson et al.* [2007]. Both these studies use all photons, out to angles consistent with the satellites' detection thresholds, which escapes the atmosphere in their spectral analysis. In our study we divide our spectra in observation angles. For the beamed case all TGFs are observed outside the production cone, while in the cone case all TGF are observed inside the production cone. *Østgaard et al.* [2008] showed that the energy spectrum is significantly softer when observed outside the production cone than inside. Also, modeled TGFs have a softer energy spectrum when produced at increasing altitudes. Therefore, to fit a given observed spectrum at a given angle, the modeled beamed case implies a lower altitude than the modeled cone case.

4.2. Why Do Dead Time Effects Lead to Larger Time Delays?

[35] The observed time delay in the TGFs is a result of Compton scattering in the atmosphere and dead time losses. *Grefenstette et al.* [2008] showed that dead time losses will increase the time delay in measured TGFs, and the same result is found in this study. High-energy photons arrive at the beginning of the TGF, and as the intensity increases, dead time losses become more significant. The scattered photons, which are reduced in energy, arrive at later times in the TGF. The result of dead time will therefore reduce the number of late arriving high-energy photons and the early arriving low-energy photons, which leads to a longer separation of the hard and the soft light curve. Figure 9 shows how the time delay increases with increasing dead time ratio. The time delay increases rapidly as the dead

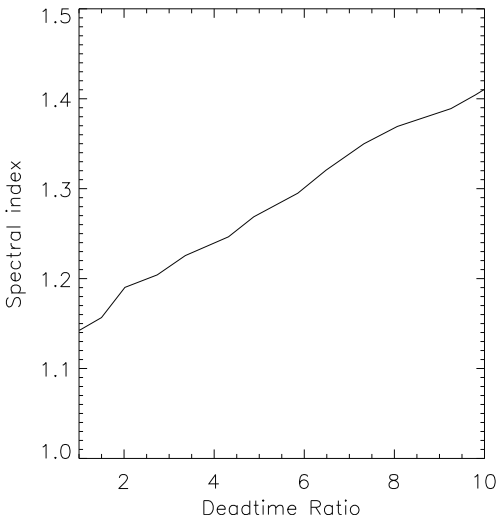

Figure 8. Best-fit power law spectral index of a simulated TGF when dead time effects are included as a function of the dead time ratio from equation (4).

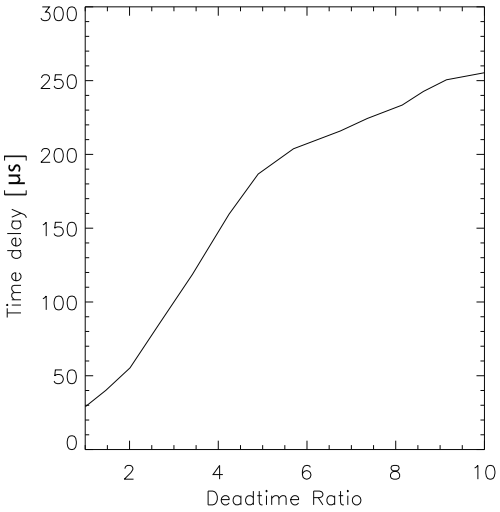

Figure 9. Time delay in simulated TGFs as a function of the dead time ratio from equation (4).

time ratio increases. In the work of *Østgaard et al.* [2008] our simulations showed that the time delay increases as the production altitude decreases. This pattern is not likely to be found in measurements that suffer from dead time losses. The effect of dead time loss on the time delay is greater than the effect of decreasing TGF production altitude. For TGFs of equal intensity produced at different altitudes, high-altitude TGFs will experience less attenuation and will therefore at satellite altitudes have a higher flux, which results in a longer time delay.

[36] As the dead time losses are not significant because of low count rate at the beginning and at the end of the TGFs, these losses do not influence our estimate ($\pm 2\sigma$) of the total duration time. Dead time losses are only important at the peak intensities and even if the peak is increased by a factor of four, the $\pm 2\sigma$ does not change.

4.3. Double Peaks

[37] As shown in step 4 in section 2, a single-peaked TGF can become a double-peaked TGF if the measurements suffer from significantly dead time losses. Most of the multipeaked TGFs have a longer separation between the peaks (>1 ms) than what can be explained by dead time. However, the light curve of TGF 2348 has two peaks separated by ~200 μs. From Figure 5 we have shown that one effect of dead time losses is that a single-peaked TGF can be measured as a double-peaked TGF. By increasing the input flux in our simulation we can reproduce this temporal behavior. In Figure 10 the total (black) and hard ($E > 300$ keV) (red) light curve is shown for TGF 2348 and a TGF from our MC. Both the measured and simulated TGFs have more high-energy counts in the first peak. Since the TGFs gets softer with time, this is what we would expect if dead time losses divide the peak. In the "single-peaked measured as a double" case the dead time ratio for this TGF is ~6. Because of the high incoming photon flux, we have passed the peak of the paralyzation curve (see Figure 4), and we are not able to discuss the spectral properties of TGF 2348. We cannot rule out the possibility that TGF 2348 is actually a double-peaked TGF. In that case the dead time losses are significantly lower than if it is a single-peaked TGF measured as a double.

4.4. Dead Time Effects for Different Types of TGFs

[38] Because of the long trigger window (64 ms), a short event such as a TGF (which typically last 1 ms) needs to be very intense to cause a trigger. Several of the BATSE TGFs contain several peaks, each lasting approx 1 ms. On the basis of the same argument, we would assume that single-peaked TGFs suffer from more dead time losses than the multipeaked TGFs. From these considerations it is likely that all the multipeaked TGFs as well as the long-duration events also are on the left and lower side of the paralyzing peak in Figure 4, and consequently, the dead time losses can be corrected. This argument is also used by *Dwyer et al.* [2008] where five long-duration BATSE events, which

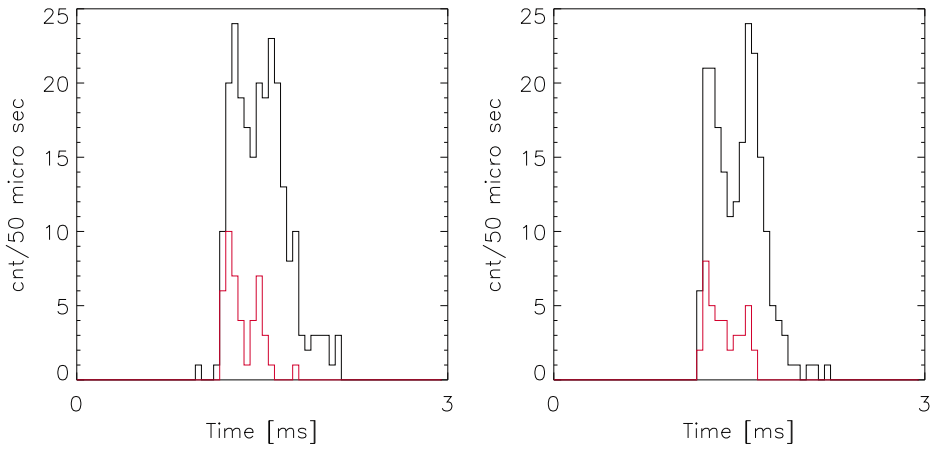

Figure 10. The light curve of (left) BATSE TGF 2348 and (right) simulated TGF. The black curve is the total light curve (channel 1 to 4), and the red is the light curve of channel 4.

were suggested to be electrons and not X-rays entering the detectors, were studied.

4.5. Duration of the Production Mechanism for TGFs

[39] As a side effect of this study, we have also found the initial duration of the TGFs. The duration times, as calculated in step 1, are listed in Table 1. Of the five single-peak TGFs we have analyzed, four have an initial duration time of 200–270 μs, while TGF 5587 has an initial duration of 555 μs. This time scale must reflect the duration of the production mechanism of TGFs.

5. Summary

[40] By modeling the propagation of X-rays through the atmosphere and the interaction of each photon with detector material until it is (or not) detected as a count by the readout electronics, we have reanalyzed five single peak TGFs and found the following:

[41] 1. TGFs that suffer from significant dead time losses (R = 3–4) have a lower production altitude than analyses without dead time. A reanalyzes of five short-duration single-peaked TGFs which in the work of *Østgaard et al.* [2008] were determined to be produced at 26 to 40 km altitude are now reduced to lower altitudes (14–22 km). One TGF, which has lower dead time losses (R = 1.46), was determined to be produced at 12 km altitude in this study and 14 km in the work of *Østgaard et al.* [2008].

[42] 2. The dead time losses increase the time delay between the hard and the soft photons of the TGF, in agreement with earlier results [*Grefenstette et al.*, 2008]. When we account for dead time losses we could reproduce the large time delays which are found in the BATSE TGFs measurements. In this analysis we have found consistent between production altitude and time delay.

[43] 3. The analyzed single-peaked TGFs have dead time ratio up to 4, confirming earlier results [*Grefenstette et al.*, 2008].

[44] 4. We have shown that the double peak of TGF 2348 may be a result of dead time losses. We have shown that a single-peaked TGF can turn into a double-peak TGF. If this TGF is a single-peaked TGF measured as a double, it is ~6 times brighter than measured by BATSE.

[45] 5. In step 1 (described in section 2) we have calculated the duration of the production process of TGF on the basis of the light curve of high-energy photons. This time scale (200 to 600 μs) must reflect the duration of the production mechanism of TGFs.

[46] **Acknowledgments.** Thanks to Nikolai Lethinen and Brant Carlson for useful discussions. This study was supported by the Norwegian Research council under contract 184790/V30.

[47] Zuyin Pu thanks Kenneth Eack and another reviewer for their assistance in evaluating this paper.

References

Carlson, B. E., N. G. Lethinen, and U. S. Inan (2007), Constraints on terrestrial gamma ray flash production from satellite observation, *Geophys. Res. Lett.*, *34*, L08809, doi:10.1029/2006GL029229.

Carlson, B. E., N. G. Lethinen, and U. S. Inan (2009), Terrestrial gamma ray flash production by lightning current pulses, *J. Geophys. Res.*, *114*, A00E08, doi:10.1029/2009JA014531.

Chanrion, O. A., and T. Nubert (2008), A pix-cc code for simulation of streamer propagation in air, *J. Comput. Phys.*, *15*, 7222–7245, doi:10.1016/j.jcp.2008-016.

Cohen, M. B., U. S. Inan, and G. Fishman (2006), Terrestrial gamma ray flashes observed aboard the compton gamma ray observatory/burst and transient source experiment and elf/vlf radio atmospherics, *J. Geophys. Res.*, *111*, D24109, doi:10.1029/2005JD006987.

Cummer, S. A., Y. Zhai, W. Hu, D. M. Smith, L. I. Lopez, and M. A. Stanley (2005), Measurements and implications of the relationship between lightning and terrestrial gamma ray flashes, *Geophys. Res. Lett.*, *32*, L08811, doi:10.1029/2005GL022778.

Dwyer, J. R., and D. M. Smith (2005), A comparison between Monte Carlo simulations of runaway breakdown and terrestrial gamma-ray flash observations, *Geophys. Res. Lett.*, L22804, doi:10.1029/2005GL023848.

Dwyer, J. R., B. W. Grefenstette, and D. M. Smith (2008), High-energy electron beams launched into space by thunderstorms, *Geophys. Res. Lett.*, *35*, L02815, doi:10.1029/2007GL032430.

Feng, H., T. Li, M. Wu, M. Zha, and Q. Q. Zhu (2002), Temporal and spectral properties of gamma-ray flashes, *Geophys. Res. Lett.*, *29*(3), 1036, doi:10.1029/2001GL013992.

Fishman, G. J., et al. (1994), Discovery of intense gamma-ray flashes of atmospheric origin, *Science*, *264*, 1313–1316, doi:10.1126/science.264.5163.1313.

Grefenstette, B. W., D. M. Smith, J. R. Dwyer, and G. J. Fishman (2008), Time evolution of terrestrial gamma ray flashes, *Geophys. Res. Lett.*, *35*, L06802, doi:10.1029/2007GL032922.

Gurevich, A. V., and K. P. Zybin (2001), Runaway breakdown and electric discharges in thunderstorms, *Phys. Uspeki*, *44*, 1119–1140, doi:10.1070/PU2001v044n11ABEH000939.

Inan, U. S., and N. G. Lehtinen (2005), Production of terrestrial gamma-ray flashes by an electromagnetic pulse from a lightning return stroke, *Geophys. Res. Lett.*, *32*, L19818, doi:10.1029/2005GL023702.

Inan, U. S., S. C. Reising, G. J. Fishman, and J. M. Horack (1996), On the association of terrestrial gamma-ray bursts with lightning and implications for sprites, *Geophys. Res. Lett.*, *23*(9), 1017–1020.

Inan, U. S., M. B. Cohen, R. Said, D. M. Smith, and L. I. Lopez (2006), Terrestrial gamma-ray flashes and lightning discharges, *Geophys. Res. Lett.*, *33*, L18802, doi:10.1029/2006GL027085.

Knoll, G. (1989), *Radiation Detection and Measurements*, John Wiley, New York.

Lehtinen, N. G., M. Walt, U. S. Inan, T. F. Bell, and V. P. Pasko (1996), γ-ray emission produced by a relativistic beam of runaway electrons accelerated by quasi-electrostatic thundercloud fields, *Geophys. Res. Lett.*, *23*, 2645–2648, doi:10.1029/96GL02573.

Moss, G., V. P. Pasko, N. Liu, and G. Veronis (2006), Monte Carlo model for analysis of thermal runaway electrons in streamer tips in transient luminous events and streamer zones of lightning leaders, *J. Geophys. Res.*, *111*, A02307, doi:10.1029/2005JA011350.

Nemiroff, R. J., J. T. Bonnell, and J. P. Norris (1997), Temporal and spectral characteristics of terrestrial gamma flashes, *J. Geophys. Res.*, *102*, 9659–9666, doi:10.1029/96JA03107.

Østgaard, N., T. Gjesteland, J. Stadsnes, P. Connell, and B. Carlson (2008), Production altitude and time delays of the terrestrial gamma flashes: Revisiting the burst and transient source experiment spectra., *J. Geophys. Res.*, *113*, A02307, doi:10.1029/2007JA012618.

Roussel-Dupre, R. A., A. V. Gurevich, T. Tunnel, and G. M. Milikh (1994), Kinetic theory of runaway breakdown, *Phys. Rev. E*, *49*, L06802, doi:0.1103/PhysRevE.49.2257.

Smith, D. M., L. I. Lopez, R. P. Lin, and C. P. Barrington-Leigh (2005), Terrestrial gamma-ray flashes observed up to 20 mev, *Science*, *307*(5712), 1085–1088, doi:10.1126/science.1107466.

Stanley, M. A., X. M. Shao, D. M. Smith, L. I. Lopez, M. B. Pongratz, J. D. Harlin, M. Stock, and A. Regan (2006), A link between terrestrial gamma-ray flashes and intracloud lightning discharges, *Geophys. Res. Lett.*, *33*, L06803, doi:10.1029/2005GL025537.

Williams, E., et al. (2006), Lightning flashes conducive to the production and escape of gamma radiation to space, *J. Geophys. Res.*, *111*, D16209, doi:10.1029/2005JD006447.

P. H. Connell, Institute of Mechanical Science, University of Valencia, Calle Tenor Alonso 55, Valencia, E-46110, Spain. (paul.connell@uv.es)

G. J. Fishman, NASA Marshall Space Flight Center, VP 62, Huntsville, AL 35812, USA. (fishman@msfc.nasa.gov)

T. Gjesteland, N. Østgaard, and J. Stadsnes, Department of Physics and Technology, University of Bergen, Allegt 55, N-5007 Bergen, Norway. (thomas.gjesteland@uib.no; nikolai.ostgaard@uib.no; johan.stadsnes@ift.uib.no)

6.3 Paper III

Confining the Angular Distribution of Terrestrial Gamma-ray Flash Emission
T. Gjesteland, N. Østgaard, A. B. Collier, B. E. Carlson, M. B. Cohen and N. G. Lehtinen

J. Geophys. Res., 116, A11313, doi:10.1029/2011JA016716, 2011.

JOURNAL OF GEOPHYSICAL RESEARCH, VOL. 116, A11313, doi:10.1029/2011JA016716, 2011

Confining the angular distribution of terrestrial gamma ray flash emission

T. Gjesteland,[1] N. Østgaard,[1] A. B. Collier,[2,3] B. E. Carlson,[1] M. B. Cohen,[4] and N. G. Lehtinen[4]

Received 1 April 2011; revised 29 August 2011; accepted 29 August 2011; published 11 November 2011.

[1] Terrestrial gamma ray flashes (TGFs) are bremsstrahlung emissions from relativistic electrons accelerated in electric fields associated with thunder storms, with photon energies up to at least 40 MeV, which sets the lowest estimate of the total potential of 40 MV. The electric field that produces TGFs will be reflected by the initial angular distribution of the TGF emission. Here we present the first constraints on the TGF emission cone based on accurately geolocated TGFs. The source lightning discharges associated with TGFs detected by RHESSI are determined from the Atmospheric Weather Electromagnetic System for Observation, Modeling, and Education (AWESOME) network and the World Wide Lightning Location Network (WWLLN). The distribution of the observation angles for 106 TGFs are compared to Monte Carlo simulations. We find that TGF emissions within a half angle >30° are consistent with the distributions of observation angle derived from the networks. In addition, 36 events occurring before 2006 are used for spectral analysis. The energy spectra are binned according to observation angle. The result is a significant softening of the TGF energy spectrum for large (>40°) observation angles, which is consistent with a TGF emission half angle (<40°). The softening is due to Compton scattering which reduces the photon energies.

Citation: Gjesteland, T., N. Østgaard, A. B. Collier, B. E. Carlson, M. B. Cohen, and N. G. Lehtinen (2011), Confining the angular distribution of terrestrial gamma ray flash emission, *J. Geophys. Res.*, *116*, A11313, doi:10.1029/2011JA016716.

1. Introduction

[2] TGFs are short (~1 ms) gamma emissions from the Earth's atmosphere. They were first observed by the Burst and Transient Source experiment (BATSE) on board the Compton Gamma Ray Observatory (CGRO) [*Fishman et al.*, 1994]. These gamma bursts have also been observed by other low Earth orbiting satellites such as the Reuven Ramaty High Energy Solar Spectroscopic Imager (RHESSI) [*Smith et al.*, 2005], AGILE [*Marisaldi et al.*, 2010] and Fermi [*Briggs et al.*, 2010]. TGFs are believed to be bremsstrahlung photons from relativistic electrons accelerated by runaway breakdown processes, a theory suggested nearly a century ago by *Wilson* [1924] and further developed in the 1990s [*Gurevich et al.*, 1992; *Roussel-Dupré et al.*, 1994; *Gurevich et al.*, 1996; *Lehtinen et al.*, 1996]. There is a strong connection between TGFs and thunderstorm activity, and the TGFs are found to occur in association with lightning discharges [*Inan et al.*, 1996; *Cummer et al.*, 2005; *Cohen et al.*, 2006; *Stanley et al.*, 2006; *Cohen et al.*, 2010b; *Shao et al.*, 2010].

[3] Several studies have analyzed the spectral properties of TGFs in order to determine the production altitude and initial angular emission. *Dwyer and Smith* [2005] analyzed RHESSI measurements and found they were best represented by 15 km production altitude and a gamma emission within 45° to vertical, or a narrow vertical gamma beam produced at 21 km. These results were later confirmed by *Carlson et al.* [2007], who also showed that a combined spectrum of the BATSE TGFs was consistent with a 15 km production altitude. *Østgaard et al.* [2008] analyzed each BATSE TGF separately and found that most TGFs were produced at 10–20 km altitude with a significant portion at higher altitudes (30–40 km). It was then shown by *Grefenstette et al.* [2008] that the BATSE instrument was saturated due to deadtime issues in the readout electronics. Motivated by these findings, *Gjesteland et al.* [2010] re-analyzed some of the TGFs that were thought to originate from high altitude (30–40 km) and found that the effect of deadtime saturation made the energy spectrum softer and therefore resulted in a too high production altitude. When deadtime was treated properly the estimated TGF production altitude was found to be 10–20 km in agreement with other studies. This means that both results

[1]Department of Physics and Technology, University of Bergen, Norway.
[2]SANSA Space Science, Hermanus, South Africa.
[3]School of Physics, University of KwaZulu-Natal, Durban, South Africa.
[4]Department of Electrical Engineering, Stanford University, Stanford, California, USA.

0148-0227/11/2011JA016716

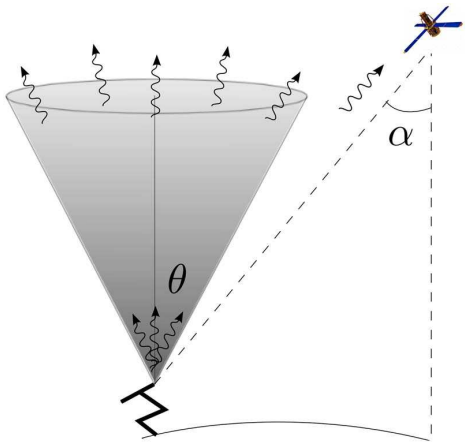

Figure 1. A sketch of the TGF emission cone with half angle θ and the satellite's observation angle α.

from average spectra and single spectrum analysis indicate TGF production ≤20 km.

[4] With a production altitude of 10–20 km, TGFs originate in the upper troposphere, probably inside thunderclouds. Based on gamma-photon attenuation in the atmosphere, *Williams et al.* [2006] suggested that high altitude intracloud lightning is the most likely source of TGFs. Cloud-to-ground lightning could also produce TGFs, however these TGFs are not likely to make it through the atmosphere due to attenuation [*Williams et al.*, 2006].

[5] TGFs are produced by acceleration of electrons in electrical fields that exceeds the runaway threshold. The electrical fields could be between charge regions in thunder clouds or in the strong electric field near leader tips. To gain the high number of electrons needed to produce a detectable TGF, *Dwyer* [2003] showed that positrons and photons may backscatter and create secondary avalanches leading to a true breakdown i.e. a breakdown which is self-sustained and do not need continues seeding to sustain the runaway process. *Moore et al.* [2001] have found energetic radiation associated with lightning stepped-leaders and *Moss et al.* [2006] have shown that streamers can produce enough relativistic seed electrons by acceleration of thermal electrons, such that the TGFs can be produced without feedback effects. *Carlson et al.* [2009, 2010] have shown that it is possible for electrons to be accelerated in the electric field near a leader tip. With seeding, as calculated by *Moss et al.* [2006], the field in leader tips is strong enough to produce TGFs. The electric field in the leader tip is divergent, implying that the TGF emission should be broad with a full width half maximum at half angle ~40° [*Carlson et al.*, 2010, Figure 1f].

[6] The geometry of the initial gamma emission is sketched in Figure 1. In the following we assume a vertical directed gamma emission within a cone given by half angle denoted θ, and the angle between the satellite nadir and the straight line to the TGF source α. The nature of the initial gamma emission is still under debate. Both *Dwyer and Smith* [2005] and *Carlson et al.* [2007] suggested a wide (θ = 45°) emission cone. *Østgaard et al.* [2008] found a softening of the TGF energy spectrum at increasing α which was also found in Monte Carlo (MC) simulations for TGFs observed outside the emission cone. The softening at increasing α was shown to be a result of Compton scattering. When the satellite observes TGFs outside the emission cone only scattered photons are detected. Scattering of photons reduces their energy and therefore leads to a softer energy spectrum. *Hazelton et al.* [2009] used lightning data from the World Wide Lightning Location Network (WWLLN) to divide TGFs into two groups, close and distant, according to whether or not TGFs were observed in association with lightning-producing storms closer than 300 km from the RHESSI sub-satellite point, which corresponds to an observation angle of $\alpha \sim 30°$ when the satellite is at ~600 km altitude. In their study they assumed a narrow and a wide TGF emission. The narrow emission cone was derived from MC simulations in a vertical electric field. The emission intensity (photons/sr) drops one order of magnitude at $\theta \sim 30°$ off axis. To simulate the effect of a divergent electric field, this emission cone was artificially broadened by convolving it with a Gaussian in solid angle. *Hazelton et al.* [2009] found that the wide emission cone provided the best fit to RHESSI data. They also reported 4 distant TGFs where the source lightning was geolocated. They all contained high energy photons ($E > 1$ MeV), which was consistent with their simulations of the broad emission.

[7] This paper will discuss the angular distribution of photon emission in the production of TGFs. In section 2 we will discuss gamma photon production and propagation in the atmosphere to show that the angular distribution of the emission must reflect the direction of the electric field producing TGFs. In section 3 we compare the distribution of the observation angles of RHESSI TGFs with MC simulations. To understand the softening of energy at large α section 4 presents a spectral analysis of TGFs observed at ($\alpha > 40°$). The discussion and conclusions are presented in sections 5 and 6.

2. Bremsstrahlung and Gamma-Photon Propagation in the Atmosphere

[8] The motion of electrons is dictated by the electric and magnetic fields. When the electron collision frequency is much larger than the gyrofrequency, the electron motion is predominantly in the direction of the electric field. *Gurevich et al.* [1996] showed that this is valid at altitudes below 20 km, because the effect of the Earth's magnetic field is negligible.

[9] Bremsstrahlung emitted by relativistic electrons is predominantly in the direction of the electron momentum, as can be seen, e.g., from the Bethe-Heitler formula [*Koch and Motz*, 1959]. The electrons are accelerated in the direction of the electric field and Coulomb scattering will spread their motion into a cone. A MC simulation of relativistic breakdown in a uniform vertical electric field by *Hazelton et al.* [2009] produced a narrow angular gamma emission where the intensity decreases to one half at $\theta \sim 20°$ and one order of magnitude at ~30° of axis. Since gamma emission is in the direction of the electron momentum and the electron momenta are aligned close with the electric field, the initial emission cone of the TGF has to reflect the electric field direction.

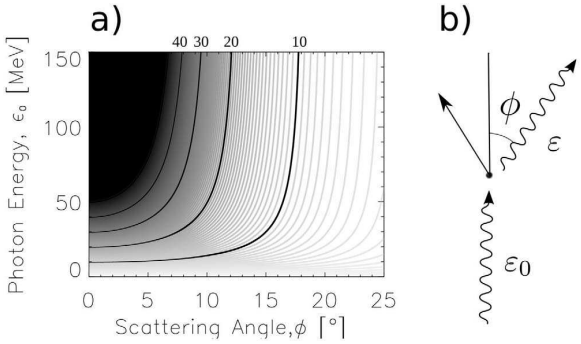

Figure 2. (a) Energy reduction as a function of scattering angle. Y-axis is the energy before scattering and the contour curves represent photon energy after Compton scattering: 10 MeV, 20 MeV, 30 MeV, and 40 MeV contours are labeled. (b) Compton scattering schematics.

[10] Gamma-photon flux propagating in air is attenuated, the most important interactions for photon energies in the range 10 keV–40 MeV being the photoelectric absorption, Compton scattering and pair production. Photoelectric absorption is almost negligible for photon energies above 100 keV and pair production is only effective for energies above 1.22 MeV. While in the photoelectric effect, the photons are absorbed with a production of an electron, in the pair production process, both an electron and a positron are created. Compton scattering is effective for all photon energies and results in scattering of the photon momentum and a loss in the photon energy. The reduction in photon energy is dramatic for large scattering angles. If the photon energy after scattering is 10 MeV it cannot have been scattered by more than 18°, assuming the photon energy before interaction is ≤150 MeV. Figure 2 shows the scattering angle, ϕ, as a function of initial photon energy, ε_0, when the photon energy after scattering, ε, is given. This relation is given by $\varepsilon = \varepsilon_0/(1 + \varepsilon(1 - \cos\phi)/m_e c^2$, where $m_e c^2$ = 511 keV. This is only valid for single Compton scattering events. By multiple scattering the energy reduction is not as dramatic and therefore Monte Carlo simulations are needed to validate the energy spectrum observed at large α.

3. Angular Distribution of TGFs Emission

[11] *Cohen et al.* [2010b] used the AWESOME network to determine the distance from the RHESSI sub-satellite point to the source lightning. A full description of AWESOME can be found in the work by *Cohen et al.* [2010a]. Thirty-six RHESSI TGFs were geolocated, 16 of which were geolocated with measurements from 3 or more stations, with 1σ uncertainty of ~30 km. The two-station cases have significantly larger uncertainties in their location and are therefore not included in this study.

[12] *Collier et al.* [2011] geolocated the source lightning of 93 RHESSI TGFs using WWLLN data, which has a spatial accuracy of 10 km [*Rodger et al.*, 2005]. Three of these TGFs were geolocated by both *Cohen et al.* [2010b] and *Collier et al.* [2011] and the sferic source locations were in agreement within the uncertainties [*Collier et al.*, 2011, Table 1]. This totals to 106 geolocated RHESSI TGFs available for this study. We assume that the TGFs are emitted at the same place and same time as the geolocated sferic. The uncertainties in timing between the sferics and TGFs are dominated by the uncertainties in the RHESSI clock which is assumed to be 1 or 2 ms [*Grefenstette et al.*, 2009]. The uncertainties in sferic timing is >50μs for AWESOME [*Cohen et al.*, 2010b] and 30μs for WWLLN [*Jacobson et al.*, 2006]. We have no information about which type of lightning the geolocated sferics comes from.

[13] The TGF angular distribution from these measurements is compared to calculated angle distributions using the code presented by *Østgaard et al.* [2008]. In this code, the production altitude, TGFs emission direction and energy spectrum are specified as initial conditions. With a production altitude of 15 km, energy spectrum $dN/dE \propto 1/E$ and gamma emission within a cone with half angle θ, Figure 3 shows the calculated scaling factor, $f(\alpha)$, between the initial number of photons, n_0, and the fluence going through a given area at satellite altitude, n_{sat}, as a function of observation angle, α:

$$n_{sat} = n_0 f(\alpha). \quad (1)$$

In Figure 3 all curves are normalized such that $f(0) = 1$. The different curves correspond to various half angle of the initial TGF emission i.e. $\theta = 20°$ (dotted), $\theta = 40°$ (dashed) and $\theta = 60°$ (dash-dotted). The solid curve is proportional to the inverse of the distance squared, demonstrating the reduction in the fluence in the absence of attenuation, referred to as the R^2-effect. Figure 3 shows that atmospheric attenuation reduces the fluence significantly more than the R^2-effect as the observation angle increases. For $\theta = 20°$ the fluence drops by a factor of ~4 if the observations are outside the emission cone. For $\theta = 40°$ the fluence also drops when the observations are outside the emission cone. At $\alpha = 60°$ the fluence has been reduced by more than one order of magnitude for all values of emission breadth θ.

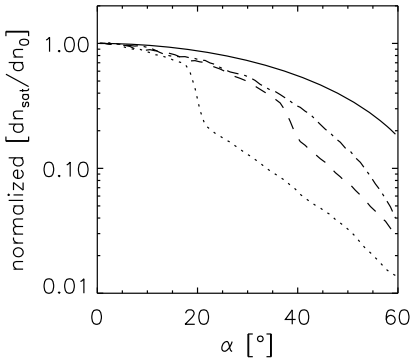

Figure 3. The scaling factor between the number of photons produced in a TGF and the number of photons detected by a satellite calculated by MC simulation. Production altitude is 15 km and $\theta = 20°$ (dotted), $\theta = 40°$ (dashed), and $\theta = 60°$ (dash–dotted). The R^2-effect is shown in solid. All curves are normalized so that $f(0) = 1$.

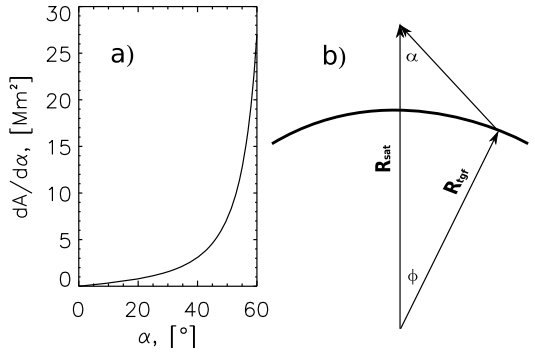

Figure 4. (a) The area as a function of α as given in equation (3). (b) A sketch of the geometry where $\mathbf{R_{SAT}}$ is from Earth's center to the satellite's position and $\mathbf{R_{TGF}}$ is from the Earth's center to the TGF origin.

[14] The number of TGFs per unit area detected by a satellite, $dN/d\alpha$, is given by the product of the area, $dA/d\alpha$, covered by the angle and the number of TGF per unit area exceed the threshold for detection, dN/dA, at that angle:

$$\frac{dN}{d\alpha} = \frac{dN}{dA}\frac{dA}{d\alpha}. \tag{2}$$

This is only valid when we assume that TGFs occur randomly in the satellite's field of view.

[15] A satellite orbiting the Earth covers a larger annular area as the observation angle increases. The area per unit angle in curved Earth geometry is given by:

$$\frac{dA}{d\alpha} = 2\pi R_{TGF}^2 \sin(\phi)\cdot\left(\frac{R_{SAT}}{R_{TGF}}\frac{\cos\alpha}{\cos(\phi+\alpha)} - 1\right), \tag{3}$$

where R_{TGF} and R_{SAT} are the distances from the Earth center to the TGFs origin and the satellite's position, ϕ is the angle between $\mathbf{R_{TGF}}$ and $\mathbf{R_{SAT}}$ given by $\phi = \sin^{-1}(\sin(\alpha)R_{SAT}/R_{TGF}) - \alpha$, $\alpha \in [0, \sin^{-1} R_{SAT}/R_{TGF})]$. $dA/d\alpha$ is shown in Figure 4a with a sketch of the geometry in Figure 4b. In the following we will derive $dN/d\alpha$.

[16] The number of TGF that can be detected at given angle is given by how many TGFs exceeding the threshold level for detection, n_{th}

$$\frac{dN}{dA} = \int_{n_{th}}^{\infty}\frac{dN}{dn_{sat}}dn_{sat}, \tag{4}$$

where dN/dn_{sat} is the distribution of TGFs versus number of photons detected by the satellite. The integral in (4) can be transformed to an integral over n_0 by substituting

$$\frac{dN}{dn_{sat}} = \frac{dN}{dn_0}\frac{dn_0}{dn_{sat}}, \tag{5}$$

where (1) gives $dn_0/dn_{sat} = 1/f(\alpha)$ and $dn_{sat} = f(\alpha)dn_0$. The lower integration limit changes to

$$n_{\min} = \frac{n_{th}}{f(\alpha)}, \tag{6}$$

where $n_{\min}$ is the lowest number of initial photons that will produce a detectable TGF. The upper limit remains at infinity. Substituting this into (4) yields

$$\frac{dN}{dA} = \int_{n_{\min}}^{\infty}\frac{dN}{dn_0}dn_0. \tag{7}$$

We assume that the initial number of photons in a TGF can be distributed according to a power law, which is shown to be feasible [*Collier et al.*, 2011]. Then the number of TGFs with n_0 initial photons are distributed according to

$$\frac{dN}{dn_0} \propto n_0^{-k}, \tag{8}$$

where k is the spectral index. We assume $1.5 < k < 3$. Solving (7) with the power law distribution gives

$$\frac{dN}{dA} \propto \frac{1}{k-1}\left(\frac{n_{th}}{f(\alpha)}\right)^{-k+1}, k > 1 \tag{9}$$

[17] The angular distribution $dN/d\alpha$ given in (2) with dN/dA from (9) and $dA/d\alpha$ from (3) will represent the angular distribution of TGF observations from Monte Carlo simulations for various values of k. Normalizing this distribution yields

$$\frac{dN(\alpha)}{d\alpha} \propto f(\alpha)^{k-1}dA/d\alpha. \tag{10}$$

[18] The distribution in (10), with $f(\alpha)$ from our simulations, are calculated for various k. For each k we have calculated the probability for (10) to represent the distribution of geolocated TGFs. The probability is calculated by a Kolmogorov-Smirnov two-sample test. The results are shown in Figure 5 for production altitudes 15 and 20 km. The three curves are for $\theta = 30°$ (solid), $\theta = 40°$ (dotted) and $\theta = 60°$ (dashed). The horizontal line shows a significance level of 0.05. For both 15 and 20 km production altitude and $\theta = 20°$ (not shown in Figure 5) the probability is below the significance level. From our analysis it follows that both $\theta = 30°$ and $\theta = 60°$ can represent the measured observation angle distribution. Emission cone with $\theta = 60°$ gives a higher spectral index, which means a softer distribution of initial photons, than an emission with $\theta = 30°$. As shown in Figure 5 our simulation only fit the measured distribution when $1.85 < k < 2.80$ for TGF produced at 15 km altitude and $1.90 < k < 2.85$ for TGF produced at 20 km.

[19] Figure 6 shows the observation angle distribution from the RHESSI measurements as a histogram. The best fit distribution from our simulations with various half angles is also shown. Half angle of $\theta = 30°$ with $k = 2.0$ is solid, $\theta = 40°$ with $k = 2.1$ is dotted and $\theta = 60°$ with $k = 2.3$ is dashed. The simulated distributions are normalized to the total number of observations in both *Cohen et al.* [2010b] and *Collier et al.* [2011]. For emission within $\theta = 30°$ our simulations show that most TGFs are detected when the satellite is within the emission cone ($\alpha \leq 30°$). When the satellite is outside the emission cone the number of observed TGF decreases significantly and only the initially brightest TGFs will be detected. An emission with $\theta = 40°$ will also

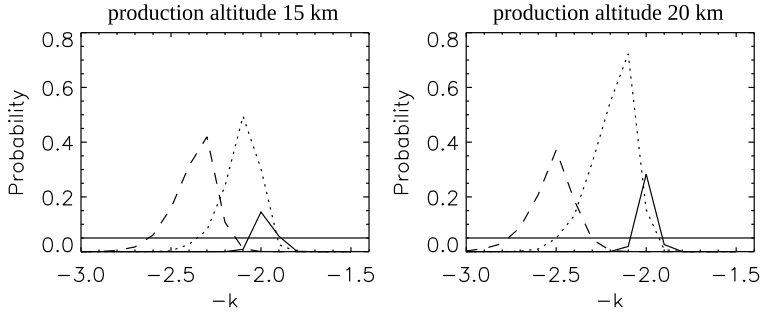

Figure 5. Probability for MC simulations to represent the observed TGF angle distribution for various spectral index, k. Various curves correspond to $\theta = 30°$ (solid), $\theta = 40°$ (dotted), and $\theta = 60°$ (dashed). The horizontal line represents a significant level of 0.05. When the probability is above this line the hypothesis cannot be rejected. TGF production altitude is given in the title of the plots.

give a decrease in number of detected TGFs as the satellite observes outside the emission cone. For $\theta = 60°$ all TGFs at satellite altitude will be detected within the emission cone. As shown in Figure 6 $\theta > 30°$ gives the best fit to the observed distribution.

4. Spectral Analysis of TGFs Observed at Large Angle ($\theta > 40°$)

[20] The energy spectrum of the TGFs can give us further information on the TGF emission cone. From the total set of the TGFs with corresponding geolocated sferics, 36 occurred before the radiation damage to the RHESSI instrument in early 2006 [*Grefenstette et al.*, 2009], and only events occurring before this are valid for proper spectral analysis. We have used the data and detector response matrix (DRM) from the RHESSI TGF catalog [*Grefenstette et al.*, 2009]. For each RHESSI TGF, the detected photons are too few (mean of 26) to perform spectral analysis. Therefore we have composited the measurements from these 36 TGFs into three spectra each with a 20° observation angle bin. Figure 7 shows each energy spectrum with the average number of counts and the error bars representing one standard deviation of the mean value. Figure 7 shows that RHESSI measures a significant softening of the energy spectrum in the 40°–60° bin versus the two others since the first energy bin has significantly more counts and the two highest energy bins have significantly fewer counts. There is also a trend that the 20°–40° spectrum is softer than the 0°–20° spectrum since it has significantly fewer counts in the highest energy bin.

[21] Figure 8 shows a combined energy spectrum of the 10 distant RHESSI TGFs. Distant TGFs are those detected at $\alpha > 40°$, which corresponds to ~500 km between the TGF production and the sub-satellite point. The simulated spectra in Figure 8 are results from our MC simulation folded through the RHESSI DRM. The initial half angle emission shown in Figure 8 is 30°, 40°, 50° and 60° and a production

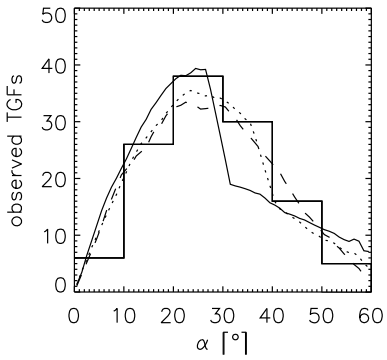

Figure 6. The histogram shows the distribution of geolocated TGFs per observation angle, α. The curves are the best results from MC simulations with $\theta = 30°$, $k = 2.0$ (solid); $\theta = 40°$, $k = 2.1$ (dotted); and $\theta = 60°$, $k = 2.3$ (dashed). The calculations were performed for the TGF source altitude of $h = 15$ km.

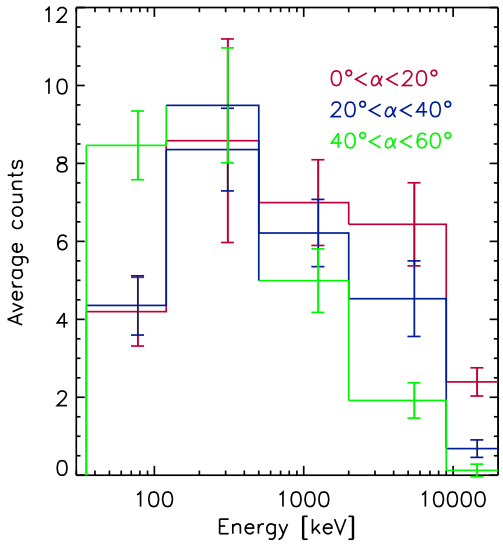

Figure 7. The average energy spectrum for various observation angles, α. The $40° < \alpha < 60°$ spectrum has significantly more counts in the lowest energy bin and significantly fewer counts in the two highest energy bins compared to the others.

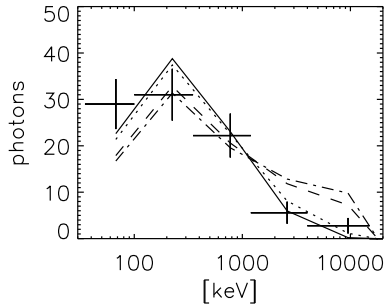

Figure 8. Combined energy spectrum from 10 distant ($\alpha > 40°$) RHESSI TGFs and the energy spectrum from MC simulations with $\theta = 30°$ (solid), $\theta = 40°$ (dotted), $\theta = 50°$ (dashed), and $\theta = 60°$ (dash–dotted). Production altitude of 15 km. The simulated spectra are normalized to the RHESSI measurements.

altitude of 15 km. The simulated spectra only contain photons that escape the atmosphere at $\alpha > 40°$. The simulated spectra are normalized to the combined RHESSI spectrum. The simulated spectra with $\theta \leq 40°$ are detected outside the emission cone. Therefore only scattered photons will be detected. This results in a softening of the energy spectrum. When the observation is obtained inside the emission cone ($\theta = 50°$ and $\theta = 60°$ in Figure 8) high energy photons may propagate directly from the TGF origin to the satellite. This would lead to a harder energy spectrum. In Figure 8 the combined RHESSI spectrum is significantly softer than the simulated spectra with $\theta = 50°$ and $\theta = 60°$, where the reduced χ^2-values are 1.91 ($p = 0.058$) and 2.36 ($p = 0.0108$). For $\theta = 30°$ and $\theta = 40°$ the simulated spectra have a closely matched softening to the combined RHESSI spectrum and the reduced χ^2-values are 0.64 ($p = 0.84$) and 0.84 ($p = 0.68$).

5. Discussion

[22] When calculating the observation angle distribution we have assumed a single TGF production altitude and a gamma emission where the number of photons emitted per solid angle is constant within the emission cone. With these assumptions we find that if TGFs have a narrow emission cone ($\theta = 20°$) the probability for our simulated distributions to represent the measured distribution is lower than a significance level of 0.05 for all values of k. As shown in Figure 5, an emission with $\theta = 30°$ has a peak probability of 0.15 for 15 km production altitude and 0.25 for 20 km production altitude. At both production altitudes the best spectral index is $k = 2.0$. Wider emission cones gives higher probability for our simulations to represent the data with a maximum at $\theta = 40°$. However, we cannot reject any of the hypotheses with $\theta \geq 30°$. An emission cone wider than 60° implies that all TGFs will be detected inside the emission cone and we can therefore not discuss the differences when $\theta > 60°$.

[23] For all emission cones we find that the spectral index should be in the range $1.85 < k < 2.8$ for production altitude 15 km and $1.9 < k < 2.85$ for 20 km. There are two important assumptions which may influence the results.

[24] 1. We have assumed a fixed production altitude. Several studies have shown that the TGF production altitude is in the range of ~14–20 km e.g. [*Smith et al.*, 2005; *Carlson et al.*, 2007; *Gjesteland et al.*, 2010]. Variation in the production altitude will change our constraints in both k and θ. However, since we get approximately similar results for both 15 km and 20 km, the constraints presented here should be valid for the range of most likely production altitudes.

[25] 2. We have assumed an isotropic emission within the cone. *Hazelton et al.* [2009] used an emission cone from MC simulations of runaway electrons. They show that photons emitted from bremsstrahlung in a non-divergent (uniform) electric field are spread with decreasing intensity to one half at $\theta \sim 20°$ and one order of magnitude at ~30° of axis. According to the simulations in the work by *Hazelton et al.* [2009] this is the narrowest emission cone possible from a relativistic runaway avalanche. This is consistent with $\theta \geq 30°$.

[26] Figure 7 shows significantly softer energy spectrum for TGFs observed at $\alpha = 40°$–$60°$ compared to TGFs observed at $\alpha = 0°$–$20°$ or $\alpha = 20°$–$40°$. The modeling results from *Østgaard et al.* [2008] have shown that TGFs sampled inside the emission cone will have a similar energy spectrum at all angles and a significant softening when the TGF is sampled outside the emission cone. This indicates that TGF observed at $\alpha = 40°$–$60°$ are outside the emission cone giving us a constraint that $\theta < 40°$.

[27] In a comparison with WWLLN geolocation of lightning associated with TGFs detected by Fermi Gamma Burst Monitor (GBM), *Connaughton et al.* [2010] found all 15 events to be observed within $\alpha \sim 30°$. *Cohen et al.* [2010b] and *Collier et al.* [2011] found that almost half of the TGFs are observed at $\alpha > 30°$. By comparing these results to MC simulations (see Figure 6), several TGFs observed at larger angles are consistent with simulation. The reason that GBM does not detect distant TGFs could be a result of differences in the trigger algorithm with respect to RHESSI or that GBM is less sensitive to TGFs with softer energy spectra. As shown in Figure 7, distant TGFs have a softer energy spectrum.

[28] The analysis of the angular distribution of TGFs emission (section 3) points toward an emission cone with $\theta \geq 30°$. The spectral analysis (section 4) indicates $\theta < 40°$. The range $30° < \theta < 40°$ is a little narrower than the half angle found in some earlier studies. *Dwyer and Smith* [2005] concluded that $\theta = 45°$ gave the best fit to the combined RHESSI spectrum and *Carlson et al.* [2007] concluded that $\theta \geq 45°$ could best represent the data.

[29] *Hazelton et al.* [2009] found that their wide emission cone, which had an intensity drop one order of magnitude at $\theta \sim 70°$ and 15 km production altitude, gave the lowest χ^2-value. However, they found that no single model (wide or narrow) fits all the data perfectly. *Hazelton et al.* [2009] separated TGFs into close and distant events. Close events are when there is lightning activity closer than 300 km from the sub-satellite point, which corresponds to $\alpha \sim 30°$. *Hazelton et al.* [2009] did not use detailed time coincidences between RHESSI and WWLLN events, but found plausible thunder storms.

[30] We found the half angle of the emission cone at $\theta \sim 40°$, therefore the distant energy spectrum in the work by

Hazelton et al. [2009] may include both direct and scattered TGFs photons. The inclusion of direct photons reduces the softening of the distant energy spectrum. A softer distant energy spectrum would fit better to their wide cone assumption [*Hazelton et al.*, 2009, Figure 1]. This indicates that an isotropic emission within $30° < \theta < 40°$ is comparable to the wide cone of *Hazelton et al.* [2009].

[31] *Carlson et al.* [2010] showed that if TGFs are produced by active lightning leader channels the gamma emission should be broad. The gamma emission predicted by *Carlson et al.* [2010, Figure 1f] drops one order of magnitude at $\theta \sim 90°$. The energy distribution of the photons emitted at large angles is not known. High energy photons emitted at large angles are not consistent with the softening of the energy spectrum found in this study.

[32] Our study indicates that the emissions are within $30° < \theta < 40°$. Assuming that the emission from a runaway breakdown in vertical electric field is emitted within $\theta \sim 20°$, which is where the intensity drops to one half in the simulation by *Hazelton et al.* [2009], our result suggest that TGFs are produced in electric fields that may have up to 20° deviation from vertical.

[33] In section 3 we assumed the TGF intensity to be distributed according to a power law and found the spectral index to be in the range $1.85 < k < 2.85$ for $\theta \geq 30°$. Since we confined the upper limit of the emission half angle to be $\theta \leq 40°$ our study indicates that the power law fit to the TGF intensity should have a spectral index $1.9 < k < 2.5$.

[34] RHESSI is known to suffer from deadtime [*Grefenstette et al.*, 2009] saturation. If TGFs saturates the detectors as much as they will not be detected the TGFs lost due to deadtime issues would be biased to short and bright TGFs [*Smith et al.*, 2010]. From our simulations the brightest TGFs are observed close to the sub satellite point. Both the R^2-effect and scattering and absorptions effects reduces the brightness at larger α. Simulations [*Gjesteland et al.*, 2010; *Grefenstette et al.*, 2008] showed that a TGF measured at larger α contain a Compton tail i.e. a tail of late arriving photons due to Compton scattering, which increase the TGF duration. Therefore, if RHESSI loses TGF due to deadtime it will manly lose TGFs at low α. If the distribution of detected TGFs are shifted to lower α that would imply a more narrow emission cone than presented in this study.

6. Summary

[35] We have used accurate geolocation of RHESSI TGFs to confine the angular TGF emission. When assuming an isotropic emission cone the half angle is confined to $30° < \theta < 40°$. This indicates that TGFs are produced in a vertical or nearly-vertical orientation (up to 20° from vertical) electric field.

[36] Our simulations shows that it is likely to detect TGFs at $\alpha > 50°$ which corresponds to >700 km between the source sferic and the sub-satellite point. We have also found that TGFs detected at $\alpha > 40°$ have a significantly softer energy spectrum, which has been interpreted to result from Compton scattering.

[37] Assuming that the total TGF intensities are distributed according to a power law (as suggested by *Collier et al.* [2011]), we confine the spectral index to $1.9 < k < 2.5$.

[38] **Acknowledgments.** This study was supported by the Research Council of Norway under contracts 184790/V30 and 197638/V30. Nikolai Lehtinen, Morris Cohen, and Brant Carlson would like to acknowledge support from NSF grant ATM-0836326. Nikolai Lehtinen would like to acknowledge support from DARPA grant HR0011-10-1-0058-P00001.

[39] Robert Lysak thanks the reviewers for their assistance in evaluating this manuscript.

References

Briggs, M. S., et al. (2010), First results on terrestrial gamma ray flashes from the Fermi Gamma-ray Burst Monitor, *J. Geophys. Res.*, *115*, A07323, doi:10.1029/2009JA015242.

Carlson, B. E., N. G. Lehtinen, and U. S. Inan (2007), Constraints on terrestrial gamma ray flash production from satellite observation, *Geophys. Res. Lett.*, *34*, L08809, doi:10.1029/2006GL029229.

Carlson, B. E., N. G. Lehtinen, and U. S. Inan (2009), Terrestrial gamma ray flash production by lightning current pulses, *J. Geophys. Res.*, *114*, A00E08, doi:10.1029/2009JA014531.

Carlson, B. E., N. G. Lehtinen, and U. S. Inan (2010), Terrestrial gamma ray flash production by active lightning leader channels, *J. Geophys. Res.*, *115*, A10324, doi:10.1029/2010JA015647.

Cohen, M. B., U. S. Inan, and G. Fishman (2006), Terrestrial gamma ray flashes observed aboard the Compton Gamma Ray Observatory/Burst and Transient Source Experiment and ELF/VLF radio atmospherics, *J. Geophys. Res.*, *111*, D24109, doi:10.1029/2005JD006987.

Cohen, M., U. Inan, and E. Paschal (2010a), Sensitive broadband ELF/VLF radio reception with the AWESOME instrument, *IEEE Trans. Geosci. Remote Sens.*, *48*(1), 3–17, doi:10.1109/TGRS.2009.2028334.

Cohen, M. B., U. S. Inan, R. K. Said, and T. Gjestland (2010b), Geolocation of terrestrial gamma-ray flash source lightning, *Geophys. Res. Lett.*, *37*, L02801, doi:10.1029/2009GL041753.

Collier, A. B., T. Gjesteland, and N. Østgaard (2011), Assessing the power law distribution of TGFs, *J. Geophys. Res.*, *116*, A10320, doi:10.1029/2011JA016612.

Connaughton, V., et al. (2010), Associations between Fermi Gamma-ray Burst Monitor terrestrial gamma ray flashes and sferics from the World Wide Lightning Location Network, *J. Geophys. Res.*, *115*, A12307, doi:10.1029/2010JA015681.

Cummer, S. A., Y. Zhai, W. Hu, D. M. Smith, L. I. Lopez, and M. A. Stanley (2005), Measurements and implications of the relationship between lightning and terrestrial gamma ray flashes, *Geophys. Res. Lett.*, *32*, L08811, doi:10.1029/2005GL022778.

Dwyer, J. R. (2003), A fundamental limit on electric fields in air, *Geophys. Res. Lett.*, *30*(20), 2055, doi:10.1029/2003GL017781.

Dwyer, J. R., and D. M. Smith (2005), A comparison between Monte Carlo simulations of runaway breakdown and terrestrial gamma-ray flash observations, *Geophys. Res. Lett.*, *32*, L22804, doi:10.1029/2005GL023848.

Fishman, G. J., et al. (1994), Discovery of intense gamma-ray flashes of atmospheric origin, *Science*, *264*, 1313–1316, doi:10.1126/science.264.5163.1313.

Gjesteland, T., N. Østgaard, P. H. Connell, J. Stadsnes, and G. J. Fishman (2010), Effects of dead time losses on terrestrial gamma ray flash measurements with the Burst and Transient Source Experiment, *J. Geophys. Res.*, *115*, A00E21, doi:10.1029/2009JA014578.

Grefenstette, B. W., D. M. Smith, J. R. Dwyer, and G. J. Fishman (2008), Time evolution of terrestrial gamma ray flashes, *Geophys. Res. Lett.*, *35*, L06802, doi:10.1029/2007GL032922.

Grefenstette, B. W., D. M. Smith, B. J. Hazelton, and L. I. Lopez (2009), First RHESSI terrestrial gamma ray flash catalog, *J. Geophys. Res.*, *114*, A02314, doi:10.1029/2008JA013721.

Gurevich, A. V., G. M. Milikh, and R. Roussel-Dupre (1992), Runaway electron mechanism of air breakdown and preconditioning during a thunderstorm, *Phys. Lett. A*, *165*, 463–468, doi:10.1016/0375-9601(92)90348-P.

Gurevich, A. V., J. A. Valdivia, G. M. Milikh, and K. Papadopoulos (1996), Runaway electrons in the atmosphere in the presence of a magnetic field, *Radio Sci.*, *31*(6), 1541–1554, doi:10.1029/96RS02441.

Hazelton, B. J., B. W. Grefenstette, D. M. Smith, J. R. Dwyer, X.-M. Shao, S. A. Cummer, T. Chronis, E. H. Lay, and R. H. Holzworth (2009), Spectral dependence of terrestrial gamma-ray flashes on source distance, *Geophys. Res. Lett.*, *36*, L01108, doi:10.1029/2008GL035906.

Inan, U. S., S. C. Reising, G. J. Fishman, and J. M. Horack (1996), On the association of terrestrial gamma-ray bursts with lightning and implications for sprites, *Geophys. Res. Lett.*, *23*(9), 1017–1020, doi:10.1029/96GL00746.

Jacobson, A. R., R. H. Holzworth, J. Harlin, R. L. Dowden, and E. H. Lay (2006), Performance assessment of the World Wide Lightning Location Network (WWLLN), using the Los Alamos Sferic Array (LASA) as

ground truth, *J. Atmos. Oceanic Technol.*, *23*, 1082–1092, doi:10.1175/JTECH1902.1.

Koch, H. W., and J. W. Motz (1959), Bremsstrahlung cross-section formulas and related data, *Rev. Mod. Phys.*, *31*(4), 920–955, doi:10.1103/RevModPhys.31.920.

Lehtinen, N. G., M. Walt, U. S. Inan, T. F. Bell, and V. P. Pasko (1996), γ-ray emission produced by a relativistic beam of runaway electrons accelerated by quasi-electrostatic thundercloud fields, *Geophys. Res. Lett.*, *23*(19), 2645–2648, doi:10.1029/96GL02573.

Marisaldi, M., et al. (2010), Detection of terrestrial gamma ray flashes up to 40 MeV by the AGILE satellite, *J. Geophys. Res.*, *115*, A00E13, doi:10.1029/2009JA014502.

Moore, C. B., K. B. Eack, G. D. Aulich, and W. Rison (2001), Energetic radiation associated with lightning stepped-leaders, *Geophys. Res. Lett.*, *28*(11), 2141–2144, doi:10.1029/2001GL013140.

Moss, G. D., V. P. Pasko, N. Liu, and G. Veronis (2006), Monte Carlo model for analysis of thermal runaway electrons in streamer tips in transient luminous events and streamer zones of lightning leaders, *J. Geophys. Res.*, *111*, A02307, doi:10.1029/2005JA011350.

Østgaard, N., T. Gjesteland, J. Stadsnes, P. H. Connell, and B. Carlson (2008), Production altitude and time delays of the terrestrial gamma flashes: Revisiting the Burst and Transient Source Experiment spectra, *J. Geophys. Res.*, *113*, A02307, doi:10.1029/2007JA012618.

Rodger, C. J., J. B. Brundell, and R. L. Dowden (2005), Location accuracy of VLF World-Wide Lightning Location (WWLL) network: Post-algorithm upgrade, *Ann. Geophys.*, *23*(2), 277–290.

Roussel-Dupré, R. A., A. V. Gurevich, T. Tunnell, and G. M. Milikh (1994), Kinetic theory of runaway air breakdown, *Phys. Rev. E*, *49*(3), 2257–2271, doi:10.1103/PhysRevE.49.2257.

Shao, X.-M., T. Hamlin, and D. M. Smith (2010), A closer examination of terrestrial gamma-ray flash-related lightning processes, *J. Geophys. Res.*, *115*, A00E30, doi:10.1029/2009JA014835.

Smith, D. M., L. I. Lopez, R. P. Lin, and C. P. Barrington-Leigh (2005), Terrestrial gamma-ray flashes observed up to 20 MeV, *Science*, *307*, 1085–1088, doi:10.1126/science.1107466.

Smith, D. M., B. J. Hazelton, B. W. Grefenstette, J. R. Dwyer, R. H. Holzworth, and E. H. Lay (2010), Terrestrial gamma ray flashes correlated to storm phase and tropopause height, *J. Geophys. Res.*, *115*, A00E49, doi:10.1029/2009JA014853.

Stanley, M. A., X.-M. Shao, D. M. Smith, L. I. Lopez, M. B. Pongratz, J. D. Harlin, M. Stock, and A. Regan (2006), A link between terrestrial gamma-ray flashes and intracloud lightning discharges, *Geophys. Res. Lett.*, *33*, L06803, doi:10.1029/2005GL025537.

Williams, E., et al. (2006), Lightning flashes conducive to the production and escape of gamma radiation to space, *J. Geophys. Res.*, *111*, D16209, doi:10.1029/2005JD006447.

Wilson, C. T. R. (1924), The electric field of a thundercloud and some of its effects, *Proc. Phys. Soc. London*, *37*, 32D–37D.

B. E. Carlson, T. Gjesteland, and N. Østgaard, Department of Physics and Technology, University of Bergen, Allegaten 55, N-5007 Bergen, Norway. (brant.carlson@ift.uib.no; thomas.gjesteland@uib.no; nikolai.ostgaard@uib.no)

M. B. Cohen and N. G. Lehtinen, Department of Electrical Engineering, Stanford University, 350 Serra Mall, Stanford, CA 94305, USA. (mcohen@stanford.edu; nleht@stanford.edu)

A. B. Collier, School of Physics, University of KwaZulu-Natal, Westville Campus, Durban 4000, South Africa. (collierab@gmail.com)

6.4 Paper IV

A new method reveals more TGFs in the RHESSI data
T. Gjesteland ,N. Østgaard, A. B. Collier, B. E. Carlson, C. Eyles, D. M. Smith

Geophys. Res. Lett., 39, L05102, doi:10.1029/2012GL050899, 2012

GEOPHYSICAL RESEARCH LETTERS, VOL. 39, L05102, doi:10.1029/2012GL050899, 2012

A new method reveals more TGFs in the RHESSI data

T. Gjesteland,[1] N. Østgaard,[1] A. B. Collier,[2,3] B. E. Carlson,[1] C. Eyles,[4] and D. M. Smith[5]

Received 10 January 2012; revised 8 February 2012; accepted 9 February 2012; published 7 March 2012.

[1] This letter presents a new search algorithm for identifying Terrestrial Gamma ray Flashes (TGFs) in the Reuven Ramaty High Energy Solar Spectroscopic Imager (RHESSI) data. The algorithm has been applied to data from the period 2004–2006 and we have found more than twice as many TGFs as previously reported. The new TGFs follow the same geographical and seasonal variations as the previously reported TGFs. The match percentage between the new TGFs and World Wide Lightning Location Network (WWLLN) data is comparable to the RHESSI catalog TGFs. Our results shows that previous searches only identified the most intense events, and that there might be a large population of faint TGFs. **Citation:** Gjesteland, T., N. Østgaard, A. B. Collier, B. E. Carlson, C. Eyles, and D. M. Smith (2012), A new method reveals more TGFs in the RHESSI data, *Geophys. Res. Lett.*, *39*, L05102, doi:10.1029/2012GL050899.

1. Introduction

[2] TGFs were discovered by *Fishman et al.* [1994] and since then a few satellites have made TGF observations [*Smith et al.*, 2005; *Marisaldi et al.*, 2010a; *Briggs et al.*, 2011]. The majority of TGFs have been observed by RHESSI. By September 2010 the RHESSI catalog contained 975 TGFs, and the instrument is still operating [*Grefenstette et al.*, 2009]. Observations by other spacecraft add up to a few hundreds of TGFs. The Burst And Transient Source Experiment (BATSE) observed 78 TGFs (http://gammaray.msfc.nasa.gov/batse/misc/triggers.html) during its eight year mission. Fermi observed 50 TGFs during their first 21 months of operation [*Fishman et al.*, 2011]. Astrorivelatore Gamma a Immagini Leggero (AGILE) has observed 130 events satisfying stringent TGF selection criteria during the period June 2008 to January 2010 [*Tavani et al.*, 2011]. In addition one TGF has been observed from an airplane by the Airborne Detector for Energetic Lightning Emissions (ADELE) [*Smith et al.*, 2011]. The limited number of events is partially due to the high trigger threshold imposed on the data in order to eliminate spurious events. Relaxing the trigger criteria leads to increasing TGF detection rates [*Fishman et al.*, 2011]. The population of fainter TGFs is currently unknown.

[3] TGFs have a typical duration of less than 1 ms. The average duration of the RHESSI catalog TGFs is $\sim 0.6 - 0.7$ ms [*Smith et al.*, 2010]. By correcting for deadtime in the BATSE instrument, *Gjesteland et al.* [2010] determined the TGF duration of five TGFs to be between 0.2 ms and 0.3 ms. New results from Fermi have shown that TGFs can be as short as 50 μs [*Fishman et al.*, 2011]. Despite the different methods used to determine TGF duration, the consensus is that typical TGFs are significantly shorter than 1 ms.

[4] Observed TGFs have an energy spectrum $\propto 1/E$ with an exponential cutoff [*Dwyer and Smith*, 2005] where the energy of single photons may be up to several tens of MeV's [*Smith et al.*, 2005; *Marisaldi et al.*, 2010b].

[5] The RHESSI TGF catalog is presented by *Grefenstette et al.* [2009] and can be found at http://scipp.ucsc.edu/~dsmith/tgflib_public. In the following we will refer to these TGFs as the catalog TGFs. *Grefenstette et al.* [2009] also present results from an alternative search algorithm. The numbers and quality of these new events were not quantified, but clearly indicate that there are more TGFs than presented in the catalog.

[6] In this letter we present a new and optimized search algorithm which has been applied to the RHESSI data and show that there are many more RHESSI TGFs than previously reported.

2. Search Algorithm

[7] RHESSI consists of nine segmented germanium detectors for X- and γ- ray detection in the energy range from 3 keV to 17 MeV, where the rear detectors measures counts with energy > 25 keV. For more description of the RHESSI instrument refer to *Smith et al.* [2002] and *Grefenstette et al.* [2009]. The raw RHESSI data are available at: http://hesperia.gsfc.nasa.gov/hessidata.

[8] We use data from the rear RHESSI detectors, considering only counts with energy > 30 keV. Detector G2 was operating poorly, in an unsegmented mode at low voltage, during 2004–2006. As in the work by *Grefenstette et al.* [2009] G2 is not included in our search. Since a high energy photon may deposit energy in more than one detector we combine counts that are detected within ± 1 binary microsecond (2^{-20}s) and regard these counts as one photon. This was also done by *Grefenstette et al.* [2009].

[9] Our search algorithm is in two steps, first a coarse search and then a fine search. The following definitions will be used. The result from the coarse search is called an *event*. If the event passes the fine search we call it a *trigger* and if it also passes a final set of selection criteria which is described below, we call it a TGF.

[10] In the coarse search we use a 1 ms search window. Since TGFs typically last < 1 ms the entire TGF will be within the 1 ms search window. However, there is a

[1]Department of Physics and Technology, University of Bergen, Bergen, Norway.
[2]SANSA Space Science, Hermanus, South Africa.
[3]Space Physics Research Institute, University of KwaZulu-Natal, Durban, South Africa.
[4]Image Processing Laboratory, University of Valencia, Valencia, Spain.
[5]Physics Department and Santa Cruz Institute for Particle Physics, University of California, Santa Cruz, California, USA.

0094-8276/12/2012GL050899

possibility that a given TGF is divided between two consecutive search windows. To avoid this we move the 1 ms search window in steps of 0.5 ms.

[11] For each window we calculate the expected number of background counts for that window. The number of expected background counts is calculated using the average background count rate over times range $t \in [-220, -20]$ ms and $t \in [20, 220]$ ms, where $t = 0$ is the time at the beginning of the search window. The reason for not including the 40 ms around the search window is to exclude the counts from the event itself. While RHESSI TGFs are typically < 1 ms, electron beams produced by TGFs may be up to 25 ms [*Dwyer et al.*, 2008; *Carlson et al.*, 2009, 2011; *Briggs et al.*, 2011]. The average RHESSI background rate is two counts per ms [*Grefenstette et al.*, 2009].

[12] For each window we calculate the probability of getting a false event assuming the background follows a Poisson process:

$$p(x \geq X|N) = 1 - e^{-N} \sum_{i=0}^{X-1} \frac{N^i}{i!}, \quad (1)$$

where N is the number of expected background counts in the search window and X is the number of counts in the search window. Windows where $p(x \geq X|N) < 10^{-6}$ are called an event. The events are then moved to the fine search. With $p < 10^{-6}$ we would expect $\sim 3 \cdot 10^4$ events per year. However, we found $\sim 10^5$ events per year which we believe is a result of cosmic rays creating several counts in the detectors.

[13] In the fine search we use three sliding search windows; 0.3 ms, 1 ms and 3 ms. As in the coarse search we calculate the probability to measure the number of counts in the search window, X, or greater given an expected background of N, but with a more stringent requirement. If $p(x \geq X|N) < p_{\max}$, where $p_{\max}$ is a chosen threshold, we call the event a trigger. In one year there are $\sim 3 \cdot 10^{10}$ intervals of length 1 ms and since our smallest search window is 0.3 ms there are $\sim 10^{11}$ independent search windows per year. Choosing $p_{\max} = 10^{-11}$, means that we expect to have one false trigger per year due to statistical fluctuations.

[14] To be identified as a TGF a trigger from the fine search must fulfill five selection criteria:

1. Triggers where the background before and after the trigger varies by more than 15% are rejected. This removes triggers artificially caused by event data being turned back on as the satellite leaves the South Atlantic Magnetic Anomaly (SAMA), as well as other false triggers due to a sudden change in background count rate.

2. The duration of a trigger should be more than 0.1 ms and less than 3 ms. The lower duration criterion remove possible cosmic rays which last $\ll 0.01$ ms, but may last up to 0.05 ms in the electronics [*Grefenstette et al.*, 2009]. The longer duration criterion removes possible TGF electron beams which typically last 5–25 ms [*Dwyer et al.*, 2008; *Carlson et al.*, 2009, 2011]. It also removes soft gamma ray repeaters and solar flares which both have longer durations. The duration is determined as $\pm 2\sigma$ of a Gaussian fit to the light curve with bin size of 0.25 ms. Since TGFs may be shorter than the bin size, we have used the same method as *Grefenstette et al.* [2009] to calculate the lower end of the duration, that is, we require that the time between the first and the last photon in the 0.3 ms trigger window should be more than 0.1 ms.

3. To avoid false triggers caused by high voltage arcing in any one of the RHESSI detectors [*Grefenstette et al.*, 2009] only allowed at most 25% of the counts in one detector. We have relaxed this criterion slightly: For the distribution of counts in the eight detectors we require that the value of $\sigma/\sqrt{n} < 1.5$, where σ and n are the standard deviation and the mean of the distribution. A Monte Carlo test of this criterion has shown that this method falsely rejects $\sim 0.2\%$.

4. The hardness ratio H_r of the trigger is determined as the number of counts with energy $E > 1$ MeV divided by the number of counts with energy $E \leq 1$ MeV. Triggers where $H_r \leq 0.025$ are rejected. For TGFs with < 40 counts this criterion implies at least one count with energy > 1 MeV.

5. Triggers where the number of overflow counts (counts with energy > 17 MeV) is larger than 30% are rejected. This criterion removes triggers which we believe comes from high energy deposit by cosmic rays that are not removed by the other criteria.

3. Results

[15] Figure 1 shows three example TGFs from our search. Figures 1a–1c show the light curve and a scatter plot of energy versus time for the counts in the TGFs. The TGF in Figure 1a with $p = 3.07 \cdot 10^{-12}$ is the one found over the Sahara desert, which is a place we do not expect to observe TGFs. However, it could be a part of a TGF electron beam as reported by *Dwyer et al.* [2008] and *Briggs et al.* [2011]. Figure 1b shows one of the weakest TGFs found in the new search ($p = 8.16 \cdot 10^{-12}$) and contains only 11 counts. The TGF in Figure 1c with $p < 10^{-16}$ is a typical TGF. This one is also in the RHESSI catalog.

[16] In the data from 2004, 2005 and 2006 we found a total of 1012 TGFs, of which 958 passed our criteria with a 0.3 ms search window, 648 with 1 ms search window and 272 with 3 ms search window. Figure 1d shows the new TGFs as red circles and the catalog TGFs as green dots. For the period 2004–2006 the RHESSI catalog contains 474 TGFs of which our search algorithm found 458. Hence, there are 16 catalog TGFs which are not found in this new search. Seven of these had $p > 10^{-11}$ and so the rest were rejected due to the criteria we applied.

[17] We have searched for matches between the new RHESSI TGFs and WWLLN events as described by *Collier et al.* [2011]. A match is defined when a WWLLN event occurs closer than 2400 km from the RHESSI sub satellite point within ± 10 ms of the TGF. The result is shown in Table 1. We found that the number of matches is slightly higher than reported by *Collier et al.* [2011]. They found that the catalog TGFs that matched with the WWLLN events were from the weaker part of the TGF intensity distribution. Thus the comparable match percentage we found for the new search, which contains fainter TGFs than in the catalog, is consistent with the result of *Collier et al.* [2011]. Also *Connaughton et al.* [2010] found a comparable match percentage between WWLLN and FERMI when the search criteria were relaxed.

[18] By choosing $p_{\max} = 10^{-10}$ we find 1283 events. Some of these appear in regions where one does not expect to find TGFs. Also the match percentage with WWLLN starts to

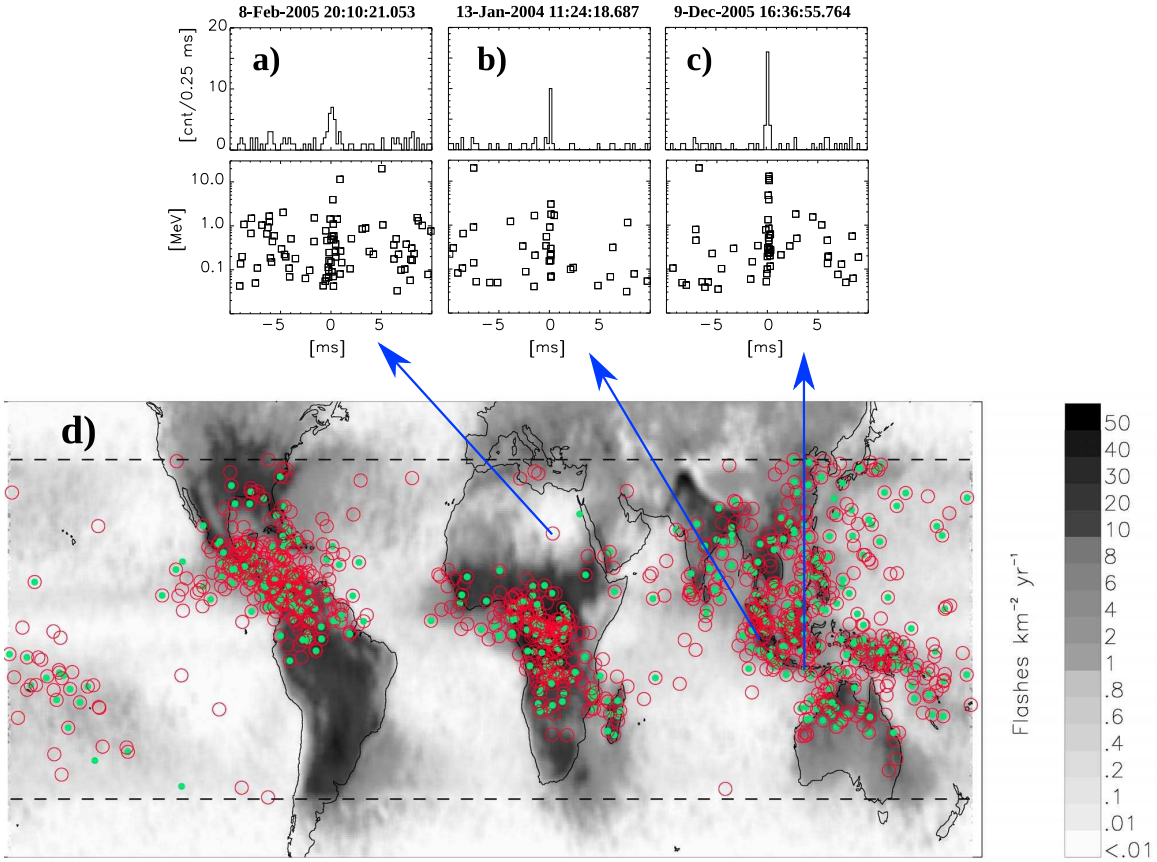

Figure 1. (a–c) (top) The light curve and (bottom) each photon with energy versus time. Figures 1a and 1b are new TGFs. Figure 1c is also presented in the RHESSI catalog. (d) RHESSI TGFs for the years 2004, 2005 and 2006. The red circles are TGFs found with the new search algorithm (1012 TGFs) and green dots are TGFs from the RHESSI TGF catalog (474 TGFs). There are no TGFs in most of South America since RHESSI does not provide data for this region (SAMA). The grey scale indicates lightning activity measured by LIS/OTD. The dashed lines are the limits of the RHESSI 38° inclination orbit.

drop at $p_{max} = 10^{-10}$. Even if many of the events where $p_{max} = 10^{-10}$ are assumed to be real TGFs we choose to use $p_{max} = 10^{-11}$ to keep our search results clean.

[19] An animation showing the lighting activity from the Lightning Imaging Sensor (LIS) gridded time series data [*Christian et al.*, 2003] and the occurrence of TGFs is uploaded in the auxiliary material.[1] Animation S1 shows that the TGFs we have found follow the seasonal variation in lighting activity. For example during the northern hemisphere winter we have found only one TGF over the Caribbean while the vast majority of TGF observations in the Caribbean occur during northern hemisphere summer and fall. A similar variation is also found in the lightning activity [*Christian et al.*, 2003]. This seasonal variation of TGFs is well established. *Splitt et al.* [2010] have shown that RHESSI catalog TGFs follow the diurnal, seasonal, and geographic patterns of lightning activity.

[20] The intensities of the new RHESSI TGFs and the catalog TGFs are shown in Figure 2a, with black and red curves respectively. As expected most of the new TGFs are weaker than the catalog TGFs. Assuming that the TGF fluence distribution follows a power law we would expect to find more TGFs when the lower threshold for detection are reduced [*Collier et al.*, 2011; *Østgaard et al.*, 2012].

[21] Due to radiation damage in the RHESSI instrument, events occurring before 1 January 2005 are the most reliable for energy analysis [*Grefenstette et al.*, 2009]. Figure 2b

Table 1. Number of TGFs/Year From the RHESSI Catalog N_c and From the New Search N_n[a]

	RHESSI Catalog		New Search TGFs	
Year	N_c	Match (%)	N_n	Match (%)
2004	156	7.7	362	7.2
2005	181	6.1	344	7.8
2006	135	7.4	306	12.4

[a]The percentage match between TGFs and WWLLN for the RHESSI catalog, N_c [*Collier et al.*, 2011], and the new search N_n is also shown.

[1]Auxiliary material data sets are available at ftp://ftp.agu.org/apend/gl/2012gl050899. Other auxiliary materials files are in the HTML. doi:10.1029/2012GL050899.

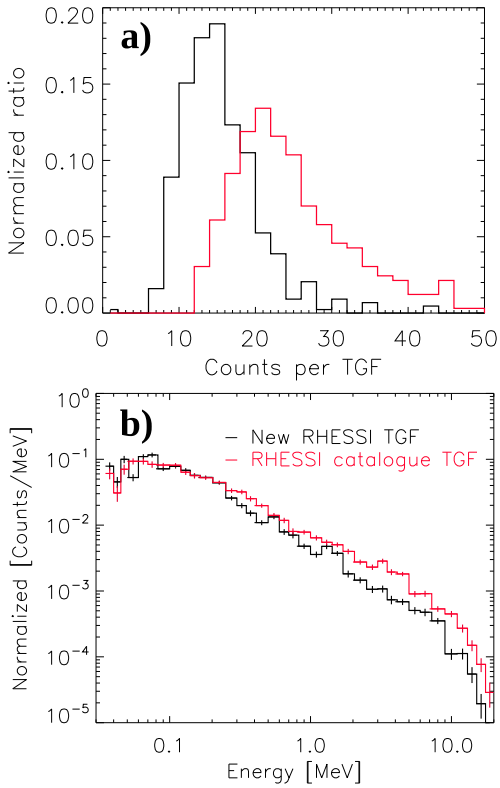

Figure 2. (a) Distribution of TGF intensity for year 2004, 2005 and 2006. Black is from 554 new TGFs and red is from 474 catalog TGFs. (b) The energy spectrum from 156 catalog TGFs in 2004 in red. The black spectrum is 210 TGFs only found in the new search. Notice that the new energy spectrum is softer than the catalog energy spectrum.

shows superposed energy spectra for TGFs occurring during 2004. The red curve is TGFs from the RHESSI catalog. The black curve contains only new TGFs for the same period. The energy spectrum from the new TGFs is softer than the energy spectrum from the catalog. If we assume an upper limit on the TGF intensity we expect that reducing the detection threshold leads to an increase in the satellite's field of view since attenuation and distance effects reduce the TGFs fluence at increasing distances. Simulations by *Østgaard et al.* [2008] have shown that Compton scattering will soften the energy spectrum for TGFs observed at large distances. It is also found that RHESSI TGFs measured at large distances have a softer energy spectrum than TGFs measured closer to the sub-satellite point [*Hazelton et al.*, 2009; *Gjesteland et al.*, 2011].

[22] The main difference between the algorithm presented here and the one presented by *Grefenstette et al.* [2009] are: 1) Relaxing the signal to noise threshold. *Grefenstette et al.* [2009] required at least $12 \cdot \sqrt{N+1} + N$ counts in a 1 ms window where N is the background. This will give a threshold of $p < 10^{-16}$ when $N = 2$ counts per ms which is the average RHESSI count rate . The new algorithm require $p < 10^{-11}$.2) We have used a shorter search window (0.3 ms in addition to 1 ms and 3 ms). 3) We have included a criterion on the hardness ratio similar to the one used in AGILE search [*Marisaldi et al.*, 2010a].

[23] The search presented here is developed to lower the threshold for detection to find new TGFs with $p < 10^{-11}$. The p-value is chosen such that we expect to find one false TGF per year based on statistical fluctuations. However, since the background spectrum is softer than the TGF spectrum, our criteria may reduce this value. We cannot be sure that our search does not include false TGFs. However, since the new TGFs are found in regions known to produce TGFs, and since the match with WWLLN events is improved in the new search we feel confident that the vast majority of the TGFs found in this study are real TGFs.

[24] In the auxiliary material we provide the time to the nearest ms and location for the 1012 TGFs found by our search. It has been suggested that the RHESSI clock is approximately 1.8 ms slower than UTC [*Grefenstette et al.*, 2009] and therefore 1.8 ms should be added to the times we present.

4. Summary

[25] We have developed a new search algorithm which has been applied to the RHESSI data for the years 2004, 2005 and 2006. Our findings are:

1. We have more than doubled the population of detected RHESSI TGFs in this period.
2. The RHESSI TGFs follow the seasonal variation of lightning activity.
3. The match percentage with WWLLN events is comparable for the new TGFs, indicating that WWLLN is just as sensitive to the source lightning for new TGFs as the catalog TGFs.
4. The superposed energy spectrum of the new RHESSI TGFs is softer than the superposed spectrum of the RHESSI catalog, which indicates that RHESSI field of view is increased.

[26] **Acknowledgments.** This study was supported by the Research Council of Norway under contracts 184790/V30 and 197638/V30. We thank the RHESSI team for the use of RHESSI raw data and software. The LIS/OTD High Resolution Annual Climatology (HRAC) data were produced by the LIS/OTD Science Team (Principal Investigator, Hugh J. Christian). We thank the institutions contributing to WWLLN (http://wwlln.net/).

[27] The Editor thanks two anonymous reviewers for their assistance in evaluating this paper.

References

Briggs, M. S., et al. (2011), Electron-positron beams from terrestrial lightning observed with Fermi GBM, *Geophys. Res. Lett.*, *38*, L02808, doi:10.1029/2010GL046259.

Carlson, B. E., N. G. Lehtinen, and U. S. Inan (2009), Observations of terrestrial gamma-ray flash electrons, in *Coupling of Thunderstorms and Lightning Discharges to Near-Earth Space: Proceedings of the Workshop, Corte, France, 23–27 June 2008*, edited by N. B. Crosby et al., *AIP Conf. Proc.*, *1118*, 84–91, doi:10.1063/1.3137717, Am. Inst. of Phys., Melville, N. Y.

Carlson, B. E., T. Gjesteland, and N. Østgaard (2011), Terrestrial gamma-ray flash electron beam geometry, fluence, and detection frequency, *J. Geophys. Res.*, *116*, A11217, doi:10.1029/2011JA016812.

Christian, H. J., et al. (2003), Global frequency and distribution of lightning as observed from space by the Optical Transient Detector, *J. Geophys. Res.*, *108*(D1), 4005, doi:10.1029/2002JD002347.

Collier, A. B., T. Gjesteland, and N. Østgaard (2011), Assessing the power law distribution of TGFs, *J. Geophys. Res.*, *116*, A10320, doi:10.1029/2011JA016612.

Connaughton, V., et al. (2010), Associations between Fermi Gamma-ray Burst Monitor terrestrial gamma ray flashes and sferics from the World

Wide Lightning Location Network, *J. Geophys. Res.*, *115*, A12307, doi:10.1029/2010JA015681.

Dwyer, J. R., and D. M. Smith (2005), A comparison between Monte Carlo simulations of runaway breakdown and terrestrial gamma-ray flash observations, *Geophys. Res. Lett.*, *32*, L22804, doi:10.1029/2005GL023848.

Dwyer, J. R., B. W. Grefenstette, and D. M. Smith (2008), High-energy electron beams launched into space by thunderstorms, *Geophys. Res. Lett.*, *35*, L02815, doi:10.1029/2007GL032430.

Fishman, G. J., et al. (1994), Discovery of intense gamma-ray flashes of atmospheric origin, *Science*, *264*, 1313–1316, doi:10.1126/science.264.5163.1313.

Fishman, G. J., et al. (2011), Temporal properties of the terrestrial gamma-ray flashes from the Gamma-Ray Burst Monitor on the Fermi Observatory, *J. Geophys. Res.*, *116*, A07304, doi:10.1029/2010JA016084.

Gjesteland, T., N. Østgaard, P. H. Connell, J. Stadsnes, and G. J. Fishman (2010), Effects of dead time losses on terrestrial gamma ray flash measurements with the Burst and Transient Source Experiment, *J. Geophys. Res.*, *115*, A00E21, doi:10.1029/2009JA014578.

Gjesteland, T., N. Østgaard, A. B. Collier, B. E. Carlson, M. B. Cohen, and N. G. Lehtinen (2011), Confining the angular distribution of terrestrial gamma ray flash emission, *J. Geophys. Res.*, *116*, A11313, doi:10.1029/2011JA016716.

Grefenstette, B. W., D. M. Smith, B. J. Hazelton, and L. I. Lopez (2009), First RHESSI terrestrial gamma ray flash catalog, *J. Geophys. Res.*, *114*, A02314, doi:10.1029/2008JA013721.

Hazelton, B. J., B. W. Grefenstette, D. M. Smith, J. R. Dwyer, X.-M. Shao, S. A. Cummer, T. Chronis, E. H. Lay, and R. H. Holzworth (2009), Spectral dependence of terrestrial gamma-ray flashes on source distance, *Geophys. Res. Lett.*, *36*, L01108, doi:10.1029/2008GL035906.

Marisaldi, M., et al. (2010a), Gamma-ray localization of terrestrial gamma-ray flashes, *Phys. Rev. Lett.*, *105*(12), 128501, doi:10.1103/PhysRevLett.105.128501.

Marisaldi, M., et al. (2010b), Detection of terrestrial gamma ray flashes up to 40 MeV by the AGILE satellite, *J. Geophys. Res.*, *115*, A00E13, doi:10.1029/2009JA014502.

Østgaard, N., T. Gjesteland, J. Stadsnes, P. H. Connell, and B. Carlson (2008), Production altitude and time delays of the terrestrial gamma flashes: Revisiting the Burst and Transient Source Experiment spectra, *J. Geophys. Res.*, *113*, A02307, doi:10.1029/2007JA012618.

Østgaard, N., T. Gjesteland, B. E. Carlson, R. S. Hansen, and A. B. Collier (2012), The true fluence distribution of terrestrial gamma flashes at satellite altitude, *J. Geophys. Res.*, doi:10.1029/2011JA017365, in press.

Smith, D. M., et al. (2002), The RHESSI spectrometer, *Sol. Phys.*, *210*, 33–60.

Smith, D. M., L. I. Lopez, R. P. Lin, and C. P. Barrington-Leigh (2005), Terrestrial gamma-ray flashes observed up to 20 MeV, *Science*, *307*(5712), 1085–1088, doi:10.1126/science.1107466.

Smith, D. M., B. J. Hazelton, B. W. Grefenstette, J. R. Dwyer, R. H. Holzworth, and E. H. Lay (2010), Terrestrial gamma ray flashes correlated to storm phase and tropopause height, *J. Geophys. Res.*, *115*, A00E49, doi:10.1029/2009JA014853.

Smith, D. M., et al. (2011), A terrestrial gamma ray flash observed from an aircraft, *J. Geophys. Res.*, *116*, D20124, doi:10.1029/2011JD016252.

Splitt, M. E., S. M. Lazarus, D. Barnes, J. R. Dwyer, H. K. Rassoul, D. M. Smith, B. Hazelton, and B. Grefenstette (2010), Thunderstorm characteristics associated with RHESSI identified terrestrial gamma ray flashes, *J. Geophys. Res.*, *115*, A00E38, doi:10.1029/2009JA014622.

Tavani, M., et al. (2011), Terrestrial gamma-ray flashes as powerful particle accelerators, *Phys. Rev. Lett.*, *106*(1), 018501, doi:10.1103/PhysRevLett.106.018501.

B. E. Carlson, T. Gjesteland, and N. Østgaard, Department of Physics and Technology, University of Bergen, Allegaten 55, N-5007 Bergen, Norway. (brant.carlson@ift.uib.no; thomas.gjesteland@uib.no; nikolai.ostgaard@uib.no)

A. B. Collier, SANSA Space Science, PO Box 32, Hermanus 7200, South Africa. (collierab@gmail.com)

C. Eyles, Image Processing Laboratory, University of Valencia, Pol. Ind. La Coma S/N, E-46980 Valencia, Spain. (cje@star.sr.bham.ac.uk)

D. M. Smith, Santa Cruz Institute for Particle Physics, University of California, 1156 High St., Santa Cruz, CA 95064, USA. (dsmith@scipp.ucsc.edu)

6.5 Paper V

The true fluence distribution of terrestrial gamma flashes at satellite altitude
Østgaard, N., T. Gjesteland, B. E. Carlson, R. S. Hansen, and A. B. Collier

J. Geophys. Res., 117, A03327, doi:10.1029/2011JA017365, 2012

JOURNAL OF GEOPHYSICAL RESEARCH, VOL. 117, A03327, doi:10.1029/2011JA017365, 2012

The true fluence distribution of terrestrial gamma flashes at satellite altitude

N. Østgaard,[1] T. Gjesteland,[1] R. S. Hansen,[1] A. B. Collier,[2,3] and B. Carlson[1]

Received 11 November 2011; revised 20 January 2012; accepted 1 February 2012; published 24 March 2012.

[1] In this paper we use the fluence distributions observed by two different instruments, RHESSI and Fermi GBM, corrected for the effects of their different orbits, combined with their different daily TGF detection rates and their relative sensitivities to make an estimate of the true fluence distribution of TGFs as measured at satellite altitudes. The estimate is then used to calculate the dead-time loss for an average TGF measured by RHESSI. An independent estimate of RHESSI dead-time loss and true fluence distribution is obtained from a Monte Carlo (MC) simulation in order to evaluate the consistency of our results. The two methods give RHESSI dead-time losses of 24–26% for average fluence of 33–35 counts. Assuming a sharp cut-off the true TGF fluence distribution is found to follow a power law with $\lambda = 2.3 \pm 0.2$ down to ~5/600 of the detection threshold of RHESSI. This corresponds to a lowest number of electrons produced in a TGF of $\sim 10^{14}$ and a global production rate within $\pm 38^{\circ}$ latitude of 50000 TGFs/day or about 35 TGFs every minute, which is 2% of all IC lightning. If a more realistic distribution with a roll-off below 1/3 (or higher) of the RHESSI lower detection threshold with a true distribution with $\lambda \leq 1.7$ that corresponds to a source distribution with $\lambda \leq 1.3$ is considered, we can not rule out that all discharges produce TGFs. In that case the lowest number of total electrons produced in a TGF is $\sim 10^{12}$.

Citation: Østgaard, N., T. Gjesteland, R. S. Hansen, A. B. Collier, and B. Carlson (2012), The true fluence distribution of terrestrial gamma flashes at satellite altitude, *J. Geophys. Res.*, *117*, A03327, doi:10.1029/2011JA017365.

1. Introduction

[2] With the discovery of terrestrial gamma flashes (TGFs) above thunderstorms [*Fishman et al.*, 1994] by the Burst and Transient Source Experiment (BATSE) a new mechanism of the coupling between the lower atmosphere and space was found. The phenomenon involves both gamma photons, relativistic electrons and positrons. Charged particles are accelerated in extremely strong electric fields (>300 kV/m sea level equivalent) associated with lightning discharges and initiate a relativistic runaway process [*Gurevich et al.*, 1992]. Through interaction with the neutral atmosphere bremsstrahlung is produced, resulting in the escape of electrons [*Dwyer et al.*, 2008], positrons [*Briggs et al.*, 2011] and gamma photons into space. There are still many open questions related to TGFs, and one of them will be addressed in this paper: How common are TGFs? Or more specifically: What is the true fluence distribution of TGFs as measured from satellite altitude?

[3] From the first observations it was believed that the TGFs are produced above 40 km and that they were related to transient luminous events [*Fishman et al.*, 1994; *Nemiroff et al.*, 1997], a reasonable suggestion given the relatively few observations of about 10 TGF/year by BATSE (78 TGFs in 9 years according to http://www.batse.msfc.nasa.gov/batse/misc/triggers.html). However, results from Reuvan Ramaty High Energy Solar Spectroscopic Imager (RHESSI) ten years later indicated that their production altitude is most likely around 15–21 km [*Dwyer and Smith*, 2005]. While BATSE had an on-board trigger algorithm with a 64 ms search window, the data from RHESSI were downloaded and a more sophisticated, but still rather conservative, search algorithm with a search window of 1 ms was applied. For more details about the search algorithm we refer to *Grefenstette et al.* [2009]. Having a trigger window significantly longer than the typical duration of a TGF(<1 ms), like BATSE had, only events with high count rates that exceed the statistical fluctuations of background counts will be classified as TGFs. However, RHESSI had a search window comparable to the duration of a TGF and could identify much weaker TGFs. Thus, RHESSI was able to report more than 100 TGFs/year (975 TGFs in 8.5 years according to http://scipp.ucsc.edu/~dsmith/tgflib_public/). Reanalyses of the BATSE data have also confirmed a production altitude of TGFs below 20 km [*Carlson et al.*, 2007; *Østgaard et al.*, 2008; *Gjesteland et al.*, 2010]. Consistent with this production altitude and general lightning physics, *Williams* [2006] speculated that TGFs are related to positive intracloud lightning, a suggestion that has been supported by a few studies comparing TGFs with

[1]Department of Physics and Technology, University of Bergen, Bergen, Norway.
[2]SANSA Space Science, Hermanus, South Africa.
[3]University of KwaZulu-Natal, Durban, South Africa.

0148-0227/12/2011JA017365

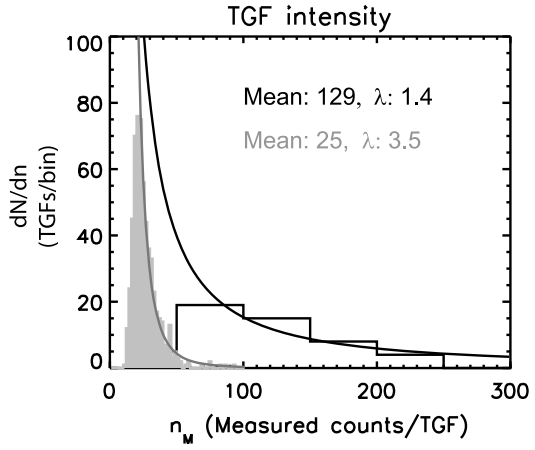

Figure 1. The fluence distributions of TGFs measured by RHESSI (grey histogram) and Fermi (black histogram). Power functions are fitted to both distributions. The average values for Fermi are for TGF pulses, defined as counts in the central 50% of duration.

electromagnetic characteristics of lightning [*Cummer et al.*, 2005; *Shao et al.*, 2010; *Cummer et al.*, 2011]. As intracloud lightning accounts for about 75% of all the lightning [*Boccippio et al.*, 2001] and most of these are positive intracloud lightning bringing negative charges upward, this may imply that TGFs are a rather common phenomenon. X-ray bursts have been observed from negative leader steps in cloud-to-ground (CG–) lightning [*Dwyer et al.*, 2005] and from dart leaders in rocket triggered lightning [*Dwyer et al.*, 2004] before the return strokes of the CG– lightning. Discharge experiments in the laboratory [*Nguyen et al.*, 2008] have also shown that bursts of X-rays are observed slightly before ($\sim$1 μs) the discharge return stroke. All these studies give some hints that TGFs might be more common than observations from space have indicated so far. On the other hand, *Smith et al.* [2011] suggested that the non-detection of TGFs by the Airborne Detector for Energetic Lightning Emissions (ADELE) may indicate the opposite, that there are very few TGFs with intensities two-three orders of magnitude weaker than those observed by RHESSI.

[4] Measurements from space have been hampered by the loss of counts due to dead-time in the electronics, limited instrument sensitivity and limitations due to the on-board trigger window. In this paper we will use the fluence distributions observed by two different instruments, RHESSI and Fermi GBM, corrected for the effects of their different orbits, combined with their different daily TGF detection rates and their relative sensitivities to make an estimate of the true fluence distribution of TGFs at satellite altitudes. This estimate is then used to calculate the dead-time loss for an average TGF fluence measured by RHESSI. Independent estimates of RHESSI dead-time loss and true fluence distribution are obtained from a Monte Carlo (MC) simulation in order to evaluate the consistency of our results. Finally, we discuss our results in the context of ADELE's sensitivity and the non-detection of TGFs by this aircraft.

2. The Measured TGF Fluence Distributions and Average Duration

[5] The fluence distribution of the 591 TGFs measured by RHESSI (March 4, 2002–December 31, 2005) and the first 53 TGFs measured by Fermi (Aug 7, 2008–March 10, 2010) are shown in Figure 1. The RHESSI TGFs were downloaded from http://scipp.ucsc.edu/~dsmith/tgflib_public/ and are the same as used in the quantitatively analysis by *Grefenstette et al.* [2009] obtained before the degradation of the instrument's sensitivity when the effective detector area was still 256 cm^2. The Fermi TGFs are taken from *Fishman et al.* [2011, Table 2]. The three double peaks in that table are treated as separate TGFs giving a total of 53 TGF pulses. All these TGFs were detected when an on-board 16 ms trigger window was used. A power function with the form

$$\frac{dN}{dn} = A_0 n^{-\lambda} \tag{1}$$

(dN is the number of TGFs with fluence within dn and A_0 is a scaling factor) has been fitted to each of the distribution, giving λ of 3.5 and 1.4, for RHESSI and Fermi, respectively. The fit is based on 14 (4) bins from the peak using bin size of 2 (50) counts for the RHESSI (Fermi) distribution. A power function was chosen because the measured RHESSI fluence distribution could be fairly well fitted with such a function. The accuracy of the fit will be discussed in section 5. We interpret the very soft fluence distribution (meaning relatively many low fluence TGFs) from RHESSI to be caused by dead-time losses that are most significant for high photon fluxes. Although Fermi also has dead-time losses, the very hard fluence distribution (meaning relatively many high fluence TGFs) from Fermi can probably be explained by the long trigger window of 16 ms, which favors high fluence TGFs. For these reasons we believe that the true fluence distribution is somewhere in between these two distributions.

[6] The durations of the 591 RHESSI TGFs have a mean of 374 μs and a median of 299 μs. The duration of a TGF is defined as the $\pm 2\sigma$ of a Gaussian function fitted to the light curve of total counts. The majority of the first 53 TGF pulses measured by Fermi have durations between 100 μs and 400 μs [*Fishman et al.*, 2011]. For comparison *Gjesteland et al.* [2010] reported 5 TGFs measured by BATSE to have a production duration of 200–250 μs.

3. Differences in Sensitivity and Total Number of Observed TGFs

[7] For the 591 RHESSI TGFs observed before January 1, 2006 the average time between TGFs was 2.35 day or 0.42 TGFs/day using a lower threshold cut-off of 17 counts [*Grefenstette et al.*, 2009]. For the first 53 TGFs measured by Fermi they observed 0.03 TGFs/day when a 16 ms on-board trigger window was applied to the NaI scintillators, which increased to 0.3 TGFs/day when the same window was applied to the BGO detectors [*Fishman et al.*, 2011]. However, after the Fermi team started downloading most of the data obtained over regions where TGFs are produced, *Fishman* [2011] reported that more than 1 TGF/day has been

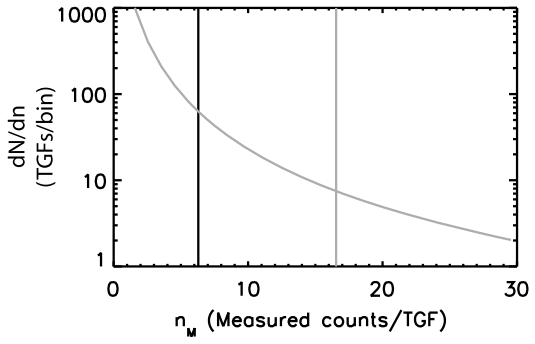

Figure 2. The average lower threshold of RHESSI (grey) and FERMI (black) given on the RHESSI scale of counts/TGF. The distribution of TGFs with an exponent of 2.3 is shown as a grey curve.

observed. According to *Briggs* [2011; M. Briggs, personal communication, 2011] their ground search found 234 TGFs in 591.8 hours of data over regions which are expected to have a high TGF rate. Over the same hours and from the same regions, they found 23 triggered TGFs, a 10.2 times increase in detection rate. According to *Fishman et al.* [2011] 35 TGFs were observed after the trigger algorithm change (from NaI to BGO) in at least 141 days of data. Of the 35 triggered TGFs 21 were inside the regions where all the data have been downloaded [*Briggs*, 2011] and the scaling factor of 10.2 should apply. We do not know if this ratio is also valid for the areas outside the boxes which are mostly over ocean. Although there are fewer thunderstorms over ocean the ratio of IC/CG and the fluence distribution of TGFs might be the same. As we are not aware of any studies that give any information whether the TGF distribution over ocean is softer or harder than over land, we will apply an uncertainty of ±50% for the triggered-to-search ratio for the regions outside the boxes. This uncertainty also accounts for any seasonal biases in the downloaded data. This gives us a daily detection rate of 2.5 ± 0.5 TGFs/day (35/141 × 10.2 and 21/141 × 10.2 + 14/141 × (15.3 or 5.1)).

[8] From the RHESSI data we know that TGFs have a strong latitudinal dependence with fewer TGFs produced at higher latitudes. As Fermi, due to its inclination of 25.6° spends more time over regions with more TGFs than RHESSI (38° inclination), Fermi should see more TGFs than RHESSI. As we want to derive a relative daily detection rate that only depends on sensitivity differences we need to correct for this effect. This correction is performed as follows: First, we consider the RHESSI TGF fluence distribution (N_R) versus latitude (θ), $dN_R/d\theta$, corrected for the latitudinal cosine effect on area. Then we calculate the fraction of the orbit RHESSI (O_R) spends at various latitudes, $dO_R/d\theta$, when the orbit is given as a sine function with amplitude of 38° + 3° latitude. A similar calculation is performed for Fermi, $dO_F/d\theta$, but with an amplitude of 25.6° +3° latitude. The extra 3° is to account for a field of view of about 400 km. The expected Fermi TGF distribution is then given as

$$\frac{dN_F}{d\theta} = \frac{dN_R}{d\theta} \times \frac{dO_F/d\theta}{dO_R/d\theta} \quad (2)$$

By integrating $dN_R/d\theta$ and $dN_F/d\theta$ over latitudes we estimate that Fermi, just due to orbital differences between the two spacecraft, is expected to see 65% more TGFs than RHESSI. This means that the relative detection rate between Fermi and RHESSI due to sensitivity differences only, Y, is given by (2.5 ± 0.5)/1.65/0.42 = 3.6 ± 0.7. It should be noted that this is what Fermi would have seen if they downloaded data similar to RHESSI and is what we will use as the relative detection rate between the two instruments. However, the real detection rate for Fermi is 1.6 TGFs/day (21 × 10.2/141 + 14/141).

[9] Even if the photon flux of a TGF has a rapid rise, the decay, due to Compton scattering, is usually slow [*Østgaard et al.*, 2008] and there is no reason to believe that RHESSI, due to dead-time losses, should miss TGFs with high fluence. Dead-time losses would only lead to underestimating the fluence of strong TGFs. When Fermi sees more TGFs than RHESSI it implies that its sensitivity is better. Although Fermi BGO detectors have a slightly larger effective detector area than RHESSI, that is 320 cm^2 [*Meegan et al.*, 2009; *Briggs et al.*, 2010] compared to 256 cm^2 [*Grefenstette et al.*, 2009] flying at practically the same altitude, the most important reason for the higher sensitivity is that a more efficient trigger algorithm for the on-ground analysis has been developed for Fermi. According to *Briggs* [2011] the on-ground trigger algorithm requires ≥4 counts in each of the two BGO detector, ≥4 in all the 12 NaI detectors and with a probability less than 10^{-11} giving a lower threshold of 19 counts in all detectors. For the comparison with the 591 RHESSI TGFs for which a lower cut-off threshold of 17 counts (before background subtraction) have been used we use the ≥8 counts (also before background subtraction) in the two BGO detectors with an energy averaged effective detector area of 160 cm^2 × 2 = 320 cm^2 to obtain the relative sensitivity, X, between Fermi and RHESSI as

$$X = \frac{17}{8} \times \frac{320}{256} = 2.7 \quad (3)$$

This is equivalent to Fermi having a lower threshold of 6.3 on the RHESSI scale as visualized in Figure 2. Although there are uncertainties related to this estimate we will show that it provides results that converge with the rest of the information we have and are consistent with an independent MC simulation of RHESSI dead-time. Uncertainties related to the relative sensitivity will be discussed.

4. The True Fluence Distribution and RHESSI Dead-Time Losses

[10] In the search algorithm to find the 591 RHESSI TGFs with the daily detection rate of 0.42 TGFs/day a lower threshold cut-off of 17 counts was used. However, our MC simulations of dead-time loss indicates that RHESSI only has a one-to-one response up to 10 counts (see Figure 4a). However, between 10 and 20 counts the errors of the estimated true counts are still overlapping the one-to-one response. We will therefore use a fluence of 15 counts as the threshold where the RHESSI results start to be affected by dead-time losses, but also show the effect of using 10 and 20 counts.

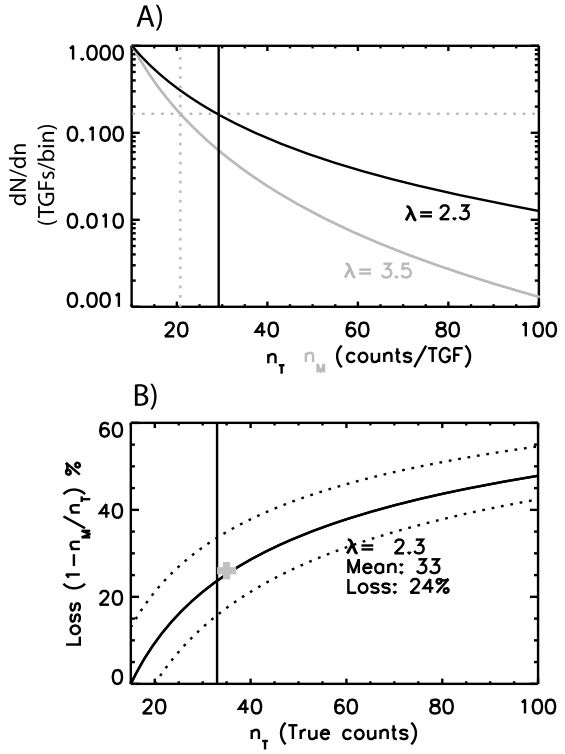

Figure 3. (a) The distribution measured by RHESSI (thick grey) and the estimated true TGF distribution at RHESSI altitude based on the two instrument's different photon detection sensitivities and their relative daily TGF detection rate. (b) The loss due to dead-time in the RHESSI electronics as a function of true counts (incoming photon fluence). Solid line is for 15 counts used as the threshold where RHESSI experiences dead-time losses. Dotted lines are for lower threshold of 10 counts (upper) and 20 counts (lower). The grey cross is the average dead-time loss determined by the MC simulations described in section 5.

[11] Given that both RHESSI and Fermi are measuring from a true fluence distribution that follows a power law with an unknown exponent, λ, but with different lower detection thresholds, we have the following expression for the total number of TGFs detected by Fermi:

$$N_F = \int_{n_{0F}}^{\infty} A_0 n^{-\lambda} dn = \frac{A_0}{\lambda - 1} n_{0F}^{1-\lambda} \tag{4}$$

where n is fluence and n_{0F} is the lower threshold of detection. The total number of TGFs detected by RHESSI, N_R can be expressed similarly, but with a different lower threshold, n_{0R}. We can then express the relative total number of detected TGFs which is equivalent to the relative daily detection rate, Y, as a function of the two lower thresholds

$$Y = \frac{N_F}{N_R} = \left(\frac{n_{0F}}{n_{0R}}\right)^{1-\lambda} = \left(\frac{1}{X}\right)^{1-\lambda} \tag{5}$$

With relative sensitivity, $X = 2.7$, and relative daily detection rate, $Y = 3.6 \pm 0.7$, this can be solved to get an exponent

$$\lambda = 2.3 \pm 0.2 \tag{6}$$

Knowing the distribution of TGFs measured by RHESSI, with $\lambda = 3.5$ and the estimated true TGF distributions, with $\lambda = 2.3$ we can calculate RHESSI dead-time losses as a function of incoming photons. For a specific number of TGFs within a fluence interval, dN/dn, in Figure 3a the dead-time loss is the difference between the true fluence, n_T, and the measured fluence n_M divided by n_T. This is shown in Figure 3b where we have used a fluence of 15 (solid line), with 10 and 20 as uncertainties (dotted lines),

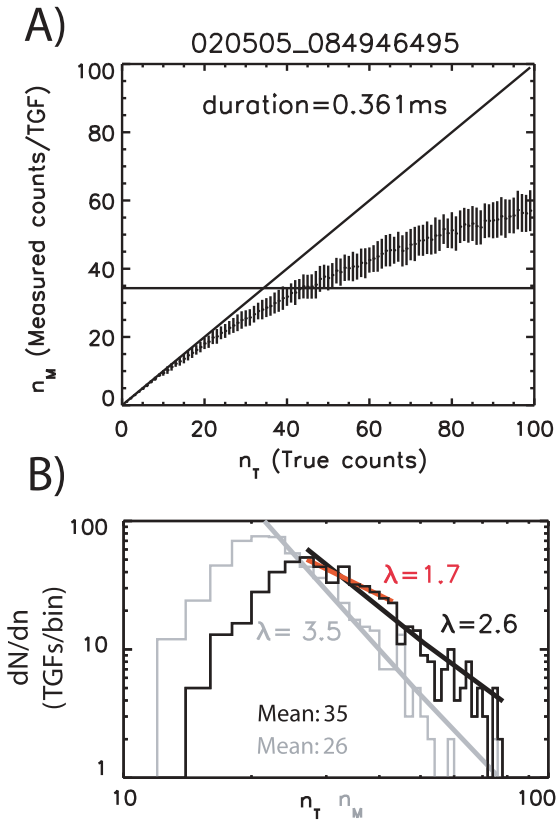

Figure 4. (a) Monte Carlo simulation of the TGF observed May 2, 2005, with a duration of 361 μs, with increasing true fluence from 0 to 100. Vertical line denotes the measured counts and the true counts can be read out from the intersection between MC values and horizontal line, here 45 $\pm$7. The diagonal line indicates that RHESSI has no dead-time losses up to about 15 counts. (b) Grey histogram is the measured fluence distribution of the 591 RHESSI TGFS, while black histogram is the true fluence distribution running the MC model on each of the 591 TGFs. Due to background subtraction there are TGFs with less than 17 counts. The black, grey and red lines show the fitted power distributions for the measured ($\lambda = 3.5$) true ($\lambda = 2.6$) and the lower bins of the true ($\lambda = 1.7$).

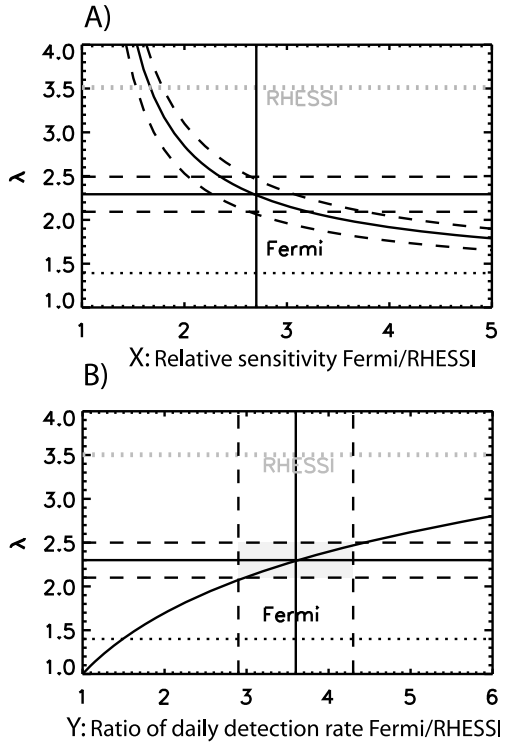

Figure 5. How the exponent, λ, depends on (a) the relative sensitivity of the two instruments and (b) the relative daily detection rate. In Figure 5a the vertical line is the relative sensitivity we have based our calculation on. The dashed lines show the same dependence when the upper and lower limits of Y are used. In Figure 5b the solid vertical line is the relative daily detection rate with lower and upper limits as dashed lines with the corresponding upper and lower limits for λ (horizontal dashed lines). In both panels the dotted lines are the λ for the measured distributions by RHESSI (grey) and Fermi (black).

as the level where dead-time losses start to affect the RHESSI counts. The loss for an average TGF (33 counts) is 24% which is fairly close to what was obtained from the MC simulations (grey cross), 26% for an average of 35 counts (Figure 4b).

5. Monte Carlo Simulation of RHESSI Dead-Time Losses

[12] To obtain an independent estimate of RHESSI dead-time losses a MC simulation was performed. For this MC simulation we used the characteristic times of the RHESSI electronics [*Grefenstette et al.*, 2009] to determine the dead-time in each of the 8 detectors. Then, for each TGF the following two steps are performed: 1) The duration of the TGF is calculated as within 2 standard deviations of a Gaussian fit to the TGF light-curve. 2) By increasing the number of photons distributed randomly within the duration of each TGF a detection efficiency curve is obtained. As this was performed hundred times for each number of photons we obtain the statistical error due to the random distribution of photons within the duration, which is shown as vertical lines in Figure 4a. The black horizontal line at 34 counts is what RHESSI measured for this specific TGF and the true counts can be read out from the intersection between the MC values and the horizontal line, here 45 $\pm$7. This curve would have been identical to the one shown in Figure 3b if both the measured counts and duration were equal to the averages, 34 counts and 374 μs. When this MC scheme is applied to all the 591 RHESSI TGFs a true fluence distribution of TGFs can be obtained, as shown by the black histogram in Figure 4b. Using the average fluence of the true distribution and the measured distribution we get the dead-time losses for an average RHESSI TGF of 26%, as shown as a grey cross in Figure 3b. Power functions can be fitted to the distributions. Depending on how many bins from the peak value that are used for the fit we find that the measured distribution before dead time correction (grey histogram) can be fitted with power exponents ranging from 3.2 (11 bins) to 3.7 (17 bins). A χ^2-test (reduced) of these fits is equally good ($\chi^2_R \leq 0.15$). Similarly, for the dead time corrected distribution (black histogram) we find power exponents ranging from 2.3 (10 bins) to 3.0 (19 bins), which are equally good with $\chi^2_R \leq 0.2$. In Figure 4b we have chosen to show exponents in the middle of the intervals, λ of 3.5 for the non-corrected distribution, that was used for estimating the RHESSI dead time losses in section 4. For the corrected distribution we show a λ of 2.6 for the entire distribution and a λ of 1.7 for the lower part, indicating a roll-off, as will be discussed in section 6.

6. Discussion

[13] Fermi also has a dead-time loss up to 50% for intense TGFs [*Briggs et al.*, 2010]. Because Fermi is seeing 3.6 $\pm$ 0.7 times more TGFs than RHESSI, we believe that Fermi due to its more sophisticated search algorithm, is seeing the weaker part of the TGF fluence distribution. We can not rule out that Fermi may lose some counts due to dead-time even for these weak TGFs, but we will argue that the lower threshold of TGF detection for Fermi is most likely determined by the signal-to-noise ratio rather than dead-time losses.

[14] There are two important values that our estimated true fluence distribution depends on: 1) the relative sensitivity (X) of the two instruments and 2) the relative daily detection rate (Y), where we have used $X = 2.7$ and $Y = 3.6 \pm 0.7$. To examine how uncertainties in these two estimates may influence our result we can rewrite equation (5) to obtain

$$\lambda = 1 + \frac{\ln(Y)}{\ln(X)} \tag{7}$$

[15] In Figure 5a we keep the relative daily TGF detection rate fixed at $Y = 3.6$ and let the relative sensitivity (X) vary from 1 to 5. One can see that if Fermi is more sensitive relative to RHESSI than we have estimated (moving to higher values) the true distribution will be slightly harder. On the other hand, if the two instruments have almost similar sensitivities the true fluence distribution quickly becomes very soft. The dashed lines show the same dependence when the upper and lower limits of Y are used. We have based our estimate of relative sensitivity on information presented by

Grefenstette et al. [2009], *Meegan et al.* [2009], *Briggs et al.* [2010], and *Briggs* [2011, also personal communication, 2011]. For the RHESSI data we have only used the 591 TGFs before the degradation of the instrument occurred. The average effective detection area is adopted from *Briggs et al.* [2010], but looking at Figure 11 of *Meegan et al.* [2009] one could argue that the average is closer to 170 cm^2. This would have given us a λ of 2.2, but introduces an uncertainty too small to affect the ± 0.2 used in equation (6).

[16] In Figure 5b we keep the relative sensitivity fixed at $X = 2.7$ and let the daily TGF detection rate (Y) vary from 1 to 6. The daily TGF detection rate for RHESSI is fairly well established by *Grefenstette et al.* [2009], while Fermi's daily detection rate is given as approximately 1 [*Fishman*, 2011]. As described above, based on the information given by *Briggs* [2011, also personal communication, 2011] we found that the equivalent (to RHESSI) daily detection rate for Fermi after downloading data, due to sensitivity differences only, is 1.5 ± 0.3 TGFs/day, with 1.2 (1.8) TGFs/day corresponding to TGFs with higher (lower) fluence over ocean than land. The grey shaded box in Figure 5b shows the range spanned by the two extreme values and indicates that the true fluence distribution of TGFs as measured from satellite altitude follows a power law with $\lambda = 2.3 \pm 0.2$. This is in good agreement with the estimated power distributions with λ ranging from 1.9 to 2.5 reported by *Gjesteland et al.* [2011], using geolocation and energy spectra of RHESSI TGFs.

[17] The two methods we have used give converging λ-values. Furthermore, if 10 to 12 bins were used for the fit to dead-time corrected distribution in Figure 4b we would get $\lambda = 2.3$. As we in our first approach focus on extending the distribution down to fluences below the RHESSI lower threshold, we conclude that both methods support a distribution with $\lambda = 2.3 \pm 0.2$.

[18] What we have estimated is the true TGF distribution as measured from satellite altitude, which is not necessarily the same as the true TGF source distribution. Flying much closer to the source, an experiment like ADELE is probably exposed to a distribution more similar to the latter. In a recent paper *Carlson et al.* [2012] have calculated the relationship between the two and for hard distributions the differences are significant. For a distribution with $\lambda = 2.3 \pm 0.2$ the true source distribution would have $\lambda = 2.0 \pm 0.2$. As reported by *Smith et al.* [2011] ADELE, flying at 14 km altitude, saw only one TGF when passing 1213 lightning discharges less than 10 km away. However, ADELE was closer than 4 km to 133 discharges and according to the model results presented in that paper the sensitivity of ADELE is increased about two-to-three orders of magnitude from 10 km to 4 km.

[19] It has been suggested that TGFs are associated with IC lightning bringing negative charges upward [*Cummer et al.*, 2005; *Williams*, 2006; *Shao et al.*, 2010; *Cummer et al.*, 2011]. As this type of lightning accounts for about 75% of all lightning [*Boccippio et al.*, 2001] this would imply that almost all lightning discharges have an associated TGF. We will now discuss this hypothesis in the context of the power distributions we have found and the non-detection of TGFs by ADELE as well as the sensitivity of ADELE versus RHESSI.

[20] First, we estimate the relative sensitivity between ADELE at 10 km and RHESSI. We use 400 km as the radius of the effective detection area below RHESSI [see *Collier et al.*, 2011, Figure 6] and notice that RHESSI detects TGFs produced within $\pm 38°$ latitude. Then, the global production rate of TGFs within this latitude range and with strength larger than the RHESSI threshold of 17 counts is about 260 TGFs/day. The global lightning rate is 3.8×10^6/day [*Christian et al.*, 2003], but within $\pm 38°$ latitude it is 3.5×10^6/day. If we only consider the IC lightning (75% of total) we get a RHESSI-TGF/lightning ratio of 9.8×10^{-5}. Of 1213 lightning RHESSI would have seen 0.1 TGF, while ADELE saw 1. Solving equations (5) or (7) with $Y = 10$ and $\lambda = 2.3$ gives $X = 6$ indicating that ADELE's sensitivity at 10 km is about 6 times better than RHESSI and 2 times better than Fermi. If the source distribution with $\lambda = 2.0$ were used these number would be larger.

[21] In Figure 6a we show the integrated distribution of TGFs, N, as a function of lower detection threshold, n_0, (equation (4)) from 1213 and 133 lightning discharges assuming that they all make TGFs with a fluence distribution following a power law with $\lambda = 2.0$ (solid lines). The two values of n_0 denote the lower threshold (relative scale) for detecting 1 TGF ($N = 1$). For $\lambda = 2.0$ the sensitivity has to increase by a factor of $\sim$10 (1/0.1) to see 1 TGF from a distribution of 133 given that 1 TGF was detected from a distribution of 1213. ADELE's sensitivity is modeled to be 100–1000 times better at 4 km compared to 10 km [*Smith et al.*, 2011] and corresponds to having a lower threshold of $n_0 = 1/100$ to 1/1000 (Figure 6a). This would imply that ADELE should have seen about 10 (at $n_0 = 1/100$) TGFs from the 133 lightning discharges if they all produce TGFs, and the probability of non-detection is very low.

[22] It should be noticed that the modeling of ADELE's sensitivity is based on certain assumptions. The model is only valid for IC+ discharges, while at least 50% of the subset shown in Figure 2 (top and middle) of *Smith et al.* [2011] are CG– discharges. A fixed 87 g/cm^2 is used for the avalanche region, which might be reasonable for charge top below 16 km (3 km charge separation), but is very large (5 km) for the higher charge tops.

[23] Assuming that ADELE's sensitivity is indeed 1000 times better at 4 km compared to 10 km our results indicate that there is a cut-off (or roll-off) in the TGF distribution. Such a cut-off is implicit in the analysis of a fixed number of lightning discharges: the lower limit must be chosen such that the integral of the distribution matches the number of events. ADELE's single observation at a relative intensity of $n_0 = 1$ out of 1213 lightning discharges implies a minimum intensity threshold of $n_0 \sim 1/1000$, the minimum value on the x axis in Figure 6a. We can estimate at which fluence value relative to the lower threshold of RHESSI detection this cut-off might be, assuming that the TGFs follow Poisson statistics. The probability, p, of non-detection when predicted number of detection is N_P, is given by

$$p|_0^N = e^{-N_P} \tag{8}$$

[24] In Figure 6b we show the probability of non-detection given that one TGF was observed at 10 km as a function of the relative sensitivity of ADELE between 10 km and 4 km,

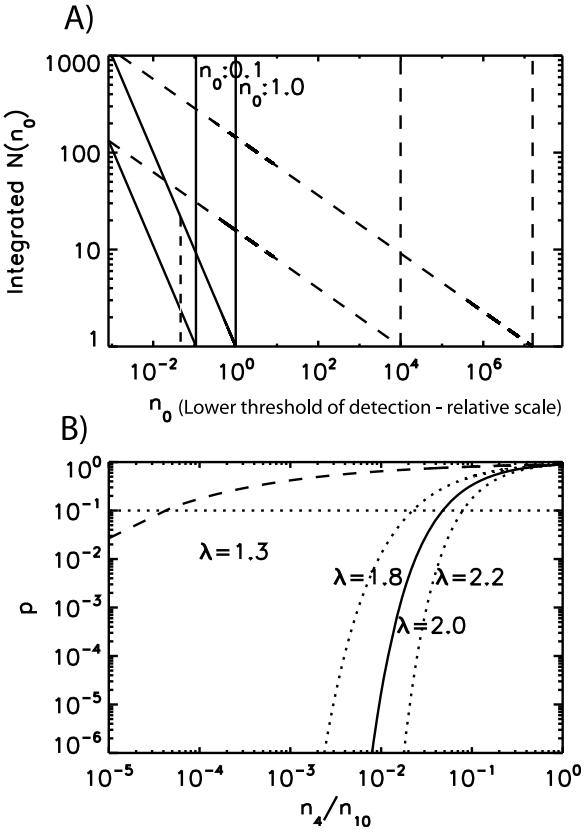

Figure 6. (a) The distribution of TGFs if all the 1213 and 133 lightning discharges can produce TGFs with a power law distribution with $\lambda = 2.0$ (solid). The values, n_0, indicate the relative lower threshold for detecting one TGF for $\lambda = 2.0$ (solid). The vertical dotted line is the highest number of observed TGFs given a sharp cut-off in the distribution. The dashed lines are for a power distribution with $\lambda = 1.3$. (b) The probability of non-detection as a function of relative sensitivity for ADELE at 10 km and 4 km given that one TGF was detected at 10 km. Probabilities are shown for distributions with $\lambda = 2.0$ (solid) and $\lambda = 1.8$ and 2.2 (dotted) and $\lambda = 1.3$ (dashed). The horizontal dotted line indicates a probability of 1 out of 10.

given by the relative lower thresholds of detection, n_4/n_{10}. Given that 0.1 ($N_P = 2.6$) from the 133 distribution is a reasonable probability of non-detection (marked with a dotted horizontal line in Figure 6b) this cut-off is at a sensitivity level of 5/100 of ADELE at 10 km, which is 5/600 of the weakest TGF observed by RHESSI (RHESSI has 1/6 of ADELE sensitivity at 10 km), or ~3/600 if one compares with the average RHESSI TGF, which is a factor of 2 larger than the RHESSI lower threshold. If the increase of ADELE's sensitivity is less than three orders of magnitude (from 10 km to 4 km) this cut-off would move to lower values. If all the lightning discharges produces TGFs, the modeling results of *Smith et al.* [2011] would have to be off by a little less than one order of magnitude.

[25] We can relate this cut-off in the TGF distribution to the lowest number of electrons that can be produced in a TGF and what the global TGF production rate would be. Our modeling results, using the model described by *Østgaard et al.* [2008], indicate that the total number of photons produced in an average RHESSI TGF ranges from 10^{16} (21 km production altitude) to 10^{18} (15 km production altitude) in agreement with others [e.g., *Smith et al.*, 2011]. The probability of bremsstrahlung production increases non-linearly with energies and is about 10% for 2 MeV electrons [*Berger and Seltzer*, 1972] and approaches 100% at higher electron energies. Measured photon energies >20 MeV indicate that we are in this energy range, which implies that the number of electrons is also ranging from 10^{16} to 10^{18}. With a cut-off in the TGF distribution at 5/600 of the RHESSI threshold the lowest possible number of electrons produced in a TGF would be $\sim 10^{14}$.

[26] From Figure 6a one can see that a cut-off at $n_0 = 5/100$ which corresponds to ~5/100 of ADELE at 10 km and 5/600 of the RHESSI lower threshold would give 20 TGFs from the 1213 lightnings from which RHESSI would have seen 0.1 TGF. This implies that the global production rate of TGFs within ±38° latitude is about 200 (20/0.1) times what we estimated from RHESSI TGF detection. This gives 50000 TGFs/day or about 35 TGFs every minute and compared to the IC lightning occurrence frequency within the same latitude range of 2.7×10^6/day, the ratio of TGF/lightning is about 2%. These numbers are slightly larger than estimated by *Smith et al.* [2011].

[27] We should emphasize that these estimates are based on only one single TGF observation from 10 km. Furthermore, they are based on the assumption of having a sharp cut-off in the TGF distribution. In reality there is probably a roll-off which would decrease the lowest number of electrons and increase the global TGF production rate. Our estimates are consistent with the non-detection by ADELE and depend strongly on these results. If future aircraft or balloon missions find slightly different results our estimates need to be recalculated.

[28] Finally, we will discuss the implication of a roll-off instead of a sharp cut-off in the TGF distribution which is a more realistic distribution. Our results indicate that the power law with $\lambda = 2.3$ is valid at least down to the Fermi threshold, which is 1/3 of RHESSI. Looking at the black histogram in Figure 4b one can argue that there is indeed a roll-off in the lower 8 bins from the peak value, which can be fitted with a λ of 1.7. According to *Carlson et al.* [2012], this corresponds to a source distribution with $\lambda < 1.3$. As long as the roll-off threshold is at 1/3 of RHESSI lower threshold or higher, ADELE is observing from the part of the distribution with $\lambda = 1.3$. Such a distribution is shown as dashed lines in Figure 6a, and one can see that the ADELE's sensitivity would have to increase 3 orders of magnitude (n_0 decreases from 10^7 to 10^4 on the relative scale) to see 1 TGF from a distribution of 133 TGFs. As can be seen from Figure 6b the probability of non-detecting at 4 km ($n_4/n_{10} = 1/10000$) is only 0.1. In this case we can not rule out that all IC lightning discharges produce TGFs. Using the true distribution as seen from space ($\lambda = 1.3$) an ideal instrument with sensitivity ~10000 times better than RHESSI would have seen about N = 4000 TGFs/day within

a radius of 400 km. The lowest number of total electrons produced in a TGF would then be $\sim 10^{12}$.

7. Summary

[29] To summarize, we have used two independent methods to find the RHESSI dead-time losses and an estimate of the true fluence distribution of TGFs as measured from satellite altitude. The two methods give dead-time losses of 24% and 26% for an average RHESSI TGF 33–35 counts. Assuming a sharp cut-off the true TGF fluence distribution is found to follow a power law with $\lambda = 2.3 \pm 0.2$ down to $\sim$5/600 of the detection threshold of RHESSI. This corresponds to a lowest number of electron produced in a TGF to be $\sim 10^{14}$ and a global production rate within $\pm 38^{\circ}$ latitude of 50000 TGFs/day or about 35 TGFs every minute, which is 2% of all IC lightning. If a more realistic distribution with a roll-off below 1/3 (or higher) of the RHESSI lower detection threshold with a true distribution with $\lambda \leq 1.7$ that corresponds to a source distribution with $\lambda \leq 1.3$ is considered, we can not rule out that all discharges produce TGFs. In that case the lowest number of total electrons produced in a TGF is $\sim 10^{12}$.

[30] **Acknowledgments.** We are indebted to the RHESSI and Fermi GBM teams for the design and successful operations of the two missions. We thank D. A. Smith for the use of RHESSI data and M. Briggs for the use of Fermi GBM data. This study was supported by the Norwegian Research Council, under the two contracts 197638/V30 and 208028/F50.

[31] Robert Lysak thanks the reviewers for their assistance in evaluating this paper.

References

Berger, M. J., and S. M. Seltzer (1972), Bremsstrahlung in the atmosphere, *J. Atmos. Terr. Phys.*, *34*, 85–108.

Boccippio, D. J., K. L. Cummings, H. J. Christian, and S. J. Goodman (2001), Combined satellite- and surface-based estimation of the intracloud-cloud-to-ground lightning ratio over the continental United States, *Mon. Weather Rev.*, *129*(1), 108–122, doi:10.1175/1520–0493(2001)129.

Briggs, M. S. (2011), More TGFs from GBM, paper presented at Terrestrial Gamma-Ray Flash Workshop 2011, Cent. for Space Plasma and Aeron. Res., Univ. of Ala., Huntsville.

Briggs, M. S., et al. (2010), First results on terrestrial gamma ray flashes from the Fermi Gamma-ray Burst Monitor, *J. Geophys. Res.*, *115*, A07323, doi:10.1029/2009JA015242.

Briggs, M. S., et al. (2011), Electron-positron beams from terrestrial lightning observed with Fermi GBM, *Geophys. Res. Lett.*, *38*, L02808, doi:10.1029/2010GL046259.

Carlson, B. E., N. G. Lehtinen, and U. S. Inan (2007), Constraints on terrestrial gamma ray flash production from satellite observation, *Geophys. Res. Lett.*, *34*, L08809, doi:10.1029/2006GL029229.

Carlson, B. E., T. Gjesteland, and N. Østgaard (2012), Connecting the terrestrial gamma-ray flash source strength and observed fluence distributions, *J. Geophys. Res.*, *117*, A01314, doi:10.1029/2011JA017122.

Christian, H. J., et al. (2003), Global frequency and distribution of lightning as observed from space by the Optical Transient Detector, *J. Geophys. Res.*, *108*(D1), 4005, doi:10.1029/2002JD002347.

Collier, A. B., T. Gjesteland, and N. Østgaard (2011), Assessing the power law distribution of TGFs, *J. Geophys. Res.*, *116*, A10320, doi:10.1029/2011JA016612.

Cummer, S. A., Y. Zhai, W. Hu, D. M. Smith, L. I. Lopez, and M. A. Stanley (2005), Measurements and implications of the relationship between lightning and terrestrial gamma ray flashes, *Geophys. Res. Lett.*, *32*, L08811, doi:10.1029/2005GL022778.

Cummer, S. A., G. Lu, M. S. Briggs, V. Connaughton, S. Xiong, G. J. Fishman, and J. R. Dwyer (2011), The lightning-TGF relationship on microsecond timescales, *Geophys. Res. Lett.*, *38*, L14810, doi:10.1029/2011GL048099.

Dwyer, J. R., and D. M. Smith (2005), A comparison between Monte Carlo simulations of runaway breakdown and terrestrial gamma-ray flash observations, *Geophys. Res. Lett.*, *32*, L22804, doi:10.1029/2005GL023848.

Dwyer, J. R., et al. (2004), A ground level gamma-ray burst observed in association with rocket-triggered lightning, *Geophys. Res. Lett.*, *31*, L05119, doi:10.1029/2003GL018771.

Dwyer, J. R., et al. (2005), X-ray bursts associated with leader steps in cloud-to-ground lightning, *Geophys. Res. Lett.*, *32*, L01803, doi:10.1029/2004GL021782.

Dwyer, J. R., B. W. Grefenstette, and D. M. Smith (2008), High-energy electron beams launched into space by thunderstorms, *Geophys. Res. Lett.*, *35*, L02815, doi:10.1029/2007GL032430.

Fishman, G. J. (2011), Positrons observed to originate from thunderstorms, *Eos Trans. AGU*, *92*(22), 185, doi:10.1029/2011EO220001.

Fishman, G. J., et al. (1994), Discovery of intense gamma-ray flashes of atmospheric origin, *Science*, *164*, 1313–1316.

Fishman, G. J., et al. (2011), Temporal properties of the terrestrial gamma-ray flashes from the Gamma-Ray Burst Monitor on the Fermi Observatory, *J. Geophys. Res.*, *116*, A07304, doi:10.1029/2010JA016084.

Gjesteland, T., N. Østgaard, J. Stadsnes, P. H. Connell, and G. J. Fishman (2010), Effects of deadtime losses on terrestrial gamma ray flash measurements done by the Burst And Transient Source Experiment, *J. Geophys. Res.*, *115*, A05303, doi:10.1029/2009JA014754.

Gjesteland, T., N. Østgaard, A. B. Collier, B. E. Carlson, M. B. Cohen, and N. G. Lehtinen (2011), Confining the angular distribution of terrestrial gamma ray flash emission, *J. Geophys. Res.*, *116*, A11313, doi:10.1029/2011JA016716.

Grefenstette, B. W., D. M. Smith, B. J. Hazelton, and L. I. Lopez (2009), First RHESSI terestrial gamma ray flash catalog, *J. Geophys. Res.*, *114*, A02314, doi:10.1029/2008JA013721.

Gurevich, A. V., G. M. Milikh, and R. Roussel-Dupré (1992), Runaway electron mechanism of air breakdown and preconditioning during a thunderstorm, *Phys. Lett. A*, *165*(5), 463–468.

Meegan, C. A., et al. (2009), The Fermi Gamma-ray Burst Monitor, *Astrophys. J.*, *702*, 791–804, doi:10.1088/0004–637X/702/1/791.

Nemiroff, R. J., J. T. Bonnell, and J. P. Norris (1997), Temporal and spectral characteristics of terrestrial gamma flashes, *J. Geophys. Res.*, *102* (A5), 9659–9665.

Nguyen, C. V., A. P. J. van Deursen, and U. Ebert (2008), Multiple X-ray bursts from long discharges in air, *J. Phys. D Appl. Phys*, *41*, 234012, doi:10.1088/0022–3727/41/23/234012.

Østgaard, N., T. Gjesteland, J. Stadsnes, P. H. Connell, and B. Carlson (2008), Production altitude and time delays of the terrestrial gamma flashes: Revisiting the Burst and Transient Source Experiment spectra, *J. Geophys. Res.*, *113*, A02307, doi:10.1029/2007JA012618.

Shao, X. M., T. Hamlin, and D. M. Smith (2010), A closer examination of terrestrial gamma-ray flash-related lightning processes, *J. Geophys. Res.*, *115*, A00E30, doi:10.1029/2009JA014835.

Smith, D. M., et al. (2011), The rarity of terrestrial gamma-ray flashes, *Geophys. Res. Lett.*, *38*, L08807, doi:10.1029/2011GL046875.

Williams, E. R. (2006), Problems in lightning physics—the role of polarity asymmetry, *Plasma Sources Sci. Technol.*, *15*(2), 91–108, doi:10.1088/0963-0252/15/2/S12.

B. Carlson, T. Gjesteland, R. S. Hansen, and N. Østgaard, Department of Physics and Technology, University of Bergen, Allegt. 55, N-5007 Bergen, Norway. (nikolai.ostgaard@ift.uib.no)

A. B. Collier, SANSA Space Science, Hospital Street, Hermanus, 7200 South Africa.